Stable Perovskite Quantum Dots Synthesis for Light-emitting Diodes

A thesis submitted to The University of Nottingham for the degree of

Doctor of Philosophy

Xuanyu Zhang

20319318

Supervised by

Dr Chengbo Wang

Dr Yong Ren

Dr Chaoyu Xiang

June 2024

Preface

This thesis is Xuanyu Zhang's original work supervised by Dr. Chenbo Wang, Dr Yong Ren, and Dr Chaoyu Xiang.

Published works related to this thesis are listed below:

- X. Zhang, Q. Wang, Z. Yao, M. Deng, J. Wang, L. Qian, Y. Ren, Y. Yan, C. Xiang, Stable Perovskite Quantum Dots Light-Emitting Diodes with Efficiency Exceeding 24%, Adv. Sci. (2023). https://doi.org/10.1002/advs.202304696.
- Y. Li, M. Deng, X. Zhang, L. Qian, C. Xiang, Proton-Prompted Ligand Exchange to Achieve High-Efficiency $CsPbI_3$ Quantum Dot Light-Emitting Diodes, Nano-Micro Lett. 16 (2024) 1–10. https://doi.org/10.1007/s40820-024-01321-8.
- Y. Li, M. Deng, X. Zhang, T. Xu, X. Wang, Z. Yao, Q. Wang, L. Qian, C. Xiang, Stable and efficient $CsPbI_3$ quantum-dot light-emitting diodes with strong quantum confinement., Nat. Commun. 15 (2024) 5696. https://doi.org/10.1038/s41467-024-50022-8.
- Q. Wang, X. Zhang, L. Qian, C. Xiang, Improving Perovskite Green Quantum Dot Light-Emitting Diode Performance by Hole Interface Buffer Layers, ACS Appl. Mater. Interfaces 15 (2023) 28833–28839. https://doi.org/10.1021/acsami.3c04592.
- P. Shen, X. Zhang, R. Wu, T. Zhang, L. Qian, W. Xu, K. Kang, D. Zhao, C. Xiang, Interfacial Regulation toward Efficient $CsPbBr_3$ Quantum Dot-Based Inverted Perovskite Light-Emitting Diodes, ACS Appl. Mater. Interfaces (2023). https://doi.org/10.1021/acsami.3c18816.

The author's other published works during the Ph.D. program are listed in Appendix 2.

Abstract

The perovskite quantum dots (PeQDs) are one of the potential candidate materials for next-generation display technologies due to their unique optoelectrical properties. PeQDs have strengths such as high photoluminescence, good defect tolerance, tunable wavelength, narrow emission, and solution processability. However, PeQDs easily lose ligands because of their ionic nature, inducing photoluminescence quenching and merging to bulk. In addition, the uncontrollable hot injection (HT) method intensifies the situation, resulting in broad size distribution and low crystallinity. Consequently, the light-emitting diodes based on PeQDs exhibit a short operation lifetime. The instability impedes the commercial application of PeQDs. This thesis proposes strategies to improve the performance of materials and devices.

Firstly, caesium and halide vacancies are passivated by resurfacing agents. In addition, Ostwald ripening is suppressed. Potent ligands react with hydrobromide acid to form resurfacing agents. The ligand exchange reactions are acid-driven, while extra bromide anions hinder the Ostwald ripening. As a result, weak ligands, such as oleic acid/oleylamine, are substituted by strong ligands via in-situ ligand exchange in the growth process.

Secondly, short chain-length ligands control the nucleation by adjusting the acid/base equilibrium of the solution. The intermediate $PbBr_2$

clusters are superfluous nucleation sources. Homogenous nucleation is achieved by using octanoic acid/octylame, eliminating clusters. Moreover, short chain-length ligands improve the conductivity of materials. The synthesised $CsPbBr_3$ NCs show near-unit photoluminescence efficiency and narrow size distribution. The fabricated device achieves a peak EQE of 24.13% and an operation lifetime T_{50} of 54 minutes at 10000 $cd \cdot m^{-2}$.

Thirdly, the same strategies are used to gain stable $CsPbI_3$ QDs successfully. However, it is hard to obtain small-size $CsPbI_3$ QDs due to synthesis difficulties. Different resurface agents are used here. The 2-naphthalene sulfonic acid is introduced as a resurfacing agent to suppress Ostwald ripening, as it is an aromatic ligand and binds strongly to QDs. Moreover, ammonium hexafluorophosphate exchanges long-chain ligands and avoids regrowth during purification. Both ligands ameliorate the charge transport ability of $CsPbI_3$ quantum dots. The pure red $CsPbI_3$ quantum dots achieve 94% photoluminescence quantum efficiency. Devices based on those QDs gain a peak EQE of 26.04%.

The thesis focuses on improving device performance with high-quality PeQDs. Different perovskite quantum dots employ stable transport layers with high carrier mobility and suitable energy levels. The proposed two synthesis strategies ameliorate the crystallinity, size distribution, photoluminescence quantum yield, and conductivity of PeQDs. With the corresponding device structure, high-performance light-emitting diodes

are fabricated. The synthesis strategies give new insight into PeQD synthesis.

Acknowledgement

Time flies by four years, and it feels like it was just yesterday when I began my doctoral research. Although it is not difficult to complete the research work, unexpected challenges and difficulties always arise. This journey has given me invaluable experience and wealth for my future. It gives me the confidence to face challenges and solve problems for the rest of my life. I express profound appreciation to all the supervisors and colleagues who have supported and helped me throughout my doctoral program.

First, I would express my gratitude to my first supervisor, Professor Chengbo Wang. He gives me timely help and guidance when I struggle to continue my PhD program. With his help, I can continue my PhD research. Second, I am deeply grateful to Professor Yong Ren. He is patient with students and positively responds to my questions. He offers me lots of inspiration and guidance about my research. Third, I am indebted to Professor Chaoyu Xiang. He is my supervisor at Ningbo Institute of Materials Technology and Engineering, CAS. I continuously explore the frontiers of perovskite quantum dots with his help. Finally, I would like to express my respect and commemorate Professor Lei Qian, the former head of the research group who has made significant contributions to the community.

In addition, I would thank my cherished friend, enthusiastic colleagues and respectful collaborations, especially Dr Zhaobing Tang, Tengzuo Huang, Ben He, Zuyan Chen, Dr Bin Song, Dr Shuo Ding, Dr Chunyan Wu, Dr Zhiwei Yao, Dr Piaoyang Shen, Dr Ximeng Wang, and Qiangqiang Wang, Bo Zhang, Yanming Li, Ming Deng, Ruifa Wu, Jianan Chen, Wenqiang Li. Thanks for your support and for accompanying me on such an enriched journey.

Last but also vital, I owe an immense debt of thanks to my beloved parents and other cherished friends. You are the people who unwaveringly support me as I continue to walk forward.

Nomenclature

Symbol	Designation	Unit
T_x	Operation lifetime is the value when it decreases to x% of its initial value.	Time unit, second, minute or hour, etc.
J	Current density	$mA \cdot cm^{-2}$
V	Voltage	V
L	Luminance	$cd \cdot m^{-2}$
$\boldsymbol{E_g^*}$	Bandgap of quantum dots	eV
$\boldsymbol{V_{TFL}}$	Trap-filled limit voltage	V
$\boldsymbol{\mu}$	Carrier mobility	$cm^2 \cdot (V\ s)^{-1}$
$\boldsymbol{e}$	Elementary charge	C
$\boldsymbol{N_t}$	Trap states	cm^{-3}
n	Refractive index	Dimensionless quantity

Abbreviations

Light emitting diode (LED).

Liquid crystal display (LCD).

Organic light emitting diode (OLED).

Quantum dot light emitting diode (QLED).

Active-matrix quantum dot light emitting diode (AM-QLED).

Perovskite quantum dot emitting diode (PeQLED).

Lead halide perovskite (LHP).

Nanocrystal (NC)

Perovskite light emitting diodes (PeLEDs).

External quantum efficiency (EQE).

Power conversion efficiency (PCE).

Electroluminescence (EL).

Current density–voltage–luminance (*J-V-L*).

Full width at half maximum (FWHM).

International Commission on Illumination / Commission Internationale de l´Eclairage (CIE)

Methylammonium (MA^+).

Formamidinium (FA^+).

Photoluminescence quantum yield (PLQY).

Phenethylammonium (PEA^+).

Electron transporting layer (ETL).

Hole transport layer (HTL).

Hole injection layer (HIL)

List of Table

List of Figure

Contents

Chapter 1. Introduction and Research Objectives

1.1 Background

Dr. Brus and his coworkers first proposed the concept of colloidal quantum dots (QDs) in 1983(Brus, 1984). Generally speaking, colloidal QDs are nanoparticles smaller than their exciton Bohr radius. According to the number of dimensions that electrons are confined with, quantum confinement materials are classified into QDs, nanowires, and nanoplates (Figure 1.1). Colloidal QDs are 3-dimensional confined, manifesting discrete atomic-like density of states (DOS). As a result, colloidal QDs exhibit excellent optoelectronic properties for light-emitting diodes, such as high photoluminescence quantum yield (PLQY), narrow emission spectra, and consecutively tunable bandgap by adjusting the particle size(Chen et al., 2013).

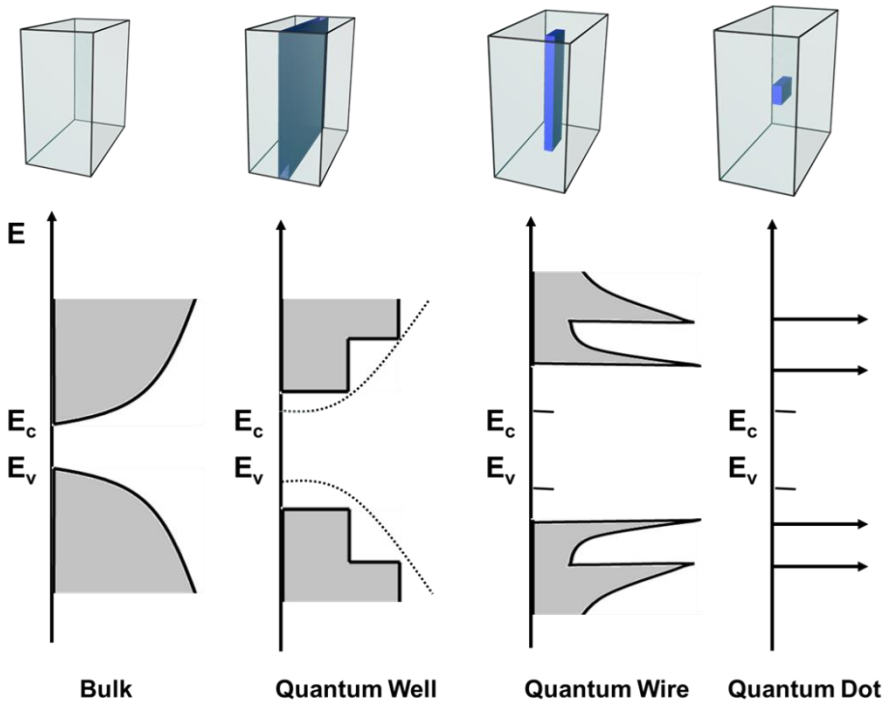

Figure 1.1 | Schematic illustration of the evolution of material bandgap density of states with different dimension confinement.

Traditional Cd-based colloidal QDs also possess good environmental stability due to their inorganic nature(Shirasaki et al., 2013). In addition, the synthesis of colloidal QDs is straightforward and scalable, named the hot-injection method developed in 1993 by Dr. Murry(Nanocrystallites et al., 1993a). The synthesised colloidal QDs are monodispersed with high crystal quality. Moreover, in 2003, the synthesis of the core-shell structure of traditional colloidal QDs (VI-II, V-III) was developed by Dr Peng, which significantly improved the PLQY and stability of materials(Li et al., 2003). The low-cost solution synthesis makes QDs possible for commercial applications. In 2012, Samsung and 3M launched the QD-enhanced liquid crystal display (LCD), which uses photoluminescence QDs as colour converters (Figure 1.2). Various application configurations have been developed over the last decade, such as QDs-enhanced LCD, QD-OLED, and QD-LED. Photoluminescence applications of QDs have achieved tremendous success. Electroluminescence (EL) of QDs has high external quantum efficiency (EQE, defined as the ratio of emitted photons divided by injected hole-electron pairs; see methodology for details) and simple device structures for ultra-thin and flexible displays, which is promising for next-generation displays. However, active-matrix quantum dots light-emitting diodes (AM-QLEDs) have been under development. Moreover, the material requirements for EL applications differ from those of PL applications, emphasising the electrical properties of QDs.

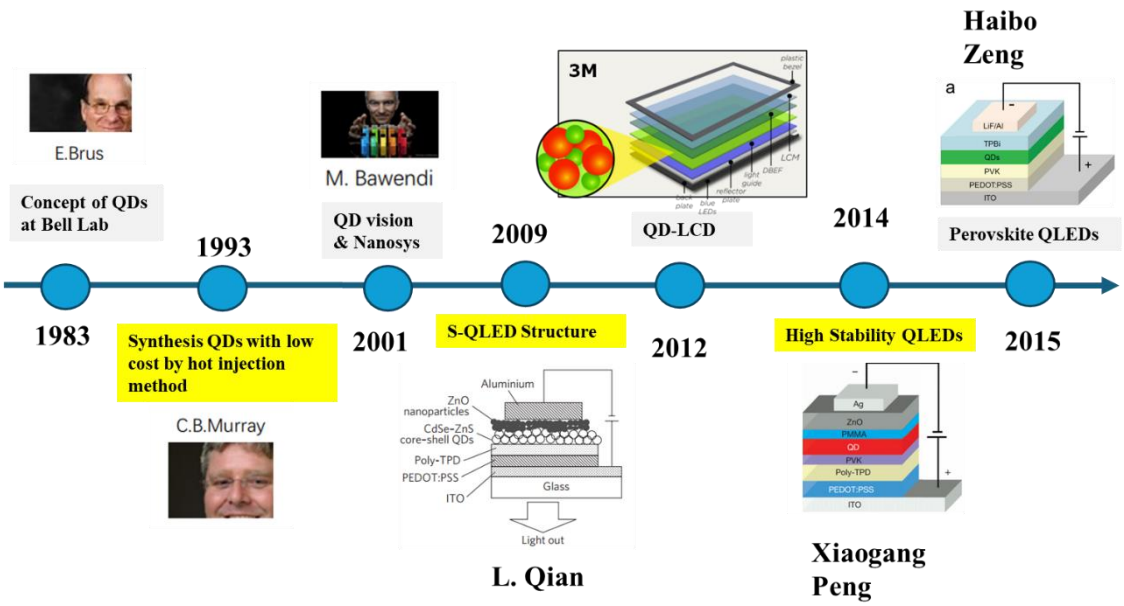

Figure 1.2 | History and development of QDs and devices(Dai et al., 2014; Qian et al., 2010; Song et al., 2015; Yang et al., 2015).

The first reported QLED was in 1994 with low EQE (0.01%)(v. L. Colvin et al., 1994). The device performance of QLEDs was dramatically enhanced through inorganic material—ZnO, an electron transport layer. The device structure was named S-QLED structure, meaning all solution processes are processable (Qian et al., 2011). In 2014, S-QLEDs achieved over 20% EQE with operation stability of T_{50} (the time when the luminance drops to 50% of initial value) 100000 h at 100 cd·m^{-2} and met the industrial standard for display technologies(Dai et al., 2014). The perovskite quantum dots light-emitting diodes (PeQLEDs) are research hotspots and merit academic attention. PeQLEDs based on hot injection (HT) methods were first reported by Dr. Zeng in 2015(Song et al., 2015). The PeQELDs have been developed rapidly in the past several years. The EQE of blue, green, and red PeQLEDs exceeded 18% for green, red, and blue devices within 10 years (Figure 1.3a) (Chiba et al., 2018, 2017; Dong et al., 2020; Fang et al., 2021; Hassan et al., 2021; Jiang et al., 2022; Kim et al., 2021; Kumar et al., 2022; Lan et al., 2021; Li et al., 2017; G. Pan et al., 2020; Song et al., 2018a, 2018b, 2015; Wan et al., 2023; Wang et al., 2020a; Ya‐Kun Wang et al., 2021; M. Xie et al., 2022; J. Zhang et al., 2023; Zheng et al., 2020). Full-colour displays usually employ three primary colours: red, blue, and green. To satisfy the Rec.2020 display industry standard, the wavelength of red, blue, and green emissions should be 620~635 nm, 460~470 nm, and 520~530 nm, respectively(Jang et al., 2021; Yuan et al., 2020; Zheng et al., 2020). However, the bulk emission of $CsPbCl_3$, $CsPbBr_3$, and $CsPbI_3$ perovskite is 390 nm, 520 nm, and 716 nm, respectively(Protesescu et al., 2015; Swarnkar et al., 2016).

For the red $CsPbI_3$ PeQLEDs, the EQE was slightly drop down due to synthesising small-size pure red $CsPbI_3$ (640 nm emission with EQE 23%(Ya‐Kun Wang et al., 2021), 636 nm emission with EQE 20.8%(M. Xie et al., 2022)). State-of-the-art perovskite QLEDs are listed in Supplementary Information Table A1-1. However, the operation stability of PeQLEDs is far from that of Cd-based QLEDs. The world record lifetime of green perovskite QLED is only T_{50} of 12 h at 1000 cd·m^{-2}(Fang et al., 2021), while Cd-based QLEDs have achieved lifetime T_{95} (the time when the luminance drops to 95% of

initial value) of 40000 h at 1000 cd·m^{-2} for red QLEDs in 2023 as manifested in Figure 1.3b(Gao et al., 2023).

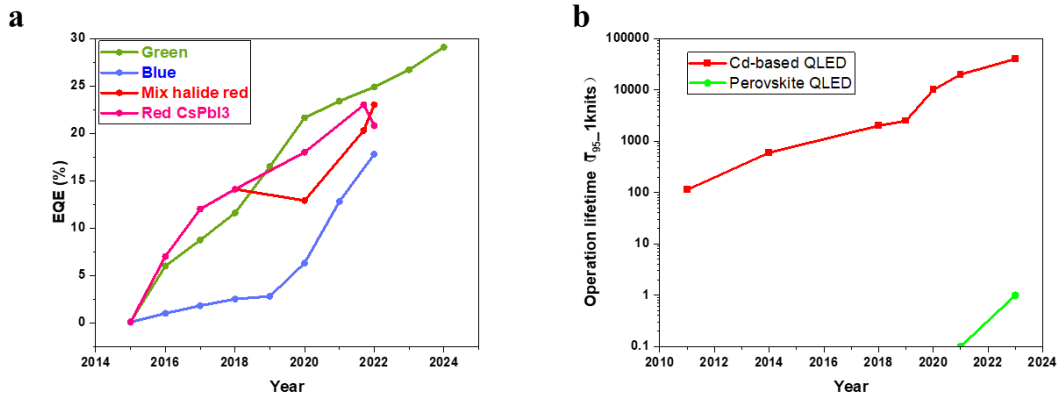

Figure 1.3 | (a) Development of perovskite QLEDs. (b) Comparison of operation lifetime of perovskite QLED versus Cd-based QLEDs.

1.2 Optoelectronic Properties of LHP NCs

Metal halide Perovskite (MHP) was first reported by H.L.WELLS in 1983(Wells, 1893). MHP was used as active layer materials for LED(Era et al., 1994) and channel layers for field effect transistors (FET)(Kagan et al., 1999) in the 1990s. Lead halide perovskite (LHP) was employed as a photosensitiser for solar cell devices and achieved a PCE of 3.8% in 2009(Kojima et al., 2009). LHP quickly caught researchers' attention and became a research hotspot. Perovskites are semiconductor materials with a crystal structure ABX_3. The A site is inorganic or organic cations like Cs^+, MA^+, or FA^+, while the B site is metal cations like Pb^{2+} and Sn^{2+}. For X sites, they are halide anions that are usually chloride, bromine, and iodide. The following Equation can evaluate the stability of the perovskite crystal structure:

$$t = r_A + r_X/\sqrt{2(r_B + r_X)} \quad (1.1)$$

The calculated tolerance factor is t, and r_i is the radii of A, B, and C ions. The tolerance factor t should be in the range from 0.8 to 1.1, which provides theoretical stability of the perovskite crystal structure. Otherwise, the formed perovskite is unstable and quickly decomposes. Moreover, another parameter is used to access the octahedra unit stability of the perovskite as the octahedra factor. Octahedra factor μ is defined as r_B/r_X, which ranges from 0.442 to 0.895(Shamsi et al., 2019). In summary, the structural stability of the perovskite crystal is usually predicted by these two parameters.

It is well known that LHP has achieved massive success in photovoltaic applications.

The PCE of state-of-the-art lead-based perovskite solar cells is up to 25.2% in 2021, with good stability(Yoo et al., 2021). LHP has excellent photoelectrical properties and is a promising semiconductor material for light-emitting applications(Protesescu et al., 2015). The typical synthesis method of LHP QDs was proposed in 2015, which demonstrated that all-inorganic perovskite QDs possess excellent optoelectronic properties for display technology, such as high PLQY, narrow emission, simple synthesis in relatively low temperatures (Cai et al., 2019; Huang et al., 2015; Imran et al., 2018a; Liu et al., 2017; Protesescu et al., 2015). Meanwhile, PeQLEDs were also reported.(Protesescu et al., 2015; Song et al., 2015) As LHP NCs are compatible with the low-cost solution process to fabricate thin films, they are promising to be applied to light-emitting diodes(Li et al., 2016; Ren et al., 2022).

Figure 1.4a is a schematical illustration of the cubic $CsPbBr_3$ perovskite crystal structure. Figure 1.4b is a transmission electron microscope (TEM) image of $CsPbBr_3$ perovskite QDs. There are different crystal structures of perovskite. Some crystal structures exhibit good optoelectronic properties, such as three-dimensional cubic and orthogonal phases. Some phases should be avoided as they do not manifest active photoelectrical properties, such as one-dimensional hexagonal and orthogonal phases.

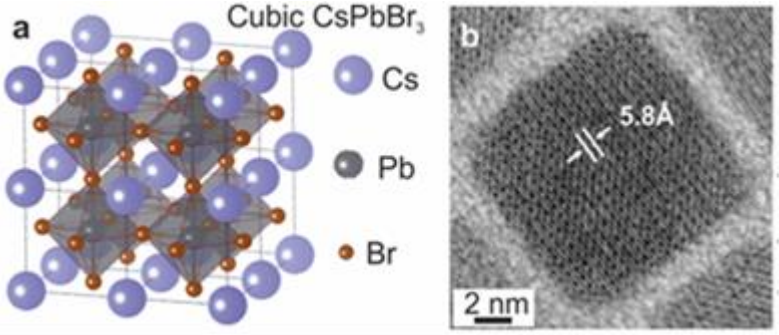

Figure 1.4 | (a) Crystal structure of lead halide perovskite quantum dots. (b) TEM image of $CsPbBr_3$ perovskite QDs(Protesescu et al., 2015).

Tunable Wavelength. The emission wavelength of QDs can be tuned by size effect. Brus derived a model to quantitatively evaluate the correlation between particle size and the quantum confinement effect(Brus, 1986, 1984). The equation used to determine the bandgap or band-edge energy gap of QDs is:

$$E_g^* = E_g + \frac{\hbar^2\pi^2}{2R^2}\left[\frac{1}{m_e^*} + \frac{1}{m_h^*}\right] - \frac{1.786e^2}{\varepsilon R} - 0.248E_R^* \qquad (1.2)$$

Where E_g^* is the bandgap of the QD, E_g is the bandgap of the corresponding bulk material,

$\hbar$ is the reduced Planck's Constant, R is the radius of the QD, m_e&m_h are an effective mass of electrons and holes in the material respectively, ε is the dielectric constant of the bulk material, and E_R^* is the Rydberg energy (which is equal to $e^4/(2\varepsilon^2\hbar^2(m_e^{-1} + m_h^{-1}))$). According to the equation, the bandgap of QD increases with the reduction of QD size. For traditional II-VI or III-V QDs, the emission wavelength is mainly tuned by size effect. Besides the size effect, the bandgap of QD can also be tuned by composition. Perovskite can easily adjust the QD bandgap by mixing the halide Cl, Br, and I with different molar ratios.(Protesescu et al., 2015) LHP QDs have a broad emission range from 405 nm to 700 nm, exhibiting high colour purity and a wide gamut (Figure 1.5). LHP QDs can satisfy the requirements of Rec.2020 and be applied to display technologies.

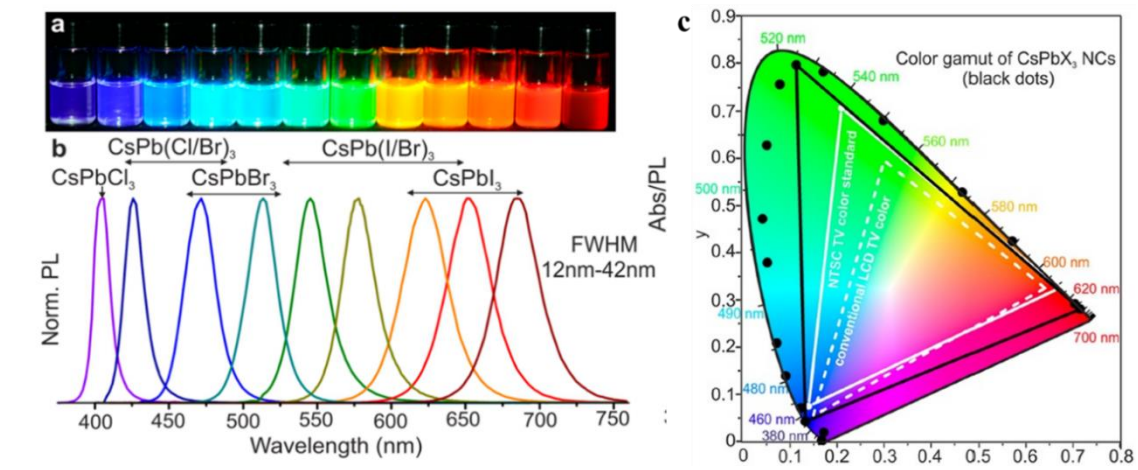

Figure 1.5 | (a) $CsPbX_3$ QDs solution in the visible light range (b) emission spectra of $CsPbX_3$ QDs (c) colour gamut of $CsPbX_3$ QDs(Protesescu et al., 2015).

There are usually two strategies to achieve wavelength tunability. LHP NCs can modify emission wavelength through size effect or composition. For green emission, it is easy for $CsPbBr_3$ NCs to achieve an emission wavelength of 520 nm by doping formamidine (FA) cations(Fang et al., 2021). For red and blue emission, mixing halide ions makes it easy to achieve deep blue ($CsPbCl_xBr_{1-x}$)(Yan et al., 2021) and pure red ($CsPbBr_xI_{1-x}$)(J. Zhang et al., 2023). Nevertheless, mixing halide LHP NCs suffer from phase segregation and unstable emission wavelengths (Vashishtha and Halpert, 2017; Zhang et al., 2019). Phase segregation is induced by ion migration under voltage bias or light excitation, leading to electroluminescence (EL) shift and LHP NC degradation.

Figure 1.6 exhibits the instability of synthesised pure red mixed halide LHP NCs by the classic hot injection method. Synthesizing small-size $CsPbBr_3$ NCs and $CsPbI_3$ NCs can emit deep blue and pure red light, respectively. This strategy can avoid the problem of phase segregation. In addition, the enhancement of quantum confinement of small-size LHP NCs increases exciton binding energy, which improves the PLQY. Therefore, controlling the LHP NC particle size is more charming in achieving stable EL for deep blue and pure red emissions.

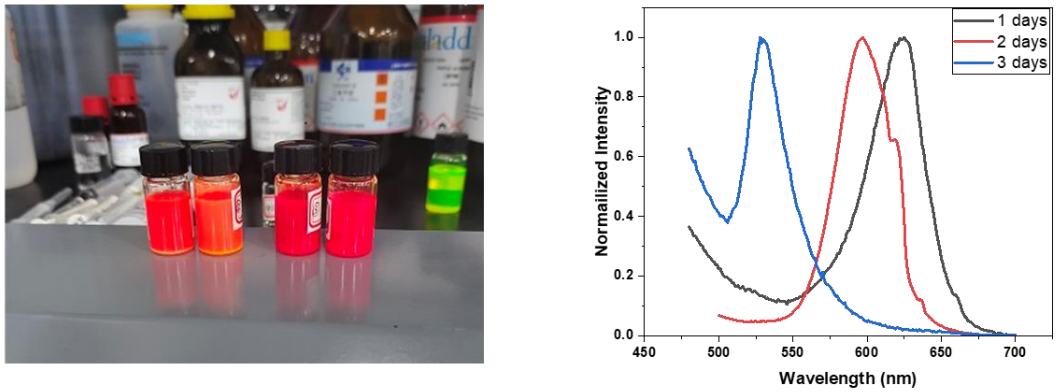

Figure 1.6 | Picture and PL spectra of synthesised pure red $CsPbBr_xI_{1-x}$ NCs stored in the air.

High PLQY. The exciton binding energy of semiconductor materials increases when quantum confinement effects are enhanced, which improves luminescence efficiency. However, traditional Cd-based QD cores have relatively low PLQY (~10%) due to plenty of surface defects(Nanocrystallites et al., 1993b). To improve the PLQY, traditional Cd-based QDs are synthesised with a complicated shell growth process and have a core-shell structure. LHP QDs can achieve near-unit PLQY without a complicated core-shell structure. The shell-free structure of PeQDs means simple synthesis procedures compared to VI-II QDs(Song et al., 2018b). This characteristic of PeQDs is attributed to good defect tolerance, which ensures stable emission of spectra and high PLQY(H. Huang et al., 2017). There are several reasons for high defect tolerance. First, defects of LHP are usually A

site and X site vacancies, which possess low formation energy. Second, the bandgap of LHP is formed between two antibonding orbits(Akkerman et al., 2018). As a result, most defect states are in valance bands or conduction bands. Even formed shallow defect states, those defects do not significantly reduce PLQY. The bandgap of traditional Cd-based QDs is formed between bonding orbits and antibonding orbits, which means that defects are in the bandgap, resulting in non-radiative recombination.

Narrow Emission Spectra. QDs possess a narrower emission width than bulk due to quantum confinement. Compared to OLED or LCD, QDs manifest narrower emission spectra, as shown in Figure 1.7. For example, the full width of half the maximum (FWHM) of $CsPbBr_3$ QDs is around 20 nm. However, the FWHM of $CsPbI_3$ QDs emission is usually about 40 nm. Several factors influence the FWHM of QDs, such as nanocrystal (NC) size distribution, defects, and quantum confinement effects.

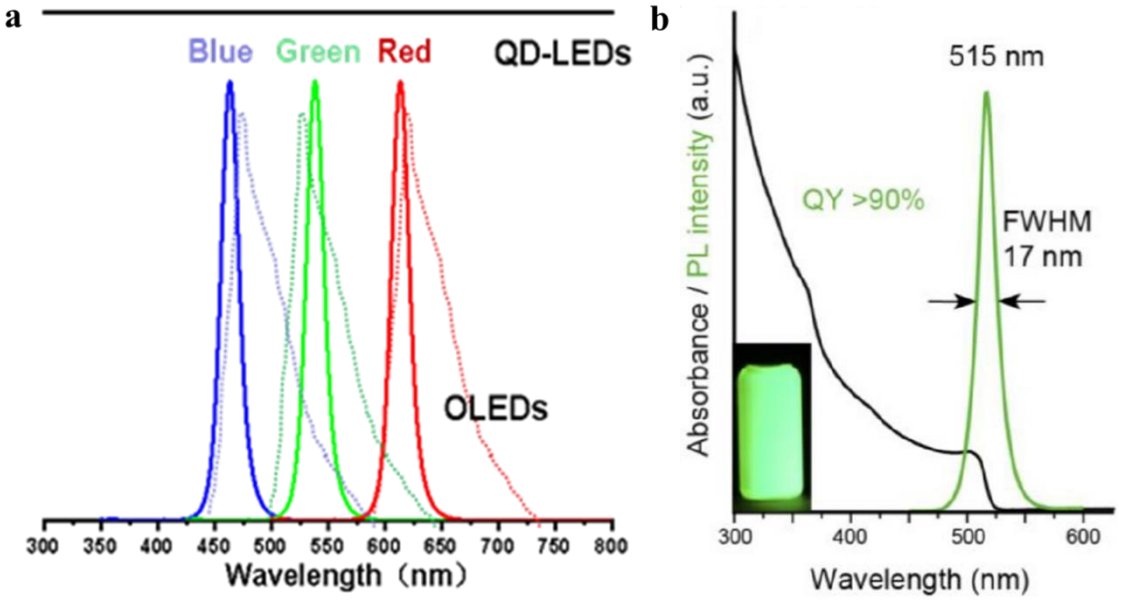

Figure 1.7 | (a) comparison of emission spectra between OLED and QLED (b) emission spectra of $CsPbBr_3$ QDs(Krieg et al., 2018).

Simple and Scalable Synthesis. Fabrication of commercial OLED relies on expensive vacuum deposition equipment, materials, and complicated manufacturing processes. In addition, the vacuum deposition process wastes plenty of materials (about 90%). Solution-processable approaches, such as blade and slot die coating, are low-cost film formation methods(Luo et al., 2014). Colloidal NCs are compatible with solution

processes. Thus, the fabrication cost of QD devices is cheaper. The PeQD synthesis is more straightforward than traditional QDs as there is no shell growth process. Two methods are widely used for PeQD synthesis: one is derived from conventional QDs, the hot injection method, and the other is the room temperature precipitation method. As the synthesis temperature of traditional Cd-based QDs is about 300 ℃, even when employing the hot injection method, the synthesis temperature of PeQDs is lower and in the range from 60 ℃ to 180 ℃(Lignos et al., 2016). In summary, PeQDs have advantages for LED applications.

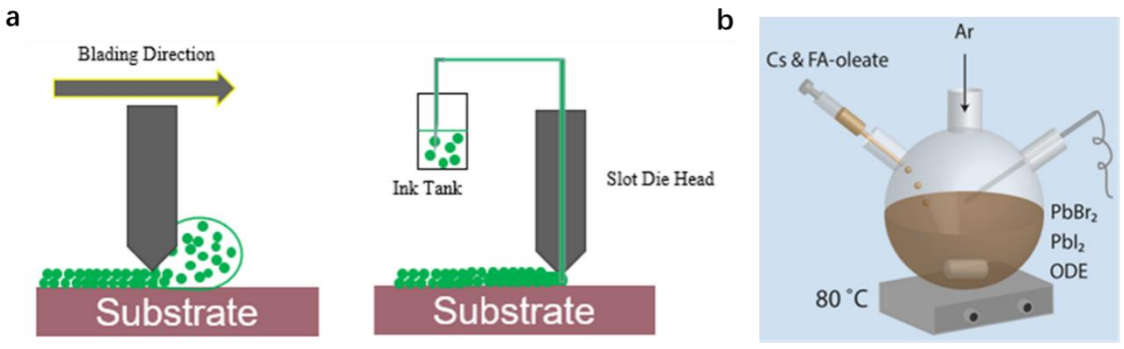

Figure 1.8 | (a) blade coating and slot die process (b) hot injection method equipment for perovskite QD synthesis(Lignos et al., 2018).

1.3 Synthesis of LHP NCs

Numerous methods have been explored to synthesise and finely control the properties of LHP NCs, such as HT, ligand assistant room precipitation (LAPR)(Search et al., 2015), ball-milling(Yun et al., 2018), sonication(Tong et al., 2016), solvothermal(Chen et al., 2017), microwave(Y. Li et al., 2018; Pan et al., 2017), and in-situ(C. Zhang et al., 2017). Each of those methods has merits and drawbacks. NCs synthesised by different methods present their unique characteristic. Researchers select synthesis methods according to the application scenarios. The widely used HT and LAPR methods are introduced in detail, while other methods are briefly presented.

Hot Injection Method. In 2015, Kovalenko and coworkers extended the hot-injection method based on previous research, enabling the synthesis of monodisperse cubic-shaped $CsPbX_3$ colloidal NCs. This milestone work built a solid foundation for subsequent studies on LHP NCs. As perovskite QDs synthesised with the hot injection

method possess relatively higher PLQY and better stability than other methods, they are suitable for fabricating LEDs(Dong et al., 2020; M. Liu et al., 2021; Wu et al., 2019). The synthesis process is illustrated in Figure 1.9. Generally, Cs_2CO_3 is utilised as a Cs precursor to react with oleic acid (OA) in octadecene (ODE) to form Cs-oleate. The Cs-oleate solution is injected under a specific temperature into the solution of $PbBr_2$, which is prepared by dissolving $PbBr_2$ powders in ODE with OA and oleylamine (OAm) as precursor ligands(Zhang et al., 2020). After reacting for 5~10 seconds, the three-neck bottle is moved into an ice water bath for cooling. Then, LHP NCs are purified and finally redispersed in hexane or octane. Additionally, organic-inorganic hybrid $MAPbX_3$ or $FAPbBr_3$ NCs are synthesised by the HT method, which uses methylamine or formamidine solutions to replace caesium oleate, adjusting the amount and ratio of precursor ligands.

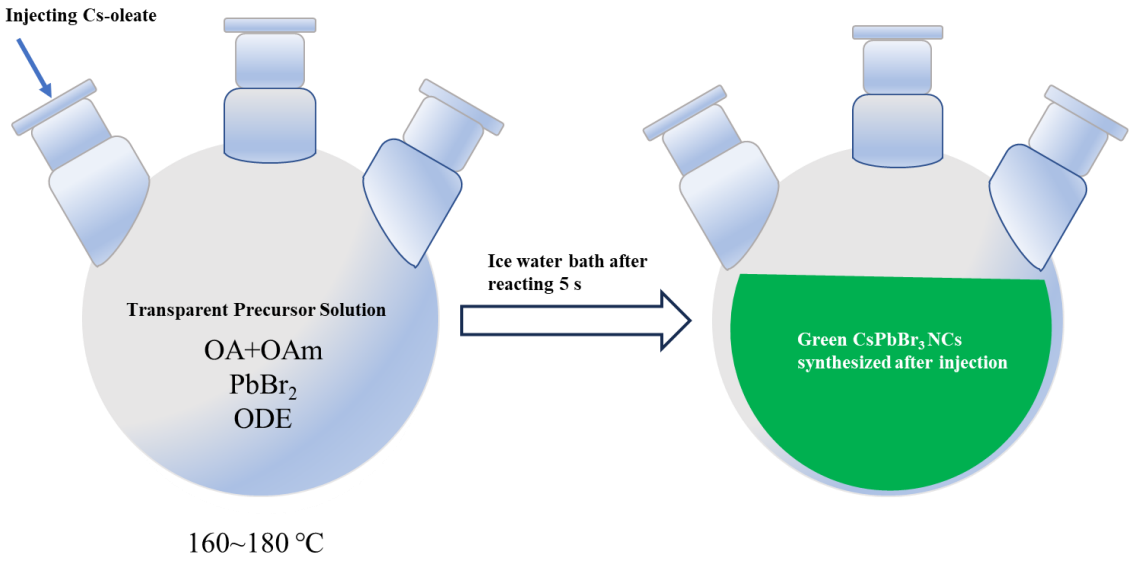

Figure 1.9 | Schematic illustration of hot injection method synthesis of $CsPbBr_3$ NCs.

When using the HT method to synthesise $APbX_3$ (where A=Cs, MA, or FA) nanocrystals, PbX_2 salt is used as halide and lead sources, which fixes Pb to X ratio, making it difficult to adjust the lead to halide ratio. The elements ratio in synthesis is not stoichiometric, which limits the control over the composition and performance of the final

product. To address this issue, researchers have used lead acetate instead of PbX_2 as the lead source to synthesise perovskite nanocrystals (PeNCs). As shown in Figure 1.10, $Pb(CH_3COO)_2$ and benzoyl halide are used as the lead and halogen sources, respectively(Imran et al., 2018a), to synthesise pure-phase all-inorganic and organic-inorganic hybrid PeNCs ($APbX_3$, where A=Cs, MA, or FA) with uniform size and excellent luminescent properties. This method is also named the three precursor methods. Other halide sources were being used. For example, lead acetate and trimethylsilyl bromide were employed to synthesise $CsPbBr_3$ nanocrystals(Zhang et al., 2020). By controlling the ratios of Cs, Pb, and Br precursors and the reaction time, pure-phase $CsPbBr_3$ with excellent optical properties were successfully synthesised.

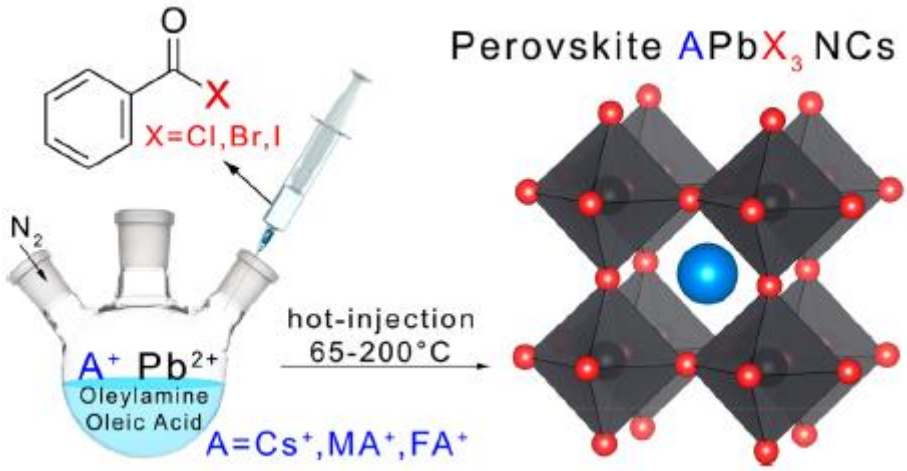

Figure 1.10 | Schematic illustration of three precursor methods synthesising perovskite quantum dots(Imran et al., 2018a).

The PeNCs synthesised via the hot-injection method exhibit uniform size and high crystallinity. Moreover, during the synthesis process, precise control over the nanocrystal size, size distribution, and morphology can be achieved by altering reaction time, synthesis temperature, and ligand concentration. However, in the typical HT method, LHP QDs quickly developed by ionic co-precipitation. LHP QDs for light-emitting diodes were synthesised by uncontrollable metathesis reactions, suffering from low product yield, nonuniform growth, and poor stability(Akkerman et al., 2022). Thus, modification and improvement from the classic HT method are necessary for synthesising stable and

efficient PeNCs.

Room Temperature Method. The reprecipitation method is a solvent displacement technique initially developed for preparing organic nanoparticle dispersions (Zhao et al., 2008). This method involves rapidly mixing a small amount of a highly concentrated precursor solution dissolved in a suitable solvent with a large amount of a poor solvent. Due to the significant difference in the solubility of the product between the appropriate solvent and the poor solvent, the rapid mixing of the two solvents changes the microenvironment of the product molecules, inducing supersaturation. The molecules are exposed to the poor solvent environment immediately, triggering nucleation and growth of molecular nanoparticles. Based on this reprecipitation method, ligands are introduced during the synthesis process to regulate crystallisation and synthesise colloidal nanoparticles. Therefore, this method is called Ligand-Assisted Reprecipitation (LARP)(Shamsi et al., 2019).

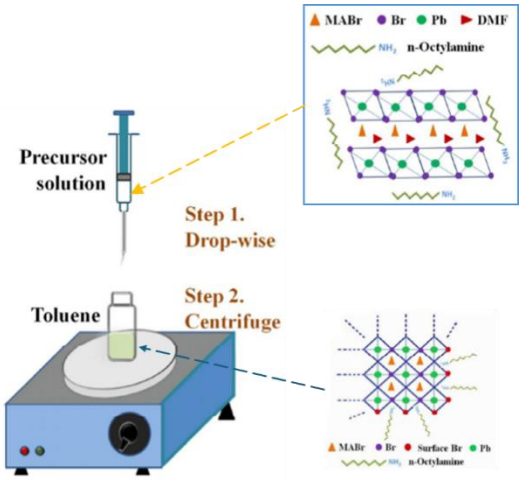

Figure 1.11 | Schematic illustration of ligand-assisted reprecipitation method to synthesise perovskite QDs(Search et al., 2015).

The LARP method commonly uses precursor salts to dissolve in suitable solvents, such as N, N-dimethylformamide (DMF), dimethyl sulfoxide (DMSO), or acetonitrile to form precursor solutions(Huang et al., 2015). Figure 1.11 shows the synthesis process of the LAPR method(Search et al., 2015). The mixtures of MABr and $PbBr_2$ salts with

ligands OA and octylamine (OTAm) are dripped into rapidly stirring toluene to mould $MAPbBr_3$ QDs. Organic amines can regulate the crystallisation kinetics of perovskite QDs, thereby controlling the size of QDs. In contrast, the primary function of carboxylic acids is to prohibit aggregation of nanocrystals to enhance QDs' stability.

Similar to the QDs' size control of the HT method, the LARP method regulates the morphology and size of perovskite QDs through synthesis parameters such as the ratio of precursors, reaction time, type of antisolvent, and the number of ligands(Sun et al., 2016). Antisolvent toluene is conducive to synthesising small square nanoparticles or nanowires (NWs), while ethyl acetate (EA) tends to form QDs, nanorods, or nanosheets(Seth and Samanta, 2016).

Although the LARP method can directly synthesise perovskite QDs on a large scale at room temperature in the air, there are some disadvantages. For example, the polar solvents used in the LARP method (such as DMF and DMSO) can damage the crystal structure of QDs (such as $CsPbI_3$ QDs). In addition, the DMF and DMSO solvents are toxic and unsuitable for large-scale industrial applications. Perovskite QDs synthesised by the LARP method possess relatively poor crystallinity due to a lack of high-temperature annealing compared to the HT method. The stability of perovskite QDs synthesised by the LARP method is also doubted to be applied to LEDs as devices produce lots of joule heat when operating.

1.4 Stability of LHP QDs

Although LHP QDs have been proven to be excellent semiconductor materials, the stability problem inhibits their commercial applications. The LHP QDs manifest classic ionic crystal features caused by the sizeable atomic spacing, which differs from the compact and stable oxide perovskite(X. K. Liu et al., 2021). The ionic feature of perovskite QDs is the reason for insufficient polar solvent resistance. The active energies needed for reactions in LAPR methods can be ignored, and the dynamic feature of those reactions corresponds with their ionic feature, which means a high reaction rate. Additionally, the composition of LHP QDs can be easily changed through ion

exchange(Chiba et al., 2018). The ionic crystal characteristics are detrimental to the structural stability of LHP QDs.

Interface Instability of LHP QDs. LHP QDs are soft lattice materials that are ionic crystals. LHP QDs quickly degrade or lose ligands due to unstable crystal structures or highly dynamic surfaces (De Roo et al., 2016), inducing fluorescence quenching as manifested in Figure 1.12. The method used to synthesise PeNCs employs weak ligands, OA and OAm. A mutual equilibrium exists between the soft Lewis acid OA and soft Lewis base OAm(Almeida et al., 2018). Molecular and ionised forms of OA and OAm in ODE solvent are presented at room temperature. Consequently, the ligands desorption of perovskite QDs occurs during the isolation and purification process, resulting in lousy ink stability and quick PLQY decrease in storage. This detachment can even cause the entire structure to be damaged, with the NCs merging into bulk polycrystalline material. Therefore, OA/OAm ligands are easily detached from the perovskite surface in the solution, causing a highly dynamic surface(De Roo et al., 2016).

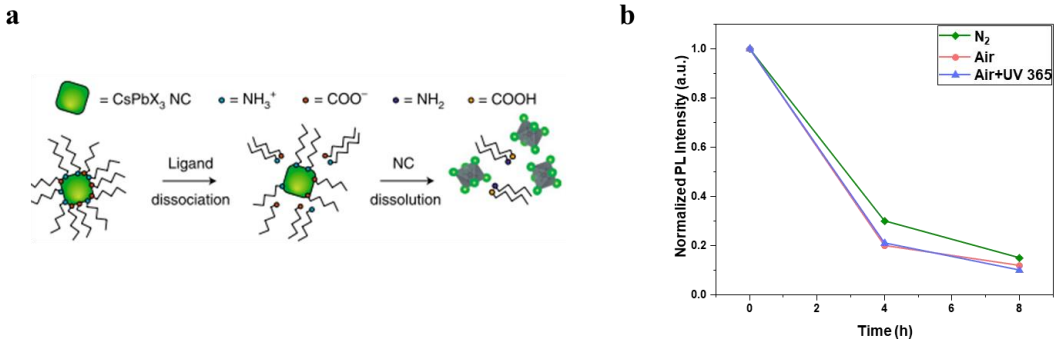

Figure 1.12 | (a) Schematical illustration of highly dynamic surface ligands (Akkerman et al., 2018), (b) PL intensity decay of OA/OAm PeNC films under different environment conditions.

Environmental Instability of LHP QDs. LHP NC films are sensitive to heat(M. Liu et al., 2021), oxygen, moisture(H. Huang et al., 2017), and continuous ultraviolet (UV) irradiation(S. Huang et al., 2017). When irradiated under UV, $CsPbBr_3$ NCs are photoexcited (Figure 1.13a). The generated charges diffuse to the surface due to the high

carrier mobility within NCs and rapid interfacial charge transfer. Subsequently, these charges are captured by ionic ligands, causing ligand detachment on the NC surface. The ligand loss results in an unprotected surface, ultimately leading to the aggregation of neighbouring particles(Chen et al., 2016). When oxygen diffuses into the perovskite lattice with light irradiation, superoxides are produced on the surface (Figure 1.13b). These superoxides cause the deprotonation of methylammonium (CH_3NH_2) cations, leading to the structural collapse of the perovskite(Aristidou et al., 2017). This degradation results in the formation of layered PbI_2, H_2O, I_2, and CH_3NH_2. With a small amount of vapour, the perovskite reacts with water to produce a monohydrate, which can reversibly dehydrate (Figure 1.13c). As the hydration process continues, dihydrate forms along with the production of PbI_2. The formation of PbI_2 leads to phase separation, further accelerating the hydration process and ultimately causing the degradation of the perovskite(Leguy et al., 2015). Moreover, for PeNCs, water molecules can cause surface ligand loss, inducing damage to the NC structure.

For electroluminescence application of LHP NCs, relatively good environmental stability or storage stability is a prerequisite because LHP NC solutions are often stored in the air before device fabrication. In addition, resistance to thermal fluorescence quenching is also vital for LHP NC films as the temperature of LHP NC films is often elevated to at least 60 ℃ during the device fabrication process, such as annealing, evaporating organic electron transport layers (ETL) and metal electrode.

Strategies for improving stability. Many efforts are made to improve the stability of LHP NCs, such as doping A site or B site cations(Song et al., 2018b; Ya-Kun Wang et al., 2021), employing robust ligands(Krieg et al., 2018; Song et al., 2018a), incorporating additives(Brown et al., 2019), cross-linking the film(Chen et al., 2020; Jang et al., 2021), and constructing metal-organic frameworks(Tsai et al., 2021).

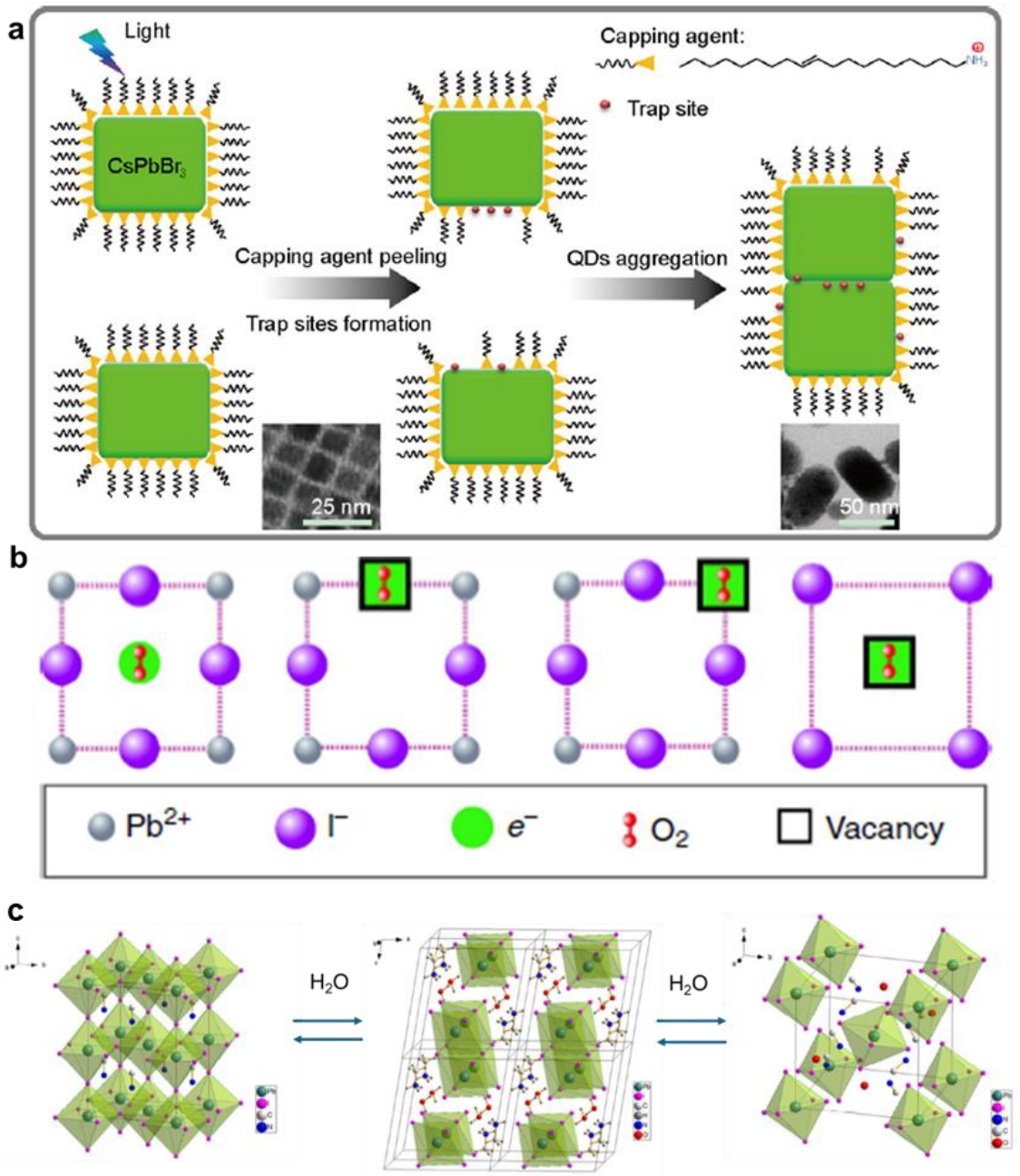

Figure 1.13 | Schematic illustration of degradation mechanisms of perovskite NCs with different environmental conditions (a) light(Chen et al., 2016), (b) oxygen(Aristidou et al., 2017), (c) water(Leguy et al., 2015).

Composition engineering, surface engineering, and encapsulation approaches have been used extensively to improve the LHP QDs' stability. Zeng, etc., doped the $CsPbBr_3$ QDs with a small number of formamidine ions (FA^+ ions) and increased the film PLQY of the LHP QDs from 46% to 61%. FA^+ ions have a larger ion radius than Cs^+. According

to equation 2.1, FA^+ ions match with lead bromide octahedrons better than Cs^+. Therefore, the $CsPbBr_3$ NCs doped with FA^+ ions have better crystal structure stability than $CsPbBr_3$ NCs. In addition, three kinds of ligands, tetraoctylammonium bromide (TOAB), didodecyldimethylammonium bromide (DDAB), and octanoic acid were employed to synthesise $CsPbBr_3$ QDs. TOAB and DDAB can efficiently passivate defects of $CsPbBr_3$ QDs, improving the PLQY of $CsPbBr_3$ QDs.(Imran et al., 2019; Song et al., 2018b) Doping cations can increase the structure stability of LHP NCs or passivate surface defects, which increase PLQY and device EQE. Nevertheless, this strategy does not exhibit the advantage of enhancing device stability.

The metal-organic frameworks method and cross-linked agents introduce many insulating agents, affecting the charge transport ability of perovskite film. This results in relatively high turn-on voltage and produces lots of joule heat during operation(Jang et al., 2021; Tsai et al., 2021; Wei et al., 2020).

Potent ligands, such as zwitterionic ligands, phosphoric acid, and dioctylamine, are employed as surface ligands to replace weakly binding OA/OAm ligands, which can tightly bind to the perovskite surface and improve the storage stability of perovskite QDs(Krieg et al., 2019, 2018). Franziska Krieg and his coworkers first proposed zwitterionic ligands as potent ligands for perovskite QDs (Figure 1.14)(Krieg et al., 2018). The potent ligands are introduced with three-precursor approaches(Imran et al., 2018b; Krieg et al., 2018). The three-precursor method synthesised LHP NCs show lower PLQY than the $PbBr_2$ precursor-based hot injection method. This class of ligands allows for the isolation of perovskite QDs with several times of precipitation/redispersion process while maintaining a high PLQY above 90%. The purified NCs were well dispersed with narrow size distribution and high reaction yield. The compacted film formed with these NCs exhibited effective charge transport and high film PLQY. LHP NCs synthesised with robust ligands exhibit good environmental stability and shape uniformity. PeQD ink showed good storage stability for up to 1 month. However, the halide source used in the three precursor methods is often dangerous and very reactive (for example, bromine),

which makes it challenging to ensure experimental safety. Additionally, the device performance of the three precursor approaches is far from that of the classic hot injection method(Zhao et al., 2020).

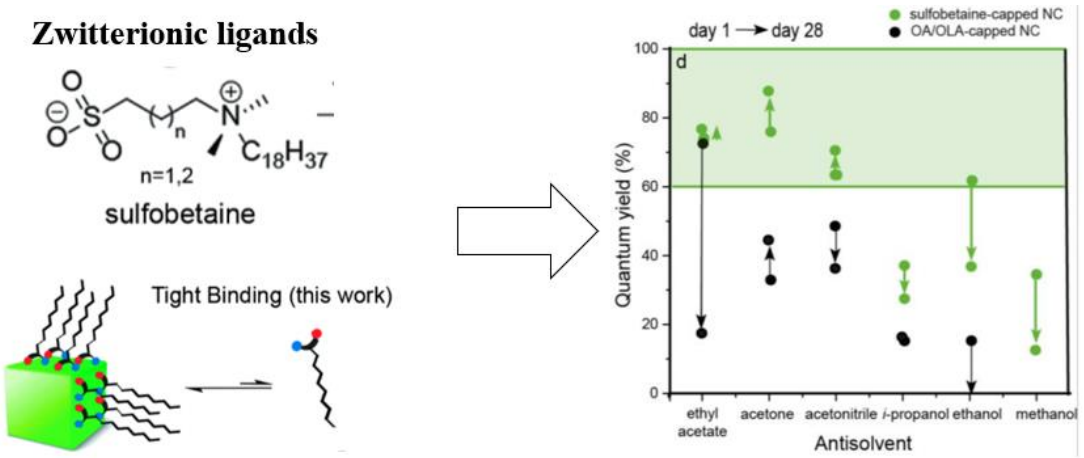

Figure 1.14 | Zwitterionic ligands and schematic illustration of tightly binding surface ligands, the storage stability of the synthesised perovskite quantum dots(Krieg et al., 2018).

Alivisatos' group proposed that phosphoric acid can enormously enhance PLQY and eliminate the halide vacancy of the perovskite QDs. They proposed strategies for post-synthesis treatment with potent ligands to get defect-free perovskite quantum dots. In addition, Tan et al. employed octyl phosphonic acid with TOPO as a precursor to synthesise perovskite quantum dots, which claims good polar solvent resistance with device EQE of 6.5% in 2018. The PLQY of synthesised perovskite QD solution was up to 80%, but the perovskite QDs were difficult to disperse in a nonpolar solvent(Brown et al., 2019; Tan et al., 2018).

Chenhao Bi and his coworkers provided a new strategy for synthesising pure blue $CsPbBr_3$ QDs as small as 4 nm (Figure 1.15)(Bi et al., 2021)—the synthesised small $CsPbBr_3$ QDs with near unit PLQY and good environmental stability. In the synthesis process, hydrogen bromide (HBr) was used to etch the perovskite quantum dot surface capped with OA/OAm ligands to eliminate the imperfect octahedrons on the surface. As

a result, there were no Pb vacancies on the perovskite surface as the surface Pb defects and excessive carboxylate ligands were removed. Therefore, it was easy to introduce other potent ligands to the perovskite QDs surface. Finally, they introduced didodecylamine (DDDAM) and phenethylamine (PEA) as surface ligands for the small $CsPbBr_3$ perovskite QDs. Moreover, these two potent ligands can strongly bind to the perovskite surface and exchange the original long-chain weak ligands. In summary, pure blue perovskite QDs with PLQY of 97% were grained. The perovskite QDs also showed excellent stability in ambient conditions.

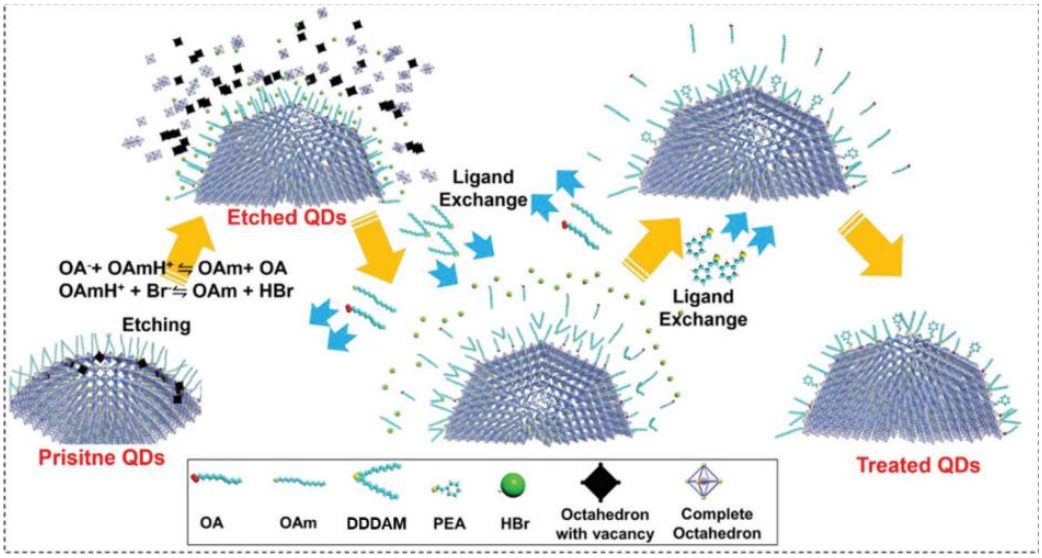

Figure 1.15 | Schematic illustration of synthesis procedures for blue perovskite quantum dots(Bi et al., 2021).

The stability of perovskite nanocrystals synthesised with additives is not satisfactory. Although those strategies improved the environmental stability of LHP NCs and significantly increased the external efficiency of PeQLEDs, PeQLEDs' operation stability is not satisfactory.

1.5 Charge Transport Ability of LHP NCs with Different Ligands

In perovskite QDs, there is a trade-off between stability and conductivity. While long alkyl chains or alkoxysilane molecular ligands can effectively passivate perovskite NC defects to improve optical properties and stability, their insulating nature restricts

electronic coupling between perovskite NCs, reducing the charge transport ability of the NCs(Vickers et al., 2018). This hinders perovskite NCs' application in optoelectronic devices.

In perovskite-based optoelectronic devices, achieving high performance depends on perovskite NCs that are both stable and possess excellent charge transport properties. In PL applications (Figure 1.16a), for instance, in down-conversion LEDs where perovskite NCs are used as backlight materials, the device performance depends on the optical and structural stability of the perovskite NCs(Kovalenko et al., 2017). In EL applications (Figure 1.16b), where perovskite NCs serve as the emissive layer, not only are superior luminescent properties and good charge transport capabilities required to ensure high EQE and brightness, but strong stability is also necessary to ensure reliable device fabrication and operation. Thus, obtaining perovskite NCs with excellent stability and charge transport performance can significantly advance the development of efficient LEDs, photodetectors, lasers, and other optoelectronic devices.

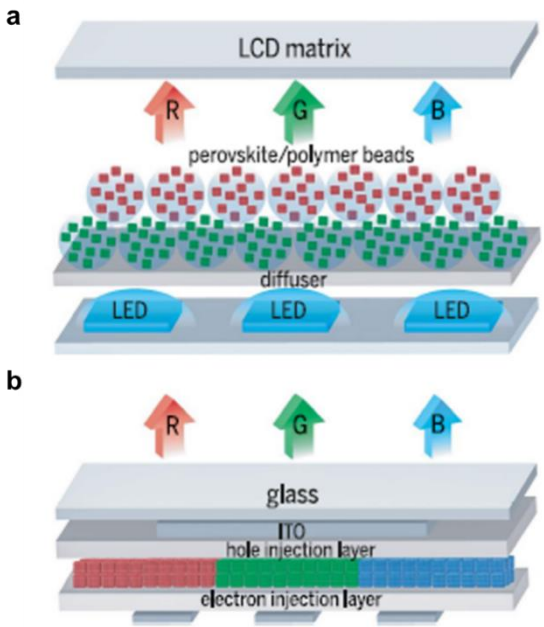

Figure 1.16 | Schematic illustration of LED applications of perovskite NCs (a) PL, (b) EL(Kovalenko et al., 2017).

For optoelectronic devices based on perovskite NCs, the charge transport properties

of nanocrystals significantly impact device performance. Poor charge transport can hinder carrier movement, dramatically reducing device efficiency. For example, in photovoltaic devices, this manifests as low photocurrent and, consequently, lower energy conversion efficiency. In LED devices, this leads to high turn-on voltage, low brightness, and low EQE. Perovskite materials are semiconductors which exhibit excellent charge transport properties. However, the ligands of perovskite NCs typically contain insulating long-chain alkyl groups. Therefore, modulating surface ligands is the key to improving the charge transport properties of perovskite NC.

Optimisation of ligands density. Li et al. proposed using a hexane/ethyl acetate mixed solvent during purification to optimise the $CsPbBr_3$ NC ligand density to enhance charge transport ability (Figure 1.17)(Li et al., 2017). During the purification process, modifying the number of purification cycles or using solvents with different polarities to regulate ligand density can enhance the charge transport properties of perovskite NCs. However, reducing the surface ligands excessively creates surface defects, which deteriorates the optical properties of the nanocrystals. Therefore, balancing optimal charge transport and sufficient surface passivation is vital. Effective carrier injection and defect passivation should be considered comprehensively.

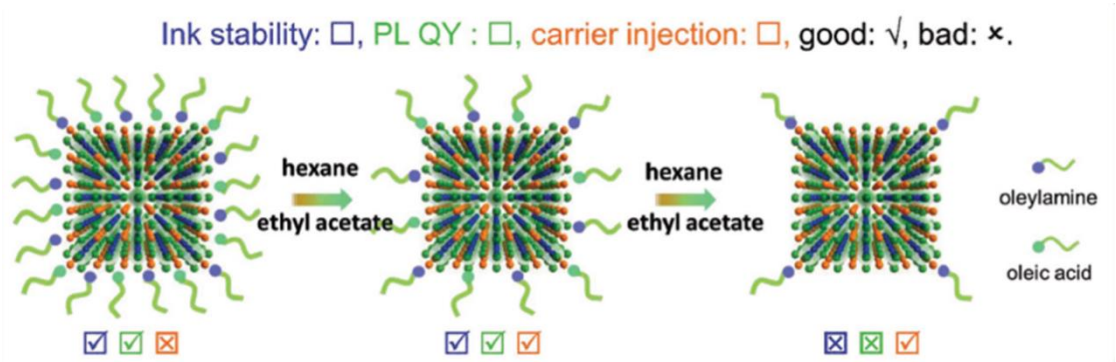

Figure 1.17 | Schematic illustration of adjusting ligand density of perovskite NCs by the purification process(Li et al., 2017).

Modification of ligand length. Using shorter chain-length ligands instead of long

alkyl chains can reduce obstacles to charge transport(Pan et al., 2016). Researchers have proposed regulating ligand length to enhance the charge transport properties of NCs by ligand exchange (Figure 1.18). In addition to the post-treatment of NCs, adjusting ligand chain length during the synthesis process is another effective method to enhance the charge transport properties of NCs. Although reducing the ligand chain length can improve the charge transport properties of NCs, it can cause NC aggregation if the ligands are too short, which deteriorates optical properties. Therefore, selecting ligands with the proper chain length is essential to balance optical properties and charge transport ability.

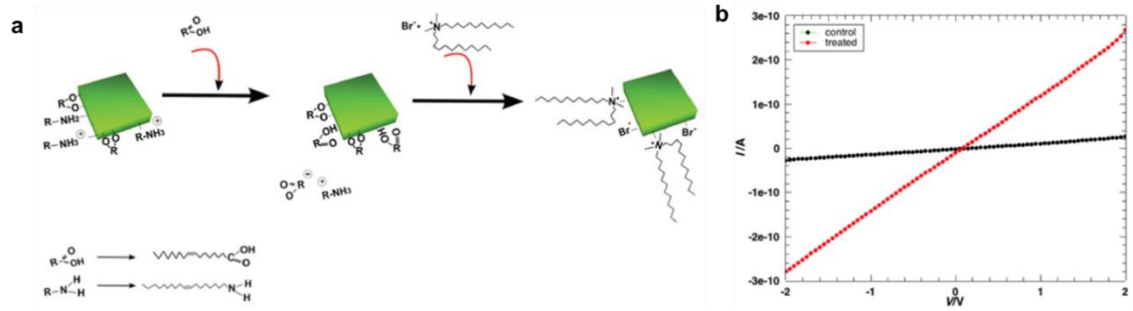

Figure 1.18 | Influence of ligand chain length on conductivity of perovskite NCs (a) schematic illustration of ligands exchange with short chain length ligands (b) comparison of measured current-voltage (*I-V*) curve of different perovskite NC films with different ligand chain length(Pan et al., 2016).

Introduction of Aromatic Ligands. Aromatic ligands with π-π conjugation effects can facilitate charge transport, improving the charge transport properties of NCs(Dai et al., 2018; Vickers et al., 2018). Li et al. used phenethylammonium bromide (PEABr) for ligand exchange with pristine $CsPbBr_3$ NCs (with OA/OAm ligands), as shown in Figure 1.19(G. Li et al., 2018). The resulting $CsPbBr_3$ NCs were capped with PEA ligands called PEA-EX $CsPbBr_3$ NCs. The LEDs based on the pristine $CsPbBr_3$ NCs had a turn-on voltage of 4.5 V, while those based on PEA-EX $CsPbBr_3$ NCs had a reduced turn-on voltage of 3.0 V, indicating that ligand exchange with aromatic ligands can enhance the conductivity of NC films. Additionally, the authors applied this ligand exchange method

to $CsPbI_3$ NCs. LEDs based on PEA-EX $CsPbI_3$ nanocrystals achieved a maximum brightness of 1444 $cd \cdot m^{-2}$ and a peak EQE of 14.08%, significantly higher than the performance of LEDs based on pristine $CsPbI_3$ NCs (188 $cd \cdot m^{-2}$ and 2.45 $cd \cdot A^{-1}$).

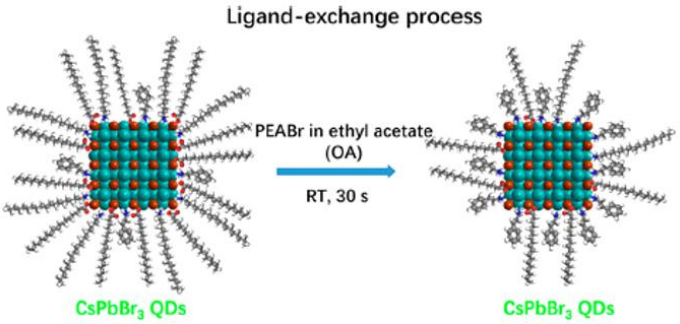

Figure 1.19 | Schematical illustration of ligands exchange with PEABr ligands(G. Li et al., 2018).

In summary, optimising ligand density, regulating ligand length, and introducing aromatic ligands are three effective strategies for enhancing the charge transport properties of halide perovskite NCs. This improvement in carrier transport can substantially boost the performance of LEDs.

1.6 Device structure of PeQLEDs

For EL applications, the commonly utilised device structure is indium tin oxide (ITO) glass/ Poly[*N*,*N*′-bis(4-butylphenyl)-*N*,*N*′-bis(phenyl)-benzidine] (ploy-TPD) /active layer (perovskite QDs)/(1,3,5-Benzinetriyl)-tris(1-phenyl-1H-benzimidazole) (TPBi) / Lithium fluoride (LiF)/aluminium (Al)(Song et al., 2018b, 2015). However, the hole transport layer poly-TPD possesses a low hole transport mobility of 10^{-4} $cm^2 \cdot V^{-1} \cdot s^{-1}$. Additionally, the electron mobility of TPBi is as low as in the range from 10^{-5} $cm^2 \cdot V^{-1} \cdot s^{-1}$ to 10^{-4} $cm^2 \cdot V^{-1} \cdot s^{-1}$ (Fang et al., 2021). The low charge transport ability of the transport layers leads to high turn-on voltage, low current density, and low EQE. Consequently, the EQE of PeQLED with this device structure is lower than 10%. Moreover, TPBi is a kind of small organic molecule that is sensitive to oxygen and water. Those devices employing TPBi as an electron transport layer quickly produce dark spots, as shown in Figure 1.20.

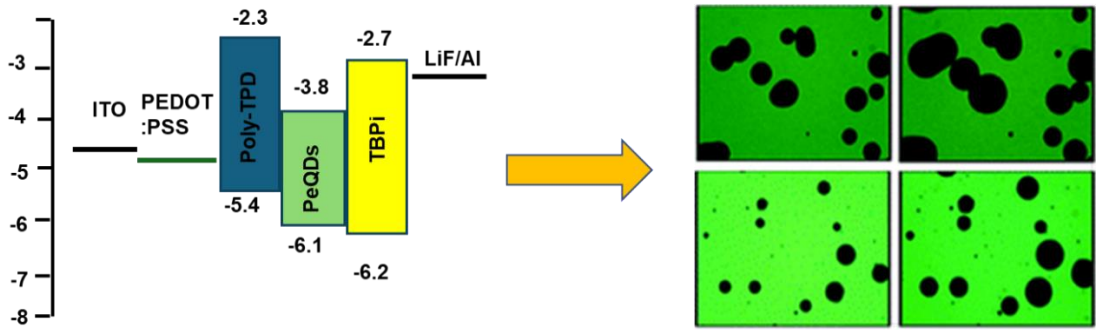

Figure 1.20 | Band diagram of the classic PeQLED structure and dark sports produced when devices are exposed to ambient conditions.

Compared to poly-TPD and TPBi, other organic carrier transport layers have carrier mobility and band energy suitable for perovskite QLEDs, such as PTAA and PO-T2T. The comparison of those organic transport layers of the charge mobility and band energy is exhibited in Table 1.1. Perovskite QLEDs can achieve high EQE by using PTAA with PO-T2T. In addition, the stability of these transport layers is much better than poly-TPD and TPBi. Besides, the mismatch of band energy level is one of the most important reasons for charge accumulation in PeQLEDs, leading to fluorescence quench and material degradation. Carrier mobility and energy levels of transport layers are essential for the charge balance of devices. As electrons are major carriers in PeQLEDs, electron injection is usually controlled by interface layers to ensure the charge balance of devices. The corresponding device structure and device performance are exhibited in Figure 1.21.

Table 1.1 | Carrier mobility and energy levels of different organic transport materials(Chen et al., 2009; Yanping Wang et al., 2021).

Charge transport layer	Mobility ($cm^2 \cdot V^{-1} \cdot s^{-1}$)	HOMO (eV)	LUMU (eV)
PTAA	5×10^{-3}	-5.3	-2.6
Poly-TPD	10^{-4}	-5.4	-2.3
TPBi	3.3×10^{-5}	-6.2	-2.7
PO-T2T	$1.7 \times 10^{-3} \sim 4.4 \times 10^{-3}$	-6.6	-3.3

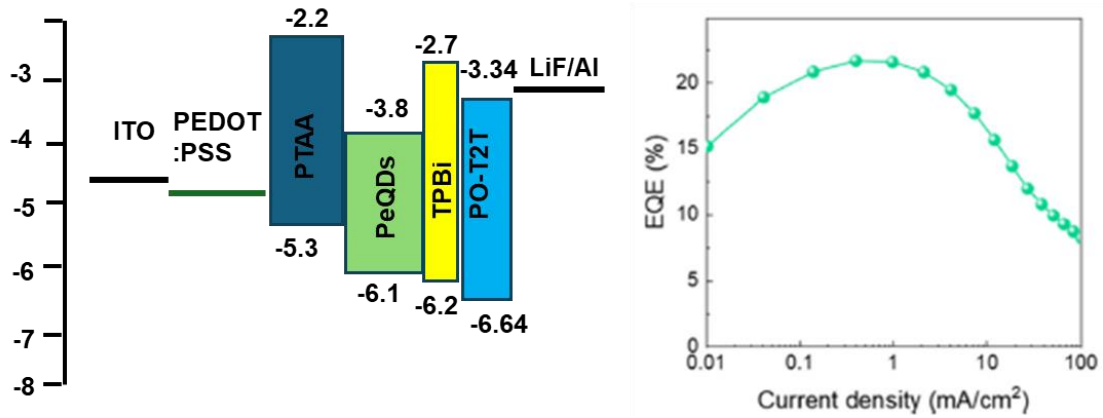

Figure 1.21 | Diagram of PeQLED device structure with high mobility transport layers("TPBI Xi'an Yuri Solar Co., Ltd," 2025).

1.7 Summary

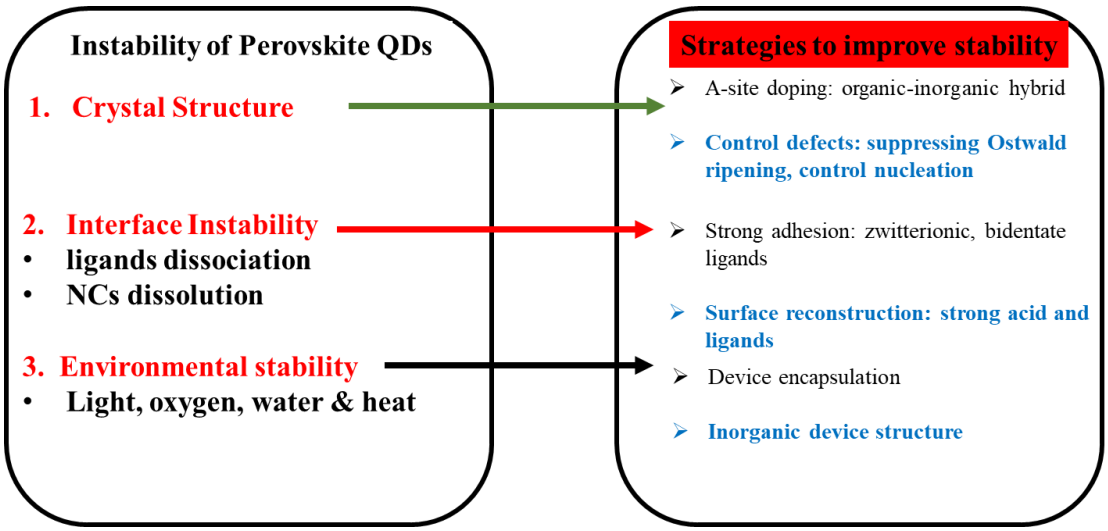

Figure 1.22 | Instability of LHP QDs and strategies for enhancing stability.

In summary, LHP QDs are potentially active materials for next-generation displays due to excellent photoelectric properties and low-cost fabrication processes. However, perovskite NCs suffer from ligand loss and degradation in the ambient environment because of their ionic crystal nature. The instability of perovskite QDs and PeQLEDs inhibits commercial applications. Although researchers have made efforts on synthesis, crystal structure, ligands, and encapsulation to improve the stability of perovskite QDs and PeQLEDs (Figure 1.22), there are some problems, such as low polar solvent

resistance, the balance between charge transport ability and PLQY, and thermal-induced fluorescence quenching. Achieving high EQE and operation stability is challenging.

To solve those problems, strategies are proposed to improve the stability of synthesised LHP NCs and design suitable device structures according to synthesised LHP NCs (Figure 1.23), finally achieving efficient and stable PeQLEDs. The crystallinity of perovskite NCs can be improved by controlling nucleation and growth. In-situ PL measurements are applied to explore the nucleation and growth process. The NCs' crystallinity is characterised by TEM and X-ray diffraction (XRD) spectra. Potent ligands can form a good shell to protect the perovskite NCs from polar solvents and passivate different vacancies on perovskite NC surfaces. Different charge transport layers that are stable and inert in ambient environments can be employed to improve the device carrier transport ability and match energy levels. Moreover, inorganic transport layers that are stable and efficient can replace those organic transport layers(Qian et al., 2010; Shi et al., 2018; Tian et al., 2021).

Herein, the synthesis method is improved and modified from the hot injection method. The modified methods can simultaneously achieve high PLQY and excellent stability. Good NCs' crystallinity and narrow size distribution are attained by controlling precursor reactivity in the solution system. The balanced reactivity of CsBr and $PbBr_2$ means that there are few defects in the formed $CsPbBr_3$ NCs from the thermodynamics perspective. Various potent ligands are used to control nucleation and growth. The potent ligands can be classified as follows: multidentate ligands, short-chain amines, phosphoric acid, and various strong acids like sulfonic acid. As illustrated in Figure 1.23, the blue fashion of fast nucleation and suppressed Ostwald ripening is preferred, often forming high crystal-quality perovskite quantum dots(Green et al., 2020). The left image shows various ligands used for perovskite synthesis, including weak and strong ligands(Zhang et al., 2020). The precursor ligands significantly influence the nucleation of perovskite nanocrystal synthesis. Strong precursor ligands generally decrease the reactivity of metal salt. An in-situ PL system is used to investigate the nucleation and growth mechanism of

different precursors, as it is easy for an in-situ PL system to collect particle size and morphology data by analysing the emission spectra.

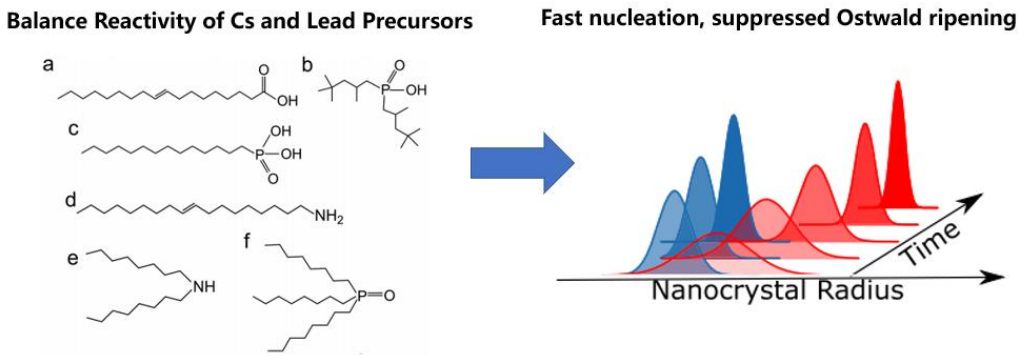

Figure 1.23 | Ligands used for synthesis and schematic illustration of nucleation and growth process of perovskite quantum dots.

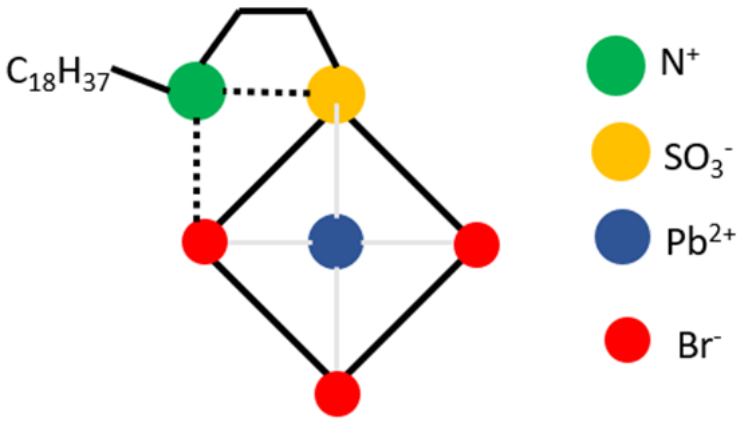

Figure 1.24 | Schematic illustration of chelation effect of zwitterionic ligands on perovskite quantum dot surface.

Potent ligands, such as zwitterionic ligands, amino acids, sulfonic acids, amines, and inorganic salts, are applied to passivate and reconstruct the surface. Potent ligands are tightly bound on the NC surface to avoid ligand loss. For example, zwitterionic ligands possess a chelation effect, as shown in Figure 1.24. A safe and efficient method to introduce potent ligands is developed in this thesis, which reacts strong ligands with strong acids to form a new precursor. The resurface agents are added after nucleation as

in-situ ligands exchange. This method is different from customarily reported post-treatment. Inorganic salts are added in the purification process to passivate QDs and prohibit Ostwald growth. Consequently, the perovskite QDs surface can finally form a compact surface ligand shell with good charge transport ability. The perovskite QDs also exhibit excellent stability in ambient conditions.

From the device perspective, many designs, such as double ETL or HTL(Fang et al., 2021; Sun et al., 2020), insert interface layers(Dai et al., 2014), crosslinked HTL(Tang et al., 2020; L. Xie et al., 2022), and mixed HTL(Zhang et al., 2022) have been successfully applied to QLEDs to improve device performance. Those device designs can also be applied to enhance the performance of PeQLEDs. Double ETL designs are used in this thesis to balance the device charge. 3,3'-[5'-[3-(3-pyridinyl)phenyl][1,1':3',1"-terphenyl]-3,3"-diyl]bispyridine (TmPyPB) are explored for the double ETL device structure.

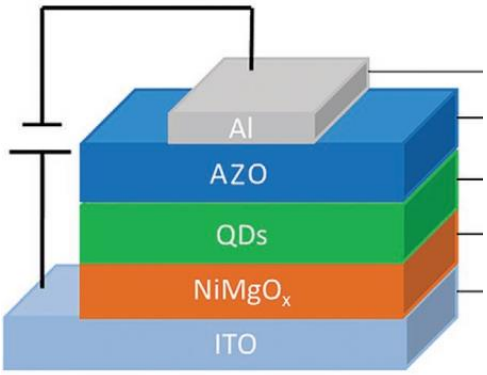

Figure 1.25 | Schematic illustration of all inorganic processable QLED structures.

Inorganic transport layers, such as WS_2 and ZnO nanoparticles, are stable to ambient conditions and have high charge mobility(Lin et al., 2019; X. Zhang et al., 2017). It is easy for metal oxide nanoparticles to tune the band gaps and control carrier mobility by doping. For instance, various metals are doped into ZnO nanoparticles, such as Al, Li, Mg, Cu, etc. (F. Wang et al., 2021). The ZnO nanoparticles have good thermal and operation stability, high electron mobility, and good energy levels that match QDs. ZnO nanoparticles are widely used as ETL for QLEDs and achieve success (Figure 1.25)(F. Wang et al., 2021). Modified ZnO nanoparticles doped with Mg are explored as ETL for

PeQLEDs. Nevertheless, the surface defects and hydroxide radicals cause fluorescence quench of QDs(Liu et al., 2022; Nguyen et al., 2021). To solve this problem, a buffer layer is inserted between the oxide transport layer and perovskite QD film. The insert buffer layer can relieve the exciton quench on the interface between the transport layer and perovskite QD film.

1.8 Objectives

This thesis aims to delve deeply into the passivation, nucleation, and growth mechanisms of PeQD synthesis to address the issues of usable $CsPbX_3$ QDs in EL applications. The principal purpose is to enhance the stability and efficiency of PeQLEDs from aspects of both materials and device structure design.

A comprehensive literature review of PeQD synthesis and PeQLEDs is summarised, focusing on uncovering underlying principles of materials synthesis and device structure design. Extensive experiments are conducted to investigate the optical-electronic properties of PeQDs, including stability under various conditions. A profound understanding of the instability of PeQDs and devices is established.

Strategies are proposed for synthesising stable, conductive, and efficient $CsPbX_3$ QDs. High-colour purity perovskite QDs for display technologies are synthesised. The fabricated PeQLEDs achieve high efficiency and operation lifetime.

1.9 Thesis Structure

The thesis has 6 chapters. Chapter 1 is a literature review that introduces QDs and QLEDs. The chapter reviews QDs' history, applications, development, and characteristics. The chapter describes the crystal structure, composition, synthesis, and optoelectronic properties of LHP NCs. The instability and charge transport ability problems of LHP NCs are analysed. Strategies for enhancing stability and charge transport ability are introduced, such as A site doping, ligands exchange, and device encapsulation. Inspired by those strategies, I propose improving the crystallinity of LHP NCs by controlling nucleation and growth. In addition, several substantial or short-chain length ligands are employed to

replace OA/OAm ligands and enhance the charge transport ability of LHP NCs. Inorganic and stable organic charge transport layers are designed to improve device performance in this thesis.

Chapter 2 is methodology. The materials, synthesis methods, equipment, and various characterisations are introduced in detail here. $CsPbBr_3$ and $CsPbI_3$ QDs are synthesised with different treatments. This section describes the characterisation of nucleation, morphology, crystal structure, and chemical binding of NCs. Except for experiments, characterisation, simulation for ligand binding, and device outcoupling are also carried out.

Chapter 3 is the result of green $CsPbBr_3$ QDs. This section focuses on developing HT methods for high-performance LHP NCs. This section explores different synthesis strategies to improve the NCs' quality. The nucleation and growth process of NCs is controlled by using different precursor ligands and adding resurface agents. The influence of different ligands is investigated. The stability and optoelectronic properties of LHP NCs are systematically studied. The LHP NCs' device performance is measured.

Chapter 4 is the result of pure red $CsPbI_3$ QDs. This section aims at fabricating high-performance pure red $CsPbI_3$ QLEDs. This section improves the HT method to synthesise pure red $CsPbI_3$. The growth of $CsPbI_3$ QDs is controlled by using strong acid and inorganic ligands in synthesis and purification. The section also investigates the influence of different ligands on size control. The ligand binding strength is characterised both experimentally and theoretically. The stability of synthesised small-size pure red $CsPbI_3$ QDs is explored. The devices fabricated by those QDs are measured.

Chapter 5 is the device structure design research of PeQLEDs. This section describes strategies to improve the performance of PeQELDs in this thesis, such as interface modification, multi-transport layer design, and device outcoupling simulation. In the section, inverted device structures are employed to construct the S-QLED structure to improve device stability. Synthesis of ZnO nanoparticles is explored by doping Mg. This section also investigates different solvents for dispersing ZnO nanoparticles. The

influence of ZnO solvents on the optical properties of LHP NCs is also investigated.

Chapter 6 is a summary and outlook of the research. This section summarises the works of the previous three chapters and offers advice for future research.

Chapter 2. Methodology

2.1 $CsPbBr_3$ QD synthesis and device fabrication

The method for LHP NC synthesis in this thesis is modified from the classic HT method. As shown in Figure 2.1, there are two routes for synthesis improvement. One route uses the precursor ligand bis(2-ethylhexyl) phosphate (DEHPA) to replace OA ligands. Resurface agents are used in both routes for LHP NCs passivation and controlling growth. Octanoic acid (OTAc)/ octylamine (OTAm) partially replaces OA/OAm ligands in the second route. The synthesis method in this section is employed in Chapters 3 and 5.

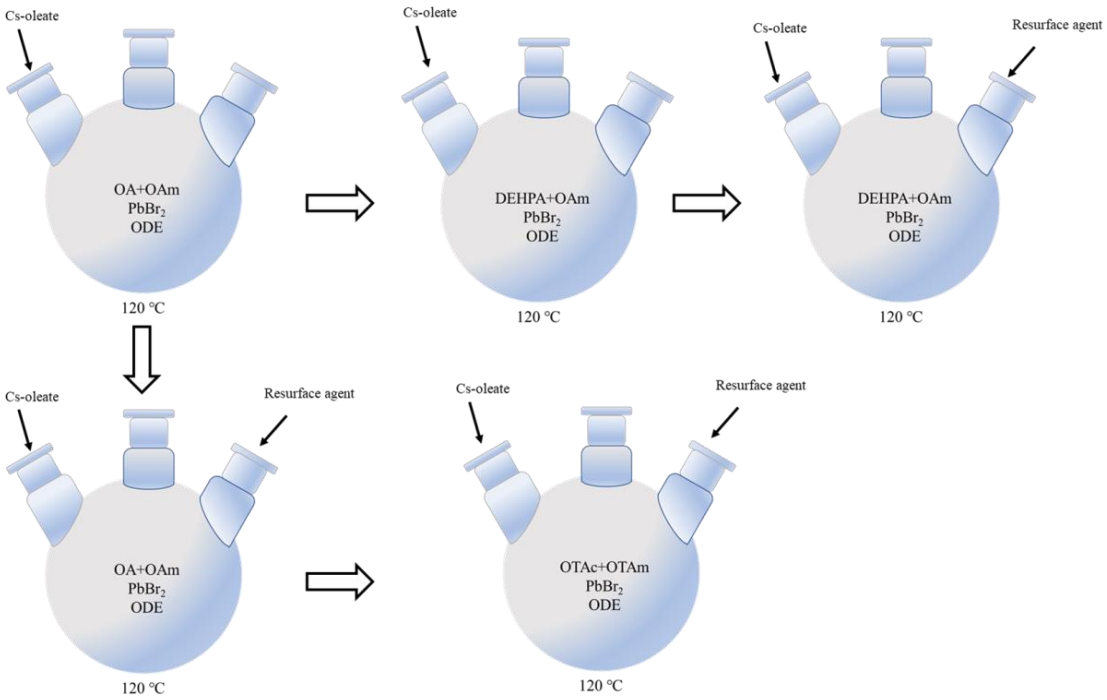

Figure 2.1 | Illustration of green $CsPbBr_3$ LHP NC synthesis with different ligands or resurface agents.

Materials: Cesium carbonate (Cs_2CO_3, Sigma-Aldrich 99.995%), oleic acid (OA, Sigma-Aldrich 90%), oleylamine (OAm, Aladdin 90%), octanoic acid (OTAc, Aladdin, 99%), octylamine (OTAm, Aladdin, 99%), octylphosphonic acid (OPA, Aladdin, 97%), 4-

Fluorophenethylamine (4-FPEA, Aladdin 90%), lead (II) bromide ($PbBr_2$ Aladdin 99.999%), 1-octadecene (ODE, Sigma-Aldrich 90%), Bis(2-ethylhexyl) phosphate (DEHPA, TCI 97%), dioctylamine (DOAM, Sigma-Aldrich 97%), didodecylamine (DDDAM, TCI 97%), 2-Phenethylamine (PEA, Aladdin, 98%), hydrogen bromide (HBr, alfa), hexane (Aladdin 99%), methyl acetate (MeOAc, Aladdin anhydrous 99.5%), ethyl acetate (Aladdin anhydrous 99.5%), 3-(N,N-dimethyloctadecylammonio)propanesulfonate (Aladdin, 99.8%, abbreviation C_3-S or ASC18), octane (Aladdin 99%), mesitylene (Aladdin 99%), chlorobenzene (CB, Mackin, 99.8%), polymethylmethacrylate (PMMA, Sigma-Aldrich); (1,3,5-Benzinetriyl)-tris(1-phenyl-1H-benzimidazole) (TPBi), 2,4,6-tris(3-(diphenylphosphoryl)phenyl)-1,3,5-triazine (PO-T2T, 99.5%), Lithium fluoride (LiF) are from Xi'an Polymer Light Technology. Argon, Indium tin oxide (ITO) glass, UV epoxy resin (Nagase, XNR5516Z(C)-SA1), capping glass, nylon organic solvent filter (0.22 μm).

Equipment: three-necked round bottom flasks (50 ml, 100 ml, Synthware), flasks (100 ml, Synthware), Schrenk Line (Synthware), temperature controller (J-KEM, Gemini, Type J, Chemglass, CG-3209-02), fume hood, magnetic stirrer (IKA, C-MAG MS 7), magnetic heating stirrer (IKA, C-MAG MS 7), anti-explosion refrigerator, pipettes (IKA, 10 μL, 100 μL, 200 μL, 1000μL), injection syringe (KDL, 1 mL, 2 mL, 5 mL, 10 mL), syringe needles (KDL, 1.6×38mm/0.9×80mm), rubber stopper (Synthware), filters (Thermo Fisher, Target 2), heating plates (JW-350BP, Junwei Tech), heat gun (Hitachi, RH600T), centrifugal machine (Eppendorf Centrifuge 5430), vacuum pump, lifetime test system (Guangzhou Jinghe Equipment Co., Ltd), UV lamp, UV light cleaning machine (BZS250GF-TC, HWOTECH), ultrasonic cleaning machine (KQ5200E, Kunsan Shumei), electronic balance (PX125DZH, OHAUS), glove box (2440/750/900, MIKROUNA), evaporation (FANGSHENG, OMV-FS300), vacuum drying oven, electrothermal blowing dry box (OVEN 125 basic dry), spin-coater (EZ6/AC200-SE), luminance meter (Konica Minolta LS-160), Keithley 6485 Picoammeter, Keithley 2400

source meter, Ocean Optics USB 2000+ spectrometer, silicon detector (Edmund), monochronic UV LEDs (ZF-7A, JIAPENG), fiber spectrometer, multimode fiber.

The classic HT method using PbX_2 salts for LHP NCs synthesis is described here, including preparing various precursors.

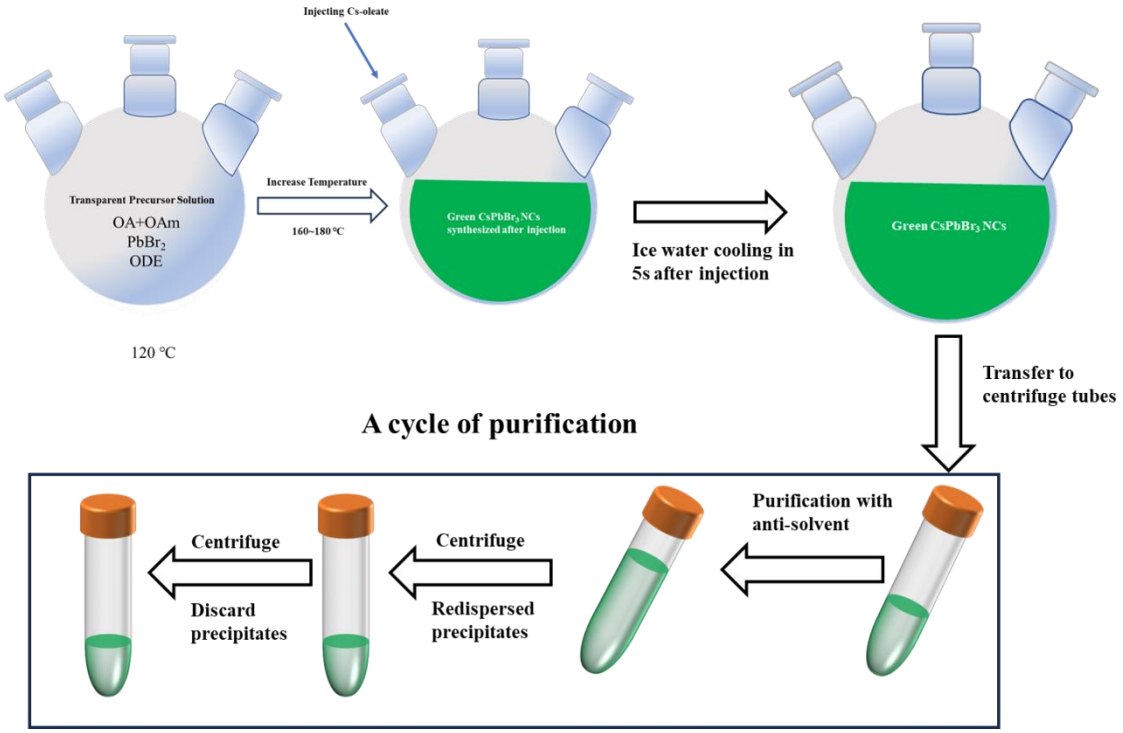

Figure 2.2 | Schematic illustration of classic HT method for $CsPbBr_3$ NCs and corresponding purification process.

Preparation of Cs-oleate. Cs-oleate preparation is modified from Kovalenko's report(Protesescu et al., 2015). Precisely, 0.75 mmol (244.36 mg) caesium carbonate (Cs_2CO_3) was weighed by the balance and placed in a three-necked round bottom flask. Then, 9 ml 1-octadecene (ODE) and 1 ml OA were added into the flask with a stir bar. Injection syringes were used for adding liquids. A magnetic stirrer was used to stir continuously. The mixture solution was heated to 40 ℃ and vacuum dried for 30 mins with the established Schrenk Line. Then, the temperature was increased to 100 ℃ and continuously vacuumed, drying for 60 mins. Then, the vacuum drying process was stopped, and the flask was filled with argon. The argon was used to bubble the mixture

solution to further degassing oxygen and water for 30 mins. The transparent Cs-oleate solution was obtained after completely removing oxygen and water. The flask was encapsulated with a rubber stopper and cooled to room temperature before use. The Cs-oleate precipitates from ODE at room temperature and is usually heated to 100 ℃ before usage.

OA/OAm $CsPbBr_3$ NCs synthesis. Kovalenko reported the synthesis of OA/OAm CsPbBr3 NCs in 2015. Figure 2.2 shows the procedures for LHP NC synthesis. Here, some parameters are different from his report. Specifically, 0.376 mmol (138 mg) $PbBr_2$ with 10 mL ODE in the three-neck bottom flask was vacuum dried at 40 ℃ for 30 mins. An electronic balance was used to weigh $PbBr_2$ powders, while injection syringes were used to add ODE. Then, the temperature was increased to 100 ℃ and continued vacuum drying for 60 mins. After stopping the vacuum dying, the argon flow was pumped into the flask, and the lead halide precursor was protected from oxygen and water. 1 mL OA and 1 mL OAm were injected into the mixtures to dissolve the $PbBr_2$. The mixture solution was keeping bubbled by argon. After the $PbBr_2$ was wholly dissolved and formed a clear solution, the temperature was increased to 160 ℃. 0.8 ml transparent Cs-oleate precursor solution was quickly injected into the flask at 160 ℃. After 5 seconds, the flask was swiftly cooled by an ice water bath. The crude solution was transferred into two 50 mL centrifuge tubes. There is about 6 mL of crude solution in each centrifuge tube. Then, methyl acetate 12 mL was added to each centrifuge tube, and the volume ratio of antisolvent to the crude solution was about 2:1. The mixture was centrifuged at 8000 revolutions per minute (rpm) for 3 minutes. Discard the liquid supernatant and redispersed precipitate with toluene (2 mL for each centrifuge tube). Oscillate the redispersed LHP NC solution for 30 seconds on the oscillator. The redispersed LHP NC solution was centrifuged at 10000 rpm for 60 seconds. An injection syringe extracts the NC solution, and the undispersed precipitates are discarded. Filter the solution into a centrifuge tube with a nylon organic solvent filter (0.22 μm). 4 mL of LHP NCs dispersed in toluene was gained. Repeat the purification procedure one more time. Ethyl acetate

was used for purification for the second time. The volume ratio of anti-solvent to LHP NC solution is 3:1. Specifically, 12 mL ethyl acetate is added to precipitate the NCs. 1.5 to 2 mL octane was used for redispersing LHP NCs. The obtained LHP NC solution was filtered into a 5 mL vial and stored in the refrigerator at 4 ℃ before usage.

DEHPA/OAm $CsPbBr_3$ NCs synthesis. The synthesis of Bis(2-ethylhexyl) phosphate (DEHPA) $CsPbBr_3$ NCs was modified from the OA/OAm nanocrystal synthesis described above. The OA used in OA/OAm LHP NC synthesis was replaced with DEHPA. 0.9 mL DEHPA and 1 mL OAm were injected into the flask to dissolve $PbBr_2$. All the other steps are the same.

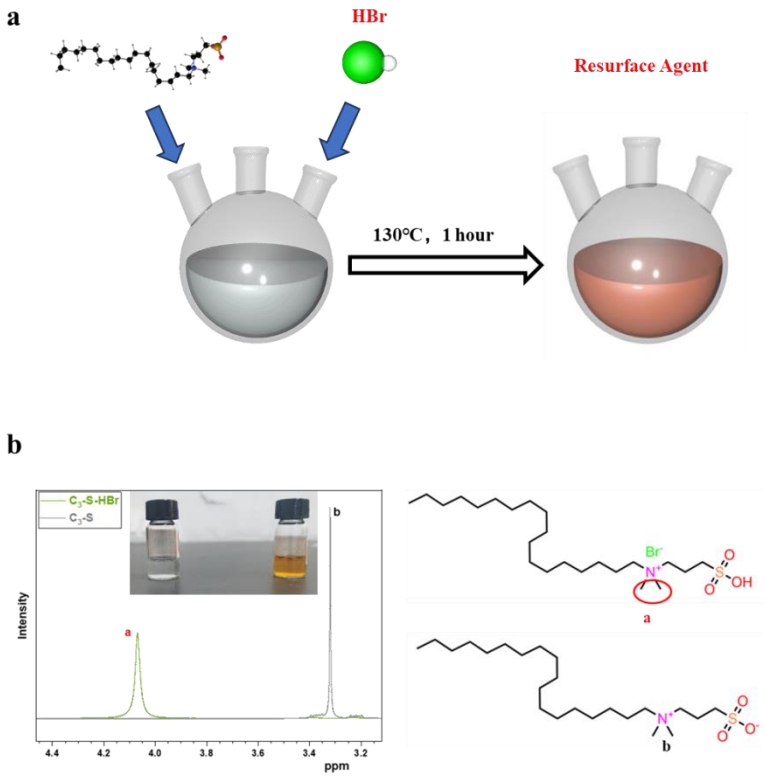

Figure 2.3 | Synthesis of resurface agent, (a) schematic illustration of C_3-S-HBr synthesis, (b) 1H NMR characterisation of C_3-S and C_3-S-HBr.

Resurface agent C_3-S-HBr synthesis. Reactions between hydrobromide acid and C_3-S synthesised the resurfacing agent C_3-S-HBr-(N, N-dimethyloctadecylammonio) propane sulfonate (C_3-S), as exhibited in Figure 2.3a. 0.4 mmol (172 mg) C_3-S was weighted by an electronic balance and added into a 50 mL three-necked flask. Then, 4 mL of

mesitylene was added with a magnetic bar. 100 μL of HBr was injected into the mixture and degassed using argon flow for 30 minutes at room temperature. The temperature was elevated to 130 ℃ in the argon atmosphere, and C_3-S was utterly dissolved in the mesitylene to form a colourless transparent solution. The C_3-S and HBr continually reacted at 130 ℃ for 60 minutes. The colourless transparent solution gradually turned to rufous after reacting at 130 ℃ for 1 hour. The reaction produced bromide salt. The temperature of the C_3-S-HBr solution was kept at 130 ℃ before usage.

The raw material C_3-S may be a kind of dimer. The peak of 3.32 ppm is attributed to methyl near the ammonium group. After reacting with hydrobromic acid, the dimer structure is broken; the possible product molecular structure is shown in Figure 2.3b. Due to changes in the chemical environment, the peak of methyl groups shifts to 4.06 ppm from 3.32 ppm.

C_3-S-HBr passivated OA/OAm $CsPbBr_3$ NCs. The synthesis of OA/OAm $CsPbBr_3$ nanocrystals treated with C_3-S-HBr was modified from the OA/OAm LHP NC synthesis mentioned above. After the injection of Cs-oleate, the prepared 2 mL C_3-S-HBr resurface agent was directly injected into the three-neck flask. After 3 seconds, 0.3 mmol didodecylamine (DDDAm) dissolved in 1 mL toluene was injected into the flask, and the mixture was immediately cooled to room temperature by an ice water bath. All the other steps are the same.

C_3-S-HBr passivated DEHPA $CsPbBr_3$ NCs. The DEHPA $CsPbBr_3$ nanocrystals treated with C_3-S-HBr were synthesised using the DEHPA LHP NCs method illustrated above. After the injection of Cs-oleate, the prepared 2 mL C_3-S-HBr resurface agent was directly injected into the three-neck flask. After 3 seconds, 0.3 mmol didodecylamine (DDDAm) dissolved in 1 mL toluene was injected into the flask, and the solution was immediately cooled to room temperature by an ice water bath. Different ligands, such as PEA, DOAm, and 4-PEA, are injected to obtain different ligands-capped LHP NCs, just like the injection of DDDAm. All the other procedures are the same.

C_3-S-HBr passivated $CsPbBr_3$ NCs. The synthesis of OTAc/OTAm $CsPbBr_3$ nanocrystals was modified from the C_3-S-HBr treated DEHPA $CsPbBr_3$ nanocrystals. The precursor ligands for dissolving the $PbBr_2$ are OA/OAm plus OTAc/OTAm. The molar ratio of OA/OAm to OTAc/OTAm is 3:8. Different molar ratios were tried, such as 2:1 and 2:3. For example, if the molar ratio is 3:8, 0.3 mL OA, 0.3 mL OAm, 0.4 mL OTAc and 0.4 mL OTAm was added into the flask to dissolve $PbBr_2$. In addition, in the second time of purification, 100 μL of 0.25 mmol·mL^{-1} OPA toluene solution was added into 4 mL LHP NC solution to do ligand exchange. The anti-solvent was added after oscillating the LHP NC solution for 30 seconds. All the other procedures are the same.

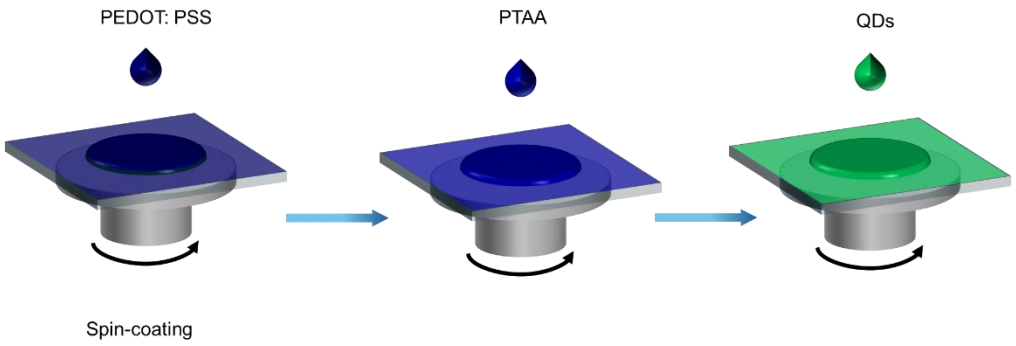

Figure 2.4 | Schematic illustration of the spin-coating process.

Device Fabrication. Acetone, isopropanol, and ethanol were sequentially used to clean the ITO pattern glass substrate with an ultrasonic cleaner. Each time took 15 minutes for ultrasonic. Then, it was treated with ultraviolet ozone to modify the work function of ITO, which usually took 15 minutes. The spin-coating process of films is manifested in Figure 2.4 PEDOT: PSS (aqueous solution) was spin-coated at 2000 rpm for 40 seconds. Then, it was annealed at 150 ℃ for 30 minutes. Subsequently, it was transferred to the glove box. In the glove box, PTAA (8 mg·mL^{-1}, chlorobenzene solution) was spin-coated on the PEDOT: PSS layer and annealed for 15 minutes at 120 ℃. The synthesised perovskite nanocrystals (25 mg·mL^{-1}, octane solution) were spin-coated at 2000 rpm for 30 seconds. It was then annealed at 60 ℃ for 10 minutes. After annealing, 5 nm TPBi, 35 nm PO-T2T,

1 nm LiF, and 100 nm Al electrodes were evaporated under 2×10^{-4} Pa pressure. For device structure with PMMA as an interface layer, the PMMA (3 mg·mL^{-1}) was spin-coated on PTAA film at 5000 rpm for 30 seconds and then annealed at 120 ℃ for 10 minutes.

2.2 $CsPbI_3$ QD synthesis and device fabrication

The synthesis method for small-size pure red $CsPbI_3$ QDs uses ZnI_2 as an extra halide source to control the particle size. My methods are modified from previous reports. The evolution of the methods is illustrated in Figure 2.5. The synthesis method in this section is employed in Chapter 4 for $CsPbI_3$ QDs.

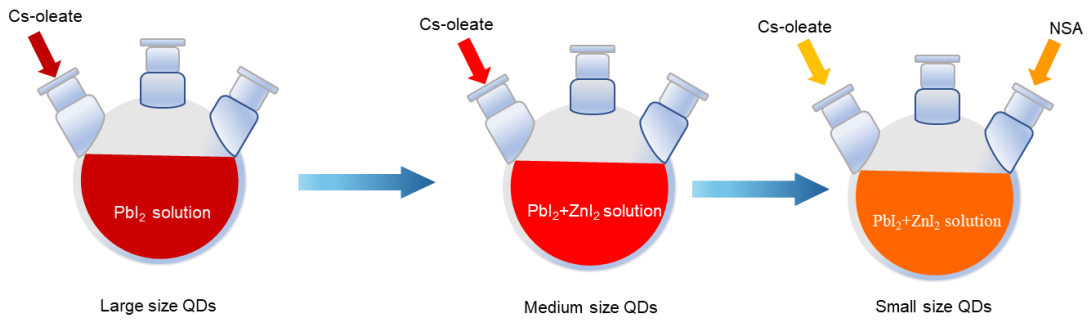

Figure 2.5 | Schematic illustration of the evolution of the HT method for small-size $CsPbI_3$ synthesis.

Materials: Cesium carbonate (Cs_2CO_3, Sigma-Aldrich 99.995%), oleic acid (OA, Sigma-Aldrich 90%), oleylamine (OAm, Aladdin 90%), octylphosphonic acid (OPA, Aladdin, 97%), lead (II) bromide ($PbBr_2$ Aladdin 99.999%), zinc bromide ($ZnBr_2$, Aladdin, 99.999%), zinc iodide (ZnI_2, Aladdin, 99.999%), lead iodide (PbI_2, Macklin, 99.999%), 1-octadecene (ODE, Sigma-Aldrich 90%), hydrogen bromide (HBr, alfa), hydroiodic acid (HI, Aladdin, 55.0% to 58.0%), hexane (Aladdin 99%), methyl acetate (MeOAc, Aladdin anhydrous 99.5%), ethyl acetate (Aladdin anhydrous 99.5%), 3-(N,N-dimethyloctadecylammonio) propanesulfonate (Aladdin, 99.8%, abbreviation C_3-S or ASC18), 5-aminovaleric acid (5AVA, Aladdin, 97%), octane (Aladdin 99%), chlorobenzene (CB, Mackin, 99.8%), 2-naphthalenesulfonic acid (NSA, SCRC, 98%),

ammonium hexafluorophosphate (NH_4PF_6, Sigma-Aldrich, 99.999%), poly(3,4-ethylenedioxythiophene) polystyrene sulfonate (PEDOT: PSS, 4083, Xi'an Polymer Light Technology Corp.), poly[bis(4-phenyl)(2,4,6-trimethylphenyl)amine](PTAA, Lingzhi Technology Co., Ltd.), 3,3'-[5'-[3-(3-pyridinyl)phenyl][1,1':3',1"-terphenyl]-3,3"-diyl]bispyridine (TmPyPB, Xi'an Polymer Light Technology Corp.), (2,4,6-tris(3-(diphenylphosphoryl)phenyl)-1,3,5-triazine (PO-T2T, 99.5%), Lithium fluoride (LiF) are from Xi'an Polymer Light Technology. Argon, Indium tin oxide (ITO) glass, UV epoxy resin (Nagase, XNR5516Z(C)-SA1), capping glass, nylon organic solvent filter (0.22 μm).

Equipment: Equipment for $CsPbI_3$ QD synthesis is the same as $CsPbBr_3$ QD synthesis.

Preparation of Cs-oleate. Cs-oleate preparation is modified from Kovalenko's report(Protesescu et al., 2015). Precisely, 0.43 mmol (142 mg) caesium carbonate (Cs_2CO_3) was weighed by the balance and placed in a three-necked round bottom flask. Then, 11 mL 1-octadecene (ODE) and 0.6 ml OA were added into the flask with a stir bar. Injection syringes were used for adding liquids. A magnetic stirrer was used to stir continuously. The mixture solution was heated to 40 ℃ and vacuum-dried for 30 minutes with the established Schrenk Line. Then, the temperature was increased to 100 ℃ and continuously vacuumed, drying for 60 minutes. Then, the vacuum drying process was stopped, and the flask was filled with argon. The argon was used to bubble the mixture solution further to degass oxygen and water for 30 minutes. The transparent Cs-oleate solution was obtained after completely removing oxygen and water. The flask was encapsulated with a rubber stopper and cooled to room temperature before use. The Cs-oleate precipitates from ODE at room temperature and is usually heated to 100 ℃ before usage.

Synthesis of OA/OAm $CsPbI_3$ NCs. The synthesis of OA/OAm $CsPbI_3$ NCs was reported by Son in 2018. Here, some parameters are different from his report. Specifically, 0.401 mmol (185 mg) PbI_2 and 1.10 mmol (351 mg) with 6 mL ODE in the three-neck bottom flask were dried in argon flow at room temperature for 30 minutes. An electronic balance was used to weigh PbI_2 powders, while injection syringes were used to add ODE.

Then, the temperature was increased to 120 ℃ and continued to flow argon to dry for 60 minutes. After stopping dying, 1.2 mL OA and 2 mL OAm were injected into the mixtures to dissolve the PbI_2. The mixture solution was keeping bubbled by argon. After the PbI_2 was wholly dissolved and formed a clear solution, the temperature was increased to 150 ℃. 2.4 mL transparent Cs-oleate precursor solution was quickly injected into the flask at 150 ℃. After 5 seconds, the flask was swiftly cooled to 50 ℃ by an ice water bath. The crude solution was transferred into two 50 mL centrifuge tubes. There is about 4 mL of crude solution in each centrifuge tube. They were centrifuged at 4000 rpm for 1 minute to remove unreacted precursor salts. The transparent upper solution was transferred to another two clean centrifuge tubes. Then, add ethyl acetate 10 mL and methyl acetate 22 mL into each centrifuge tube. The mixture was centrifuged at 7000 rpm for 2 minutes. Discard the liquid supernatant and redispersed precipitate with hexane (0.7 mL for each centrifuge tube). Oscillate the redispersed LHP NC solution for 30 seconds on the oscillator. The redispersed LHP NC solution was centrifuged at 4000 rpm for 60 seconds. An injection syringe extracts the NC solution, and the undispersed precipitates are discarded. Filter the solution into a centrifuge tube with a nylon organic solvent filter (0.22 μm). 1.4 mL of LHP NCs dispersed in hexane was gained. Then, I purified the NC solution one more time. Ethyl acetate 6 mL and methyl acetate 6 mL were added for second-time purification. The mixture was centrifuged at 7000 rpm for 1 minute. 1 mL octane is used for the redispersion of LHP NCs. The obtained LHP NC solution was filtered into a 5 mL vial and stored in the refrigerator at 4 ℃ before usage.

Preparation of 5AVAI ligand solution. 0.1, 0.2, and 0.3 mmol (M) 5AVA were dissolved with 19 μL, 38 μL, and 57 μL HI, respectively. 1 mL ethyl acetate was added as a solvent to prepare the 5AVAI solution. The 5 AVAI solution formed was white turbidity. The 5AVAI solution was heated to 80 ℃ for subsequent ligand treatment.

Preparation of NSA ligand solution. 0.2, 0.4, 0.6, and 0.8 mmol NSA ligands were dissolved in 1 mL of ethyl acetate solvent. The formed transparent solution was heated and stirred at 80 ℃ for 20 minutes before subsequent ligand treatment.

Preparation of NH_4PF_6 ligand solution. 0.2 mmol NH_4PF_6 was dissolved in 1 mL methyl acetate solvent for subsequent ligand exchange. To accelerate the dissolution, the mixture was heated and vibrated.

Synthesis of NSA-NH_4PF_6 $CsPbI_3$ NCs. The synthesis of NSA-NH_4PF_6 $CsPbI_3$ nanocrystals was modified from the OA/OAm nanocrystal synthesis described above. After injecting 2.4 mL Cs-oleate to react for 5 seconds, the mixture solution was cooled to 130 ℃ by ice water bath; the NSA ligands were injected to control nanocrystal growth at 130 ℃. When temperatures of the mixture solution were cooled to 50 ℃, the crude solution was transferred into two 50 mL centrifuge tubes. The procedures of first-time purification are the same as OA/OAm $CsPbI_3$ NCs. The second-time purification was different and described here. Methyl acetate 0.5 mL and ethyl acetate 6 mL, 140 μL NH_4PF_6 solution were sequentially added into 1.4 mL QDs solution for second-time purification. The mixture was centrifuged at 5000 rpm for 1 minute. Discard the residue and add 6 mL methyl acetate to the upper transparent solution. Then, the mixture was centrifuged at 7000 rpm for 1 minute. 1 mL octane is used for the redispersion of LHP NCs. The NC solution was centrifuged at 4000 rpm for 1 minute to remove undispersed precipitate. The obtained LHP NC solution was filtered into a 5 mL vial and stored in the refrigerator at 4 ℃ before usage.

Synthesis of 5AVAI $CsPbI_3$ NCs. The parameters for synthesising 5AVAI $CsPbI_3$ NCs differ slightly from synthesising OA/OAm $CsPbI_3$ NCs. Specifically, 185 mg PbI_2, 351 mg ZnI_2, and 6 mL ODE were loaded into a 50 mL three-necked flask and dried under argon flow at 120 °C for one h. Then, 1 mL OA and 2 mL OAm were injected at 120 °C under argon flow. The temperature was increased to 150 °C, and Cs-oleate (2.2 mL of the stock solution prepared as described in this section) was swiftly injected and reacted for 5 seconds. Then, the reaction mixture was immediately cooled to 100 °C by immersing in a cold water bath; the prepared 5AVAI ligand solution was swiftly injected. Subsequently, the reaction mixture was cooled down to 55 °C. The crude solution needs

to be purified as soon as possible. It was centrifuged at 5000 rpm for 1 min to remove unreacted salts and transferred to two 50 mL centrifuge tubes. Then, add ethyl acetate 10 mL and methyl acetate 22 mL into each centrifuge tube. The mixture was centrifuged at 7000 rpm for 2 minutes. The obtained precipitates containing $CsPbI_3$ QDs were re-dispersed in 1 mL of hexane and centrifuged at 5000 rpm for 1 min to remove non-perovskite precipitates. The preliminary purified QDs solution of 1 mL was added to 6 mL methyl acetate and 6 mL ethyl acetate to precipitate again and centrifuged at 4000 rpm for 5 min. The obtained $CsPbI_3$ QDs were redispersed in 1 mL of octane and centrifuged at 5000 rpm for 1 min. Finally, the QDs solution was filtered by a 0.22 μm poly(tetrafluoroethylene) filter.

Device Fabrication: The ITO glass cleaning process is the same as described in the previous section. PEDOT: PSS (aqueous solution) was spin-coated at 6000 rpm for the 40 seconds. Then, it was annealed at 150 ℃ for 20 minutes. Subsequently, it was transferred to the glove box. In the glove box, PTAA (8 $mg \cdot mL^{-1}$, chlorobenzene solution) was spin-coated on the PEDOT: PSS layer and annealed for 15 minutes at 120 ℃. The synthesised perovskite NCs (10 mg mL^{-1}, octane solution) were spin-coated at 2000 rpm for 30 s. It was then annealed at 60 ℃ for 10min. After annealing, 5 nm Tmpypz, 35 nm PO-T2T, 1 nm LiF, and 100 nm Al electrodes were evaporated under 2×10^{-4} Pa pressure.

2.3 Characterizations

Ultraviolet-visible light (UV-vis) absorption spectra. The UV-vis absorption spectra were obtained by Perkin-Elmer Lambda 950. The sample was diluted by hexane before characterisation, and the absorbance is usually around 0.05 at the wavelength of the excitation source—the UV-vis characterised materials' absorption spectra, including films and solutions. UV-vis is employed for characterising $CsPbBr_3$ and $CsPbI_3$ QDs in Chapters 3, 4, and 5.

TEM and high-resolution transmission electron microscope (HRTEM). TEM and HRTEM of nanocrystals were obtained by a Talos F200X with 200 kV acceleration

voltage. The sample used for TEM characterisation was usually diluted with hexane or octane to a concentration of 3 mg $\cdot mL^{-1}$. TEM characterised QDs' shape, morphology and uniformity. The characterisation is used for $CsPbBr_3$ and $CsPbI_3$ QDs in Chapters 3 and 4.

PL spectra. PL spectra profiles were obtained by using the Horiba FL3-111. The excitation source is 400 nm or 420 nm. The sample used for PL characterisation must be diluted, and the measured intensity must be under 2000000 with the CPS model. If the measured PL intensity exceeds 2000000, the reabsorption of samples induces measured spectra redshift and widens the full width of half maximum (FWHM). PL spectra are employed for characterising $CsPbBr_3$ and $CsPbI_3$ QDs in Chapters 3, 4, and 5.

Time-resolved PL decay spectra (TRPL). TRPL of NCs were also obtained by applying the Horiba FL3-111. The samples for TRPL were fabricated by spin-coating with LHP NC solution, the concentration of which is from 15 to 25 mg mL^{-1}. The LHP NCs were dispersed in octane. The LHP NCs solution was spin-coated on ITO glass at 2000 rpm for 30 seconds to form thin films. The emission wavelength of the laser excitation source for TRPL characterisation is 320 nm. TRPL spectra are employed for characterising $CsPbBr_3$ and $CsPbI_3$ QDs in Chapters 3, 4, and 5.

PLQY. PLQY was obtained by using the Otsuka QE2100. The samples were diluted with hexane. The absorbance of measured samples is in the range of 0.1 to 0.6. PLQY are employed for characterising $CsPbBr_3$ and $CsPbI_3$ QDs in Chapters 3, 4, and 5.

XRD spectra. The XRD spectra of nanocrystal film were obtained by a Bruker D8 Advanced Davinci using Cu Kα radiation (λ=1.5418 Å). The samples for XRD characterisation were prepared by directly casting LHP NC solution on ITO glass or glass substrates to form a relatively thicker film. XRD are employed for characterising $CsPbBr_3$ and $CsPbI_3$ QDs in Chapters 3, 4, and 5.

Fourier transform infrared spectroscopy (FTIR). FTIR was collected using a Cary660+620 attenuated total reflectance FTIR system. All LHP NC film samples were

fabricated by directly casting on glass substrates to form a micrometre-thick film. XRD are employed for characterising $CsPbBr_3$ and $CsPbI_3$ QD films in Chapters 3, 4, and 5.

X-ray photoelectron spectroscopy (XPS). XPS measurements were performed using an ESCALAB 250Xi with a base pressure of 10^{-9} torr. The X-ray radiation is Al Kα emission (1486.7 eV, take-off angle, 75°). The calibration was implemented with gold as standard samples. The ultraviolet photoelectron spectroscopy (UPS) measurement was also performed employing the ESCALAB 250Xi with a base pressure of 10^{-9} torr. The standard sample used for calibration is gold. XPS are employed for characterising $CsPbBr_3$ and $CsPbI_3$ QD films in Chapters 3, 4, and 5.

Photostability. Photostability tests were implemented here, and UV lamps were used as excitation sources. The intensity of the UV lamps is 320 $mW \cdot cm^{-2}$ and 500 $mW \cdot cm^{-2}$. The excitation source wavelength is 365 nm or 254 nm. The LHP NC films were fabricated by spin-coating at 2000 rpm with a 40 $mg \cdot mL^{-1}$ concentration. The solvent is hexane. Photostability tests are employed for characterising $CsPbBr_3$ and $CsPbI_3$ QDs in Chapters 3, 4, and 5.

In-situ photoluminescence (PL) spectra. Screening of perovskite QD precursors can be implemented by characterising perovskite QD evolution in the synthesis process. The setup of the in-situ PL system for characterising nucleation and growth is illustrated in Figure 2.6. As shown here, the initial nucleation size of the nanocrystal can be indirectly characterised by the in-situ PL system. In addition, it is also reasonable to use an in-situ photoluminescence system to investigate the nucleation and growth of the perovskite nanocrystal synthesis process. The particle size and composition determine the emission wavelength and FWHM of LHP NCs(M. Zhang et al., 2023). Therefore, perovskite nanocrystals' nucleation and growth kinetics can be deduced by analysing the emission wavelength and FWHM data collected by the in-situ photoluminescence system.(Lignos et al., 2018, 2016) In-situ PL spectra were performed by a monochromatic source (LED), which was used as an excitation source (emission wavelength 365 nm). The emission

originating from the sample coupled via a 10× objective to a fibre spectrometer through a 2 m long multimode fibre with a core diameter of 400 µm. The spectrometer comprised a 20 µm entrance slit, 600 lines per millimetre (mm) grating, and a detector containing 2048 pixels. The spectrometer was operated between 400 and 1100 nm, and data was recorded using 10 to 100 milliseconds (ms) integration times. The entire system was enclosed in a black box to minimise pollution from the stray light. In-situ PL spectra are employed for characterising $CsPbBr_3$ and $CsPbI_3$ QDs in Chapters 3 and 4.

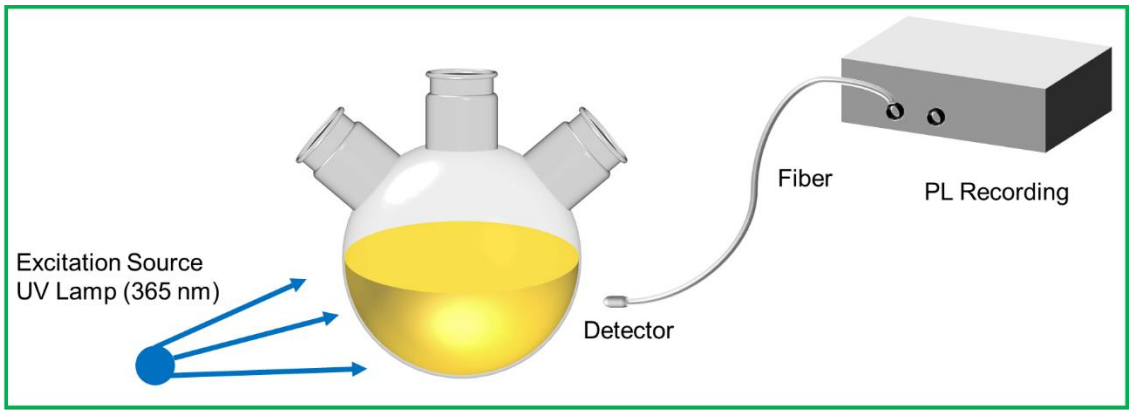

Figure 2.6 | Schematic illustration of in-situ PL measurements.

Device characterisation. The relation between external quantum efficiency (EQE) and internal quantum efficiency (IQE) of emitting materials can be described by the following equation:

$$\eta_{EL} = \eta_{rec}\eta_s\eta_{PL}\eta_{OUT} \tag{2.1}$$

η_{EL} is electroluminescence efficiency: EQE, η_{rec} is the charge balance factor of the devices, η_s is the spin statistic factor, η_{PL} is the photoluminescence efficiency of emitting materials, η_{OUT} is the light outcoupling efficiency. PeQDs are inorganic semiconductor materials with direct bandgap. Therefore, η_s is unity in the thesis. The charge balance factor depends on the device's charge balance. η_{OUT} depends on many factors, such as device structure, refractive index, dielectric constant, and absorptivity of each layer.

The EL performance of devices was measured with the same setup as previously reported (Xiang et al., 2020). Electroluminescence spectra were obtained using an Ocean Optics USB 2000+ spectrometer with the devices driven at a constant current with a Keithley 2400 source meter. The *J-L-V* characteristics of the devices were taken under ambient conditions with a Keithley 2400 source meter measuring the sweeping voltages and currents and a Keithley 6485 Picoammeter with a calibrated silicon detector (Edmund) measuring light intensities. Luminance was calibrated using a luminance meter (Konica Minolta LS-160) with the assumption of the Lambertian emission pattern of all devices. This measurement is employed for characterising PeQLEDs in chapters 3, 4, and 5.

The operational lifetime test was conducted under ambient conditions at room temperature (22±2℃) using a commercialised lifetime test system (Guangzhou Jinghe Equipment Co., Ltd). The devices were encapsulated with Nagase UV epoxy resin XNR5516Z(C)-SA1 and capping glasses. A UV lamp was used to solidify the epoxy resin for 30 minutes. The operation lifetime test is employed for characterising PeQLEDs in Chapters 3, 4, and 5.

Defects density and hole mobility calculation

The defect density of thin films could be calculated by trap-filled limit region (V_{TFL}) as shown in equation 2.2. The Mott-Gurney law equation can calculate the hole mobility of perovskite nanocrystal films 2.3.

$$N_t = \frac{2\varepsilon\varepsilon_0 V_{TFL}}{ed^2} \tag{2.2}$$

$$J_D = \frac{9\varepsilon\varepsilon_0 \mu V^2}{8d^3} \tag{2.3}$$

The structure of our hole-only devices is ITO/PEDOT: PSS (30 nm)/PTAA (35 nm)/PMMA/QDs (~240 nm) /TAPC (10 nm)/Ag. N_t is the trap state density, V_{TFL} is the trap-filled limit voltage, d is the distance between the electrodes, e is the elementary charge, ε_0 and ε is the vacuum permittivity and relative permittivity, respectively. μ is carrier mobility which is hole mobility here. J_D and V are current density and bias in the

Child's Law region. However, it is hard to spin-coat pure red $CsPbI_3$ QD film with a thickness of 240 nm. Therefore, the active layer thickness of the hole-only device for $CsPbI_3$ QDs was only 10 nm. Consequently, the measured data for those devices cannot be used for calculation, but it can be used for contrast. This measurement characterises PeQLEDs in Chapters 3, 4, and 5.

Density Functional Theory (DFT) Calculations. The binding energies between different ligands and $CsPbI_3$ are calculated using density functional theory (DFT) in the Vienna ab initio Simulation Package (VASP) (Kresse and Furthmüller, 1996; Kresse and Hafner, 1993) with projector augmented waves (PAW) pseudopotentials(Blöchl, 1994; Joubert, 1999). The generalised gradient approximation (GGA) is chosen to approximate the exchange-correlation energy with the Perdew–Burke–Ernzerhoff (PBE) functional(Itaya et al., 1986). A cutoff energy of 500 eV and an 8 × 8 × 1 Monkhorst–Pack k-point mesh were used for all the calculations(Pack and Monkhorst, 1977). The convergence threshold for each ionic step is set to be 1×10^{-6} eV, and the convergence threshold of maximum force is set to be 0.025 eV $Å^{-1}$. Spin polarisation is also included in our calculations. All the calculations are based on the Ferromagnetic (FM) configuration. The high-resolution TEM image of QDs manifested in Figure 2.7a demonstrates that the exposed crystal surface is (100). Therefore, the (100) surfaces are chosen to simulate the binding process. Both ion positions and cell shape can change during the structural relaxation. Figure 2.7b is the measured XRD spectra of synthesised $CsPbI_3$ QDs. The configurations of ligand-$CsPbI_3$ binding are shown in Figure 2.8. After structural relaxation, the binding energy is calculated by the equation:

$$E_b = E_{ligand-CsPbI_3} - E_{ligand} - E_{CsPbI_3} \quad (2.4)$$

This simulation is used in Chapter 4 for $CsPbI_3$ QDs.

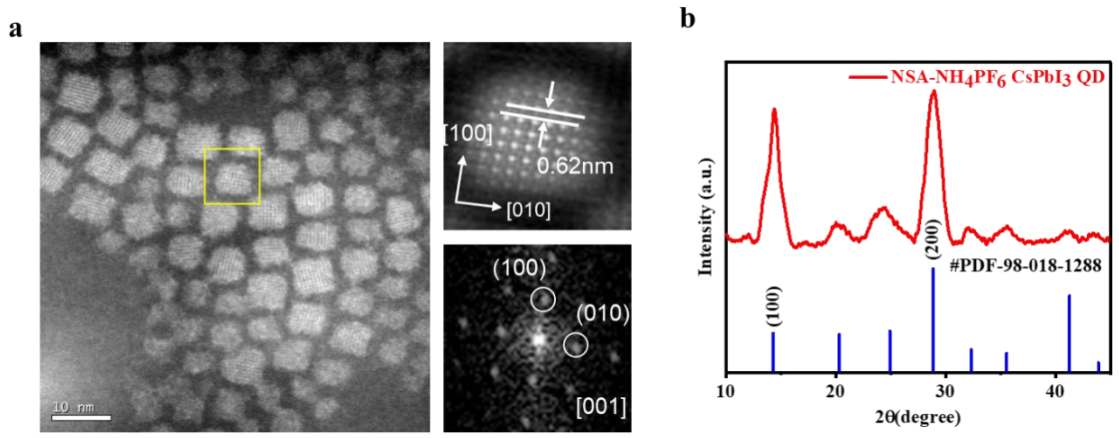

Figure 2.7 | (a) TEM image of synthesised NSA-treated $CsPbI_3$ QDs (b) XRD spectra of synthesised $CsPbI_3$ QDs.

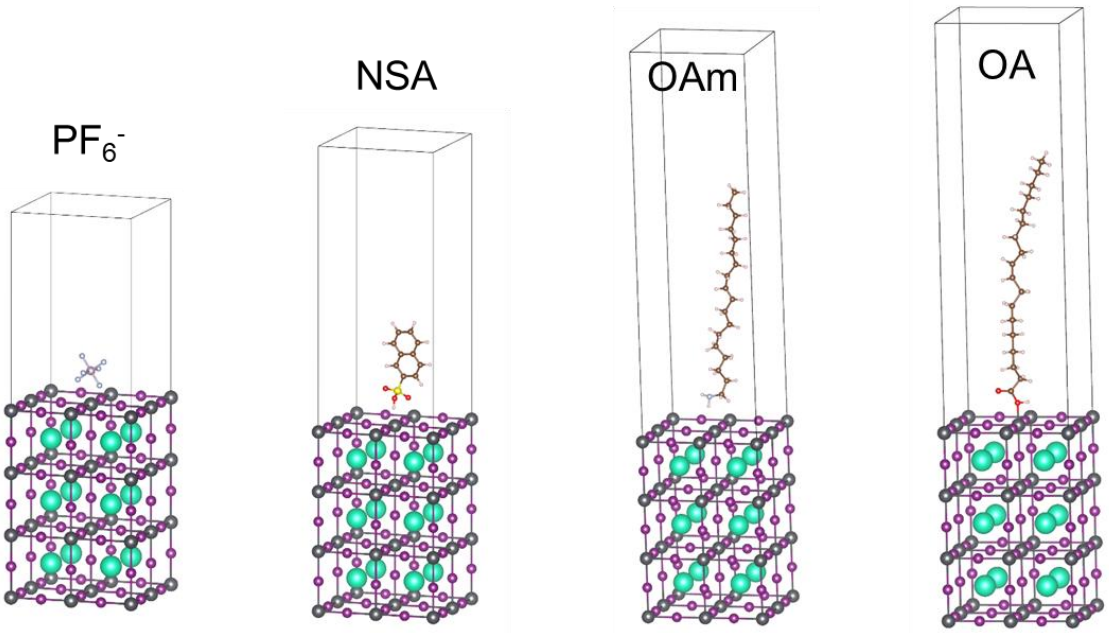

Figure 2.8 | Different ligands-$CsPbI_3$ Binding. Configurations of various ligand-$CsPbI_3$ binding, including PF_6 anions, 2-naphthalene sulfonic acid (NSA), oleic acid (OA), oleylamine (OAm).

Chapter 3. Stable Green $CsPbBr_3$ Quantum Dots and Electroluminescence

3.1 Background

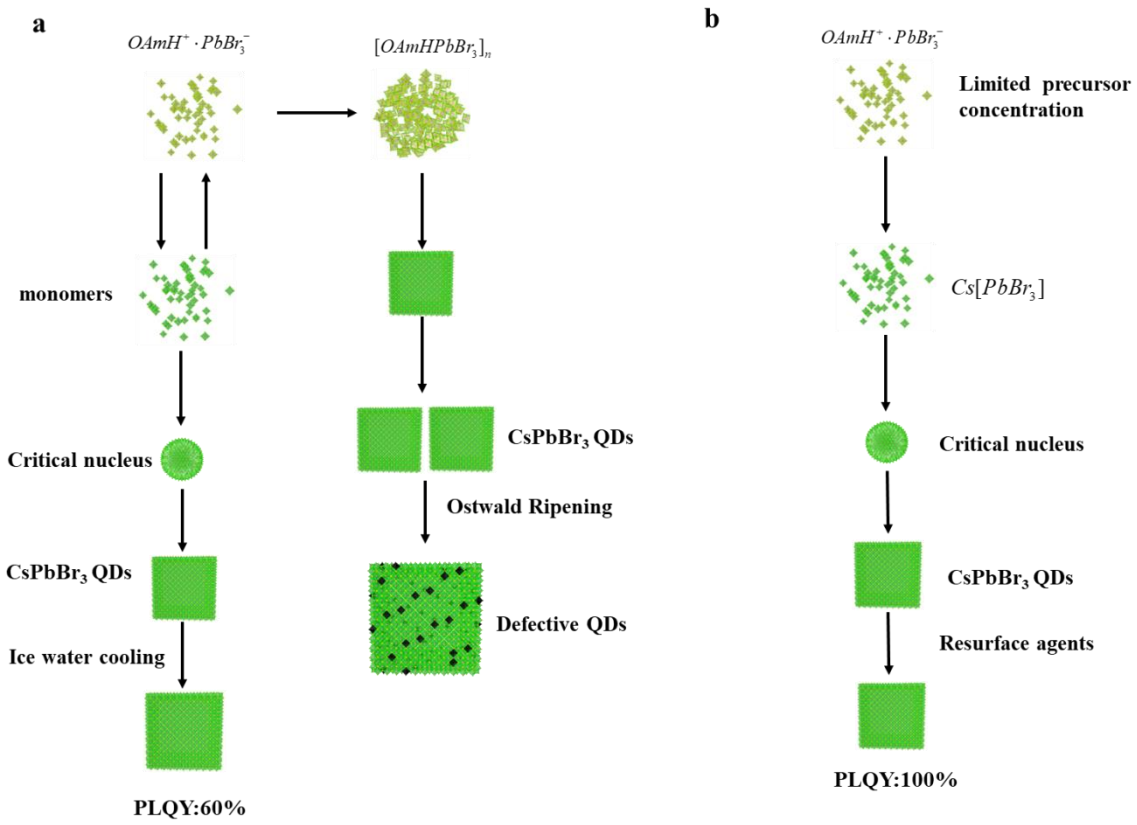

Figure 3.1 | (a) nucleation and growth of OA/OAm as precursor ligands (b) one route nucleation of DEHPA/OAm as precursor ligands.

From the perspective of LEDs, it is also vital to ensure good charge transport ability and suitable energy levels. Thus, strategies introducing lots of insulating staff need improvement and should be carefully applied. In addition, the reported all solution processable QELDs structure, which uses ZnO NPs as electron transport layer (ETL), significantly improved the operation stability of QLEDs(Qian et al., 2011). PeQLEDs may also use this strategy to increase the operation lifetime of devices, as inorganic ETL

Works in Chapter 3 were published: Zhang, X., Wang, Q., Yao, Z., Deng, M., Wang, J., Qian, L., Ren, Y., Yan, Y., Xiang, C., 2023. Adv. Sci. 10, 1–7. Zhang, X., Yao, Z., Deng, M., Wu, R., Wang, J., Ren, Y., Wang, C., Jia, G., Qian, L., Xiang, C., 2024. J. Mater. Chem. C.

is much more stable than small molecules of organic ETL, such as TPBi and PO-T2T. However, the S-QLED structure requires that LHP NC film possess good polar solvent resistance.

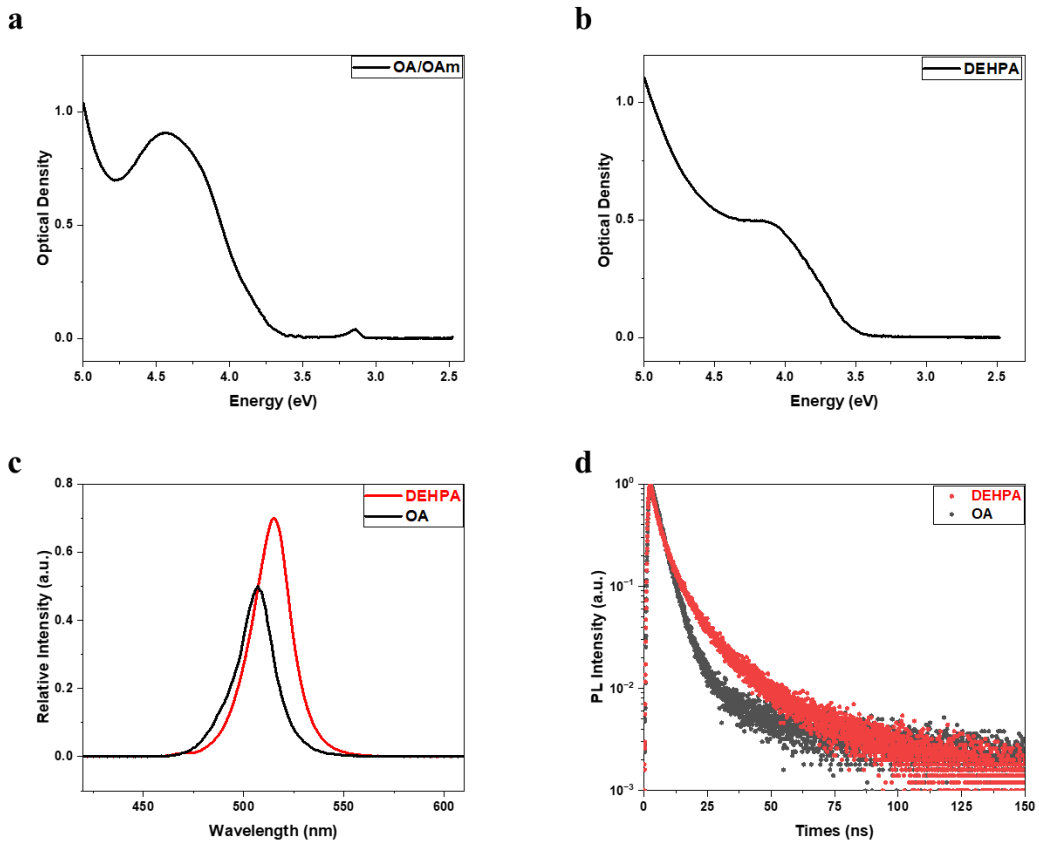

Figure 3.2 | Absorption spectra of precursor solution of (a) OA/OAm method and (b) DEHPA/OAm method. (c) PL Intensity of nanocrystal solution. (d) TRPL spectra of nanocrystal films.

A synthesis strategy is proposed to modify the classic hot injection method to synthesise stable and efficient $CsPbBr_3$ NCs. Firstly, OA/OAm ligands are replaced or partially replayed by acids or amines with a relatively higher dissociation constant, such as phosphoric and sulfonic acids. The LHP NCs synthesised with OA/OAm often suffer from nonuniform nucleation and growth as there are two routes of nanocrystal reactions in the traditional hot injection method(Almeida et al., 2018; X. Zhang et al., 2023) (Figure

3.1a). The intermediate clusters formed due to the high halo plumbate ionic solute concentration lead to large-size nanocrystals, which are over-ripening and defective(Akkerman et al., 2022). The concentration of halo plumbate ionic solute can be controlled by using high dissociation constant acids or amines (Figure 3.1b). The dissociation constant (Ka) of Bis(2-ethylhexyl) phosphate is $10^{-1.47}$, which is much higher than OA (Ka $10^{-5.02}$). Figures 3.2a and b are the absorption spectra of the precursor solution with different precursor ligands (OA/OAm and DEHPA/OAm). The small absorption peak at 3.15 eV is attributed to formed clusters. In comparison, the DEHPA/OAm method does not have a small peak at 3.15 eV. The absorption peak at 4.4 eV is attributed to dissolved $PbBr_2$ monomers. For DEHPA, the absorption peak of $PbBr_2$ monomers redshifts to 4.1 eV. As shown in Figure 3.2c, LHP NCs synthesised with DEHPA exhibit relatively high PLQY compared to OA. The measured PL intensity of DEHPA NCs is 70%, while the value of OA NCs is 50%. The TRPL measurement of nanocrystal films is manifested in Figure 3.2d. The DEHPA/OAm $CsPbBr_3$ QD films exhibit a longer exciton lifetime, indicating better surface defect passivation (Nenon et al., 2018).

Secondly, robust ligands usually used in three precursor methods are successfully applied to classic hot injection methods with an in-situ ligand exchange strategy. The novel ligand exchange agent is synthesised with zwitterionic ligands (3-(N, N-dimethyloctadecylammonio) propanesulfonate, abbreviation C_3-S) and hydrobromide acid (HBr). The resurface agent C_3-S-HBr was used to passivate the LHP NCs and replace the weak precursor ligands through in-situ ligand exchange. Compared to OA, DEHPA is a weaker ligand that can facilitate the in-situ ligand exchange process(Wang et al., 2017), as potent binding C_3-S ligands can easily replace it. The enhanced surface stability of synthesised LHP NCs can satisfy the requirements of QLED fabrication. In addition, the extra addition of Br anions is beneficial in forming a Br anions-rich surface and regulates the thermal equilibrium of reactions. Consequently, the harmful Ostwald ripening is suppressed. Finally, the LHP NCs achieve high PLQY with a Br-rich surface due to better

surface passivation. Besides DEHPA, oleic acid (OA) and oleylamine (OAm) can also be replaced by short-chain ligands octanoic acid (OTAc) and octylamine(Fang et al., 2021) (OTAm). The short-chain ligands can improve the charge transport ability of LHP NCs compared to long-chain ligands, improving the performance of QLEDs.

Amine ligands, such as DOAm, DDDAm, PEA, and F-PEA, are used together with resurfacing agent. Those amine ligands have higher surface affinity than OA. In addition, those ligands can effectively passivate surface bromide ions, immobilising the halide ions on the surface. Amine ligands also provide a suitable steric hindrance. Therefore, the surface stability of perovskite QDs has improved. In my proposal, OPA ligands are used in the purification process. The OPA ligands can further replace OA ligands. Moreover, OPA ligands can form strong hydrogen bonding on perovskite QDs surface, protecting surface bromide ions. As a result, the stability of the perovskite QDs is enhanced. (Brown et al., 2019) The synthesised OTAc/OTAm LHP NC achieved a world record EQE and operation lifetime for green PeQLEDs.

3.2 DEHPA/OAm $CsPbBr_3$ NCs with C_3-S-HBr in-situ passivation

There are usually two kinds of defects on the perovskite nanocrystal surface, as shown in Figure 3.3a Br and Cs vacancies(Bodnarchuk et al., 2019; Quarta et al., 2019). The surface composition of perovskite nanocrystals highly relies on the size of the nanocrystal. The molar ratio of surface atoms of Br: Pb: Cs is increasing with small-size nanocrystals, as shown in Figure 3.3b. Therefore, to synthesise stable perovskite quantum dots with high PLQY, passivating surface defects and constructing a stable surface is vital. Herein, the in-situ ligand exchange strategy uses C_3-S-HBr as the resurfacing agent. In addition, the OA precursor was replaced by weakly binding DEHPA ligands to facilitate the ligands exchange process. The in-situ ligands exchange strategy for the $PbBr_2$ precursor-based hot injection method employed the synthesised resurface agent to achieve efficient ligands exchange during the nanocrystal growth stage. The strategy can efficiently replace the original weak ligands of nanocrystals with robust ligands to

construct a stable surface and passivate surface defects. The in-situ ligands exchange process is manifested in Figure 3.3c. The surface defects on perovskite nanocrystals are passivated with zwitterionic ligands and Br anions injected after nucleation, which means that a resurfacing agent was injected following cesium-oleate (Cs-OA). Zwitterionic ligands replaced the original acid-weak ligands on the nanocrystal surface. In addition, perovskite nanocrystal ripening is suppressed with extra Br anions added(Dong et al., 2018). Weak-binding oleylamine ligands were replaced with latterly injected secondary amines(Bi et al., 2021). I tried different amines to exchange the oleylamine ligands, such as PEA, F-PEA, DOAm, and DDDAm. The optimised ligand is F-PEA, which exhibits the best device performance compared to other amine ligands. The details of device performance will be described in the device performance section.

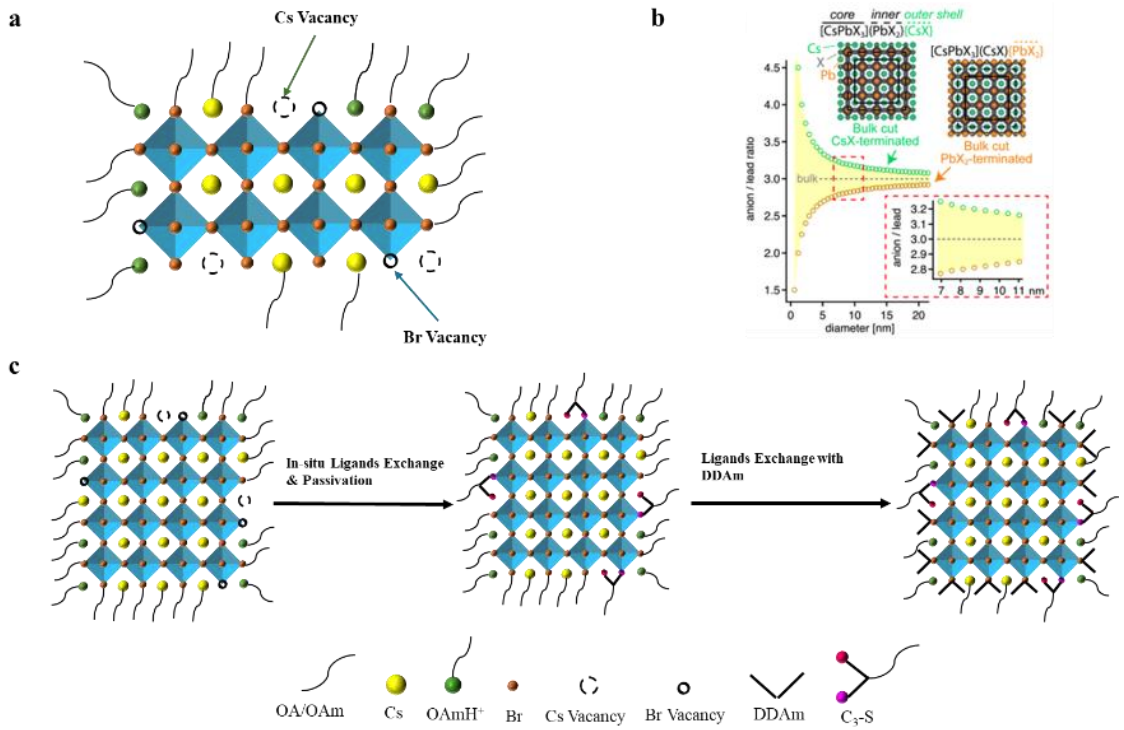

Figure 3.3 | (a) schematic diagram of 3 kinds of vacancy on the surface of PeNCs, (b) size dependence of surface atoms molar ratio of PeNCs, (c) illustration of in-situ ligands exchange and passivation of PeNCs.

The synthesis parameters, such as reaction temperature, element molar ratio, resurface agent amount, and post-treatment ligands amount, are optimised. The resurface agent amount used in the experiment is calculated by the surface ligand number of synthesised nanocrystals. The number of surface ligands is calculated according to the nanocrystals' number and surface area, as described in the methodology section. As shown in Figure 3.4a, the optimised zwitterionic ligands amount is 0.2 mmol with a PLQY of 96%. The posttreatment ligands (OPA) amount is 0.025 mmol for the first purification. For the second purification, the amount of OPA ligands is 0.019 mmol. Excess OPA ligands induce NC to decompose and broaden FWHM, as manifested in Figure 3.4b. Different amine ligands for replacing oleylamine were also tried. Compared to short chain length DOAm, nanocrystals capped with DDDAm manifested better storage stability. Excess amine ligands also cause surface octahedra to peel off. After optimising the amine amount, the emission wavelength of NC is 512 nm with an FWHM of 19 nm.

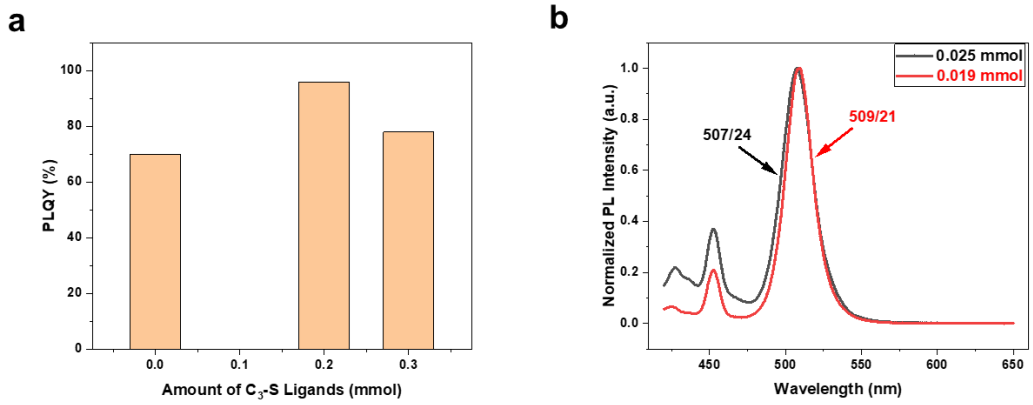

Figure 3.4 | (a) PLQY of synthesised NCs with different numbers of C3-S ligands (b) PL spectra of synthesised NCs with different numbers of OPA ligands for posttreatment.

C_3-S-HBr Passivated Nanocrystals. Studies demonstrate that the resurfacing agent C_3-S-HBr passivates various surface defects of perovskite NCs(Bodnarchuk et al., 2019; Quarta et al., 2019; J. Zhang et al., 2023; Zhao et al., 2021). To increase zwitterionic ligand density on the nanocrystal surface, a weak binding precursor ligand DEHPA is

employed to replace the oleic acid (OA) so that the in-situ ligand exchange process of zwitterionic ligands will be promoted. In addition, the DEHPA/OAm method synthesised perovskite NC exhibits better stability and higher PLQY than OA/OAm NCs. C_3-S-HBr is a strong acid with sulfonic acid groups, which can attack the defective $PbBr_6$ octahedron on the $CsPbBr_3$ surface(Bodnarchuk et al., 2019; Quarta et al., 2019). For NCs with high defect density, they are transformed into nanoplates. However, nanoplates can be removed through purification. Thus, high-quality $CsPbBr_3$ NCs are screened out after purification. This is demonstrated by the absorption spectra of as-synthesized $CsPbBr_3$ NCs treated with C_3-S-HBr. As shown in Figure 3.5a, the as-synthesized $CsPbBr_3$ nanocrystals treated with C_3-S-HBr have two sharp absorption peaks at 500 nm and 423 nm, respectively. In contrast, the controlled $CsPbBr_3$ NCs have two broad absorption peaks at 495 nm and 400 nm, respectively. The sharp absorption peak at 423 nm of treated $CsPbBr_3$ NCs can be attributed to nanoplates with 2-unit cells. After purification, the absorption peak of those unstable nanoplates disappears, as shown in Figure 3.5b. The emission of nanocrystal solution with or without C_3-S-HBr is 510 nm or 513 nm, respectively. However, the C_3-S-HBr NC solution exhibits narrow FWHM. The C_3-S-HBr NCs exhibit clear Urbach absorption edge and lower Urbach energy Figure 3.5c, indicating better passivation of C_3-S-HBr treated nanocrystals. This result corresponds with the transient photoluminescence (TRPL) characterisation of perovskite nanocrystal film, shown in Figure 3.5d. The fitted parameters of TRPL are listed in Table 3.1. The three components of lifetimes are 9.87 (57.64%), 2.60 (15.57%), and 28.86 (26.78%) ns for C_3-S DEHPA film. For DEHPA film, the three components of lifetimes are 8.52 (49.93%), 34.41 (18.78%), and 2.71 (31.29%) ns. The result implies that there are three channels responsible for observed emissions. The Intensity-Weighted effective lifetime is calculated by following the equation:

$$\tau_{eff} = \frac{\sum_{i=1}^{n} B_i \tau_i^2}{\sum_{i=1}^{n} B_i \tau_i^2} \quad (3.1)$$

The effective exciton lifetime of C_3-S-HBr nanocrystals is 13.82 ns. This value is higher than the controlled nanocrystals, whose effective exciton lifetime is 11.56 ns, as

described above. The result indicates that C_3-S-HBr nanocrystals have relatively low defect density.

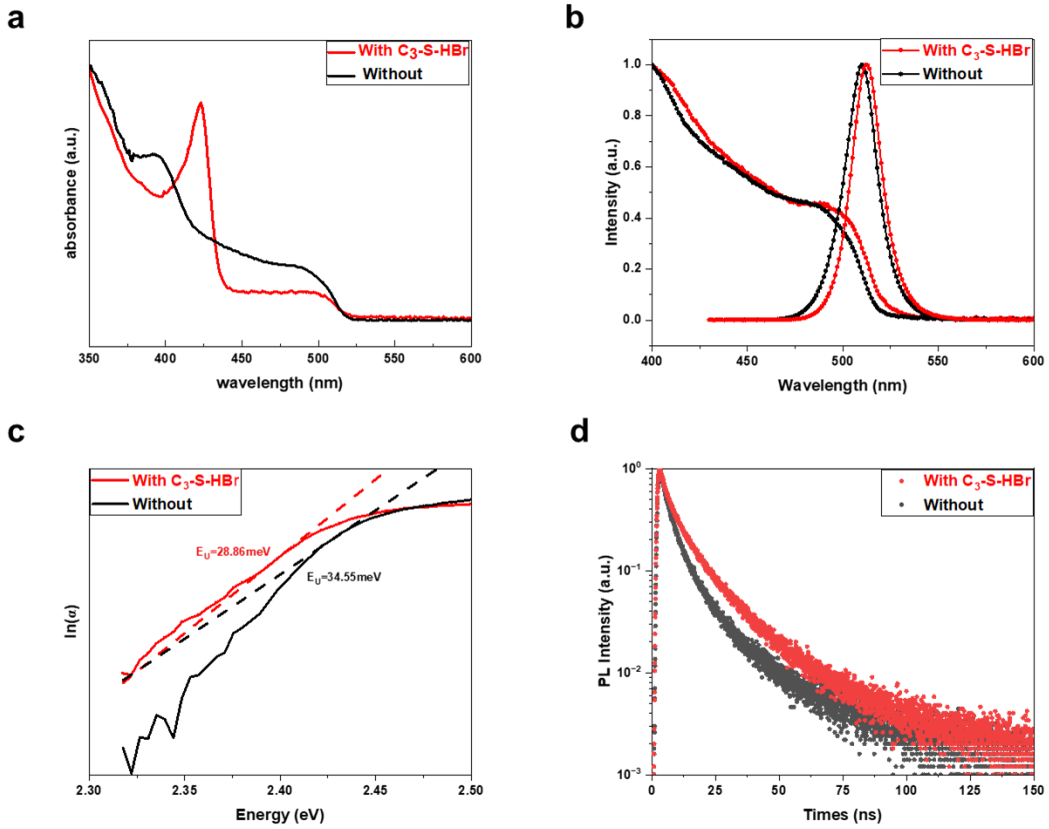

Figure 3.5 | Optical properties of PeNC solution with or without C_3-S-HBr treatment. (a) absorption spectra of pristine solution (no purification), (b) absorption and photoluminescence spectra of purified NC solution, (c) Urbach energy diagram for PeNCs, (d) Transient PL of synthesised NC thin films.

Table 3.1 | Parameters used for fitting the PL decay of perovskite NC film with or without C_3-S passivation.

	τ_1(ns)	τ_2(ns)	τ_3(ns)	B_1	B_2	B_3	$\tau_{eff.}$(ns)
C_3-S DEHPA film	9.87	2.60	28.86	2212.309	2268.873	351.5839	13.82
DEHPA film	8.52	34.41	2.71	1578.861	146.9923	3109.993	11.56

Works in Chapter 3 were published: Zhang, X., Wang, Q., Yao, Z., Deng, M., Wang, J., Qian, L., Ren, Y., Yan, Y., Xiang, C., 2023. Adv. Sci. 10, 1–7. Zhang, X., Yao, Z., Deng, M., Wu, R., Wang, J., Ren, Y., Wang, C., Jia, G., Qian, L., Xiang, C., 2024. J. Mater. Chem. C.

The XRD result of purified perovskite nanocrystal films in Figure 3.6a also proves that C_3-S-HBr nanocrystal films are better crystallised cubic $CsPbBr_3$. The perovskite nanocrystal with C_3-S-HBr passivation manifests a narrow full width of half maximum (FWHM) of (200) crystal face peak. The TEM image in Figure 3.6b manifested a uniform shape of synthesised perovskite nanocrystal with C_3-S-HBr. The scale bar in Figure 3.6b is 10 nm, and the particle size observed from the image is around 12 nm.

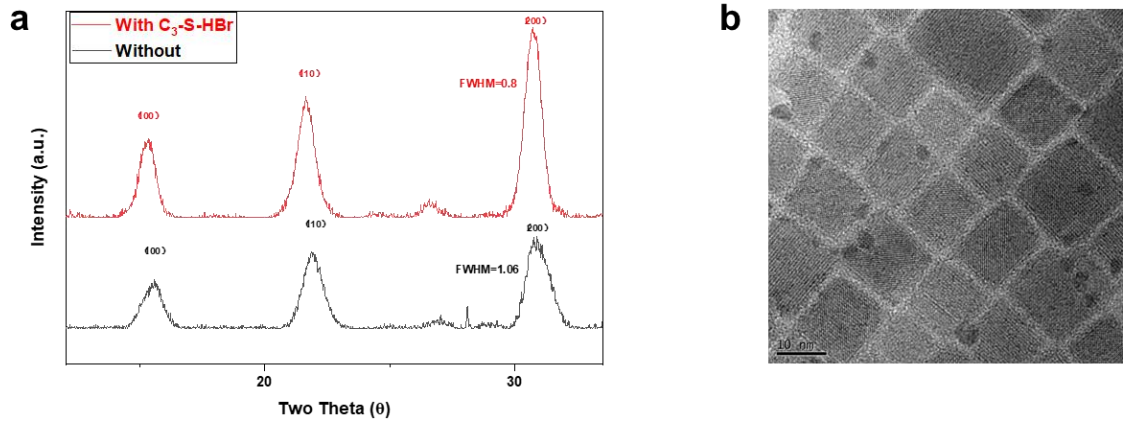

Figure 3.6 | (a) X-ray refraction patterns of synthesised perovskite nanocrystal films. (b) TEM image of C_3-S-HBr PeNCs.

Figure 3.7a is the FTIR spectra of synthesised NC films. The characteristic peaks are marked. According to the FTIR spectra, there are no carboxylic acid or phosphoric acid peaks. In addition, there are two peaks at 1165 cm^{-1} and 1031.7 cm^{-1}, which can be attributed to sulfonic acid. The results indicate that the original precursor ligands OA/phosphoric acid are replaced by C_3-S-HBr in the ligand exchange process. The TGA in Figure 3.7b of C_3-S-HBr nanocrystals demonstrates the increment of organic ligands on the nanocrystal surface(X. Zhang et al., 2023). The weight ratio of ligands of OA/OAm nanocrystals passivated with C_3-S is usually 15% to 20%(Krieg et al., 2018), while DEHPA/OAm nanocrystals passivated with C_3-S was 25% to 30%. Due to strong chemical binding and chelation effects, the C_3-S ligand shell is hard to lose. Thus, it can protect the inner crystal structure from polar solvents, oxygen, and water.

Works in Chapter 3 were published: Zhang, X., Wang, Q., Yao, Z., Deng, M., Wang, J., Qian, L., Ren, Y., Yan, Y., Xiang, C., 2023. Adv. Sci. 10, 1–7. Zhang, X., Yao, Z., Deng, M., Wu, R., Wang, J., Ren, Y., Wang, C., Jia, G., Qian, L., Xiang, C., 2024. J. Mater. Chem. C.

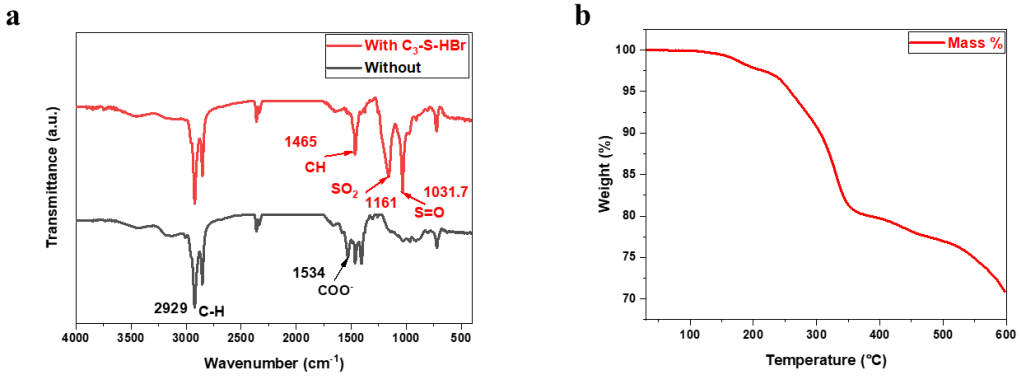

Figure 3.7 | (a) FTIR spectra of synthesised nanocrystals with or without C_3-S-HBr (b) TGA of synthesised DEHPA nanocrystals passivated with C_3-S.

Figure 3.8 shows the XPS spectra of synthesised NC films. According to the XPS characterisation, compared to pristine NCs, the XPS Pb 4*f* peaks of C_3-S-HBr nanocrystals shift 0.4 eV to higher energy levels. For example, the Pb $4f^{7/2}$ peak shifts from 138.1 eV to 138.5 eV. The XPS Br 3*d* peaks of C_3-S-HBr nanocrystals also shift 0.4 eV to higher energy levels, as manifested in Figure 3.8b. The higher binding energy implies stronger ligand binding. The ligand density on the NCs' surfaces also influences the energy shift magnitude. The NC films exhibit good resistance to polar solvents, which can bear zinc oxides in an ethanol solution thanks to the potent ligand binding and high ligand density.

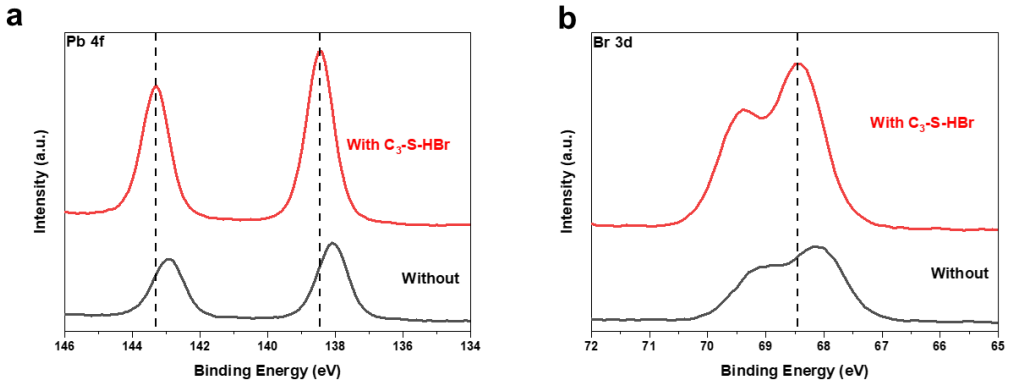

Figure 3.8 | XPS (a) Pb 4*f*, (b) Br 3*d* of perovskite NC films with/without C_3-S-HBr treatment.

Works in Chapter 3 were published: Zhang, X., Wang, Q., Yao, Z., Deng, M., Wang, J., Qian, L., Ren, Y., Yan, Y., Xiang, C., 2023. Adv. Sci. 10, 1–7. Zhang, X., Yao, Z., Deng, M., Wu, R., Wang, J., Ren, Y., Wang, C., Jia, G., Qian, L., Xiang, C., 2024. J. Mater. Chem. C.

The synthesised nanocrystal solution exhibited excellent storage stability. The PLQY of synthesised nanocrystal solution does not significantly decrease after storing for 280 days, which can keep 90% of the initial PL intensity, as shown in Figure 3.9a. The photoluminescence stability of synthesised C_3-S-HBr nanocrystal film was measured under different temperatures in the glove box, manifested in Figure 3.9b. The perovskite nanocrystal film can keep 80% of the initial PL intensity, even elevating the temperature to 100 ℃. The PL intensity dropped to 60% of the initial PL intensity when the temperature was 120 ℃. Surprisingly, the PL intensity of C_3-S-HBr perovskite film can be kept stable when we heated the perovskite nanocrystal film to 80 ℃ in the ambient environment (relative humidity of 80%). These results are comparable to the state-of-the-art perovskite nanocrystal film, which can strongly suppress heat-induced fluorescence quenching(M. Liu et al., 2021).

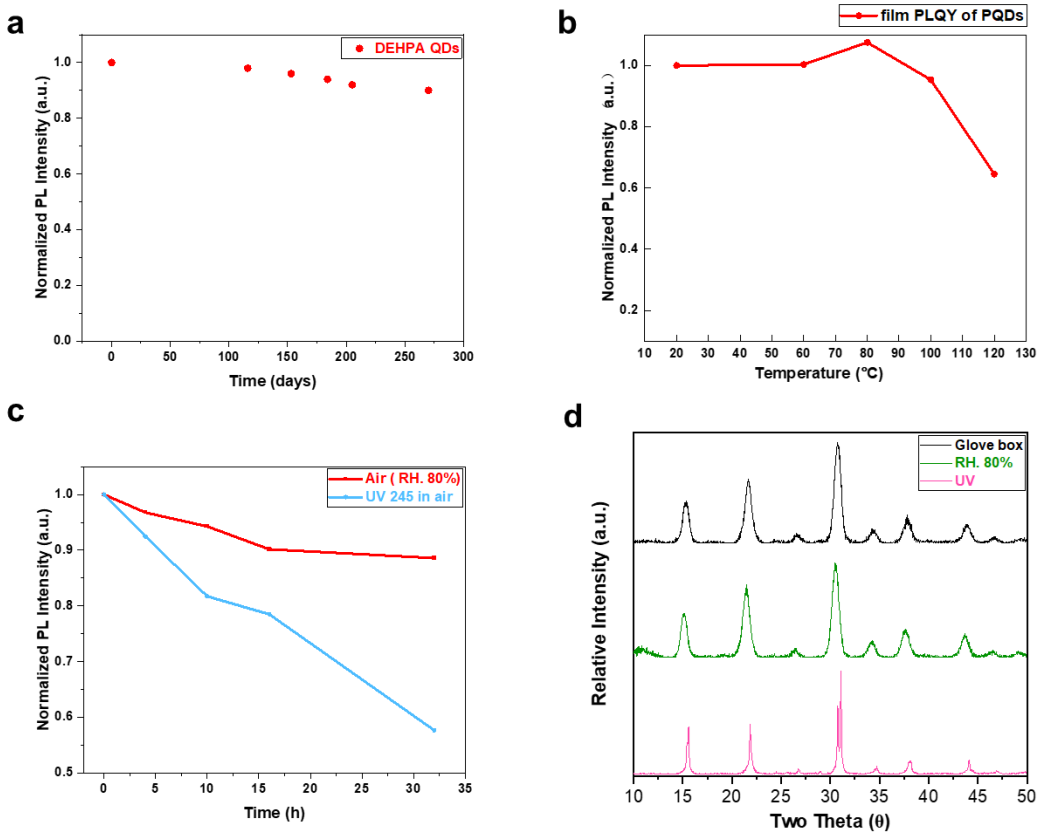

Figure 3.9 | Stability of PeNCs. (a) Storage stability of synthesised C_3-S-HBr NC solution, (b) PL Intensity at different temperatures for perovskite NC film with/without C_3-S-HBr, (c) PL Intensity of C_3-S-HBr perovskite NC film in the ambient environment and under

UV 254, (d) XRD spectra of perovskite NC film in the glove box, ambient environments, and under UV 254.

Figure 3.9c is the photoluminescence stability of C_3-S-HBr perovskite nanocrystal films in the ambient environment (humidity up to 80%) and under UV 245 illumination. The C_3-S-HBr perovskite NC film has strong resistance to oxygen and water, which can maintain 90% initial PL intensity after 16 hours. The film can hold nearly 80% of the initial PL intensity after exposure to UV 254 for 16 hours. Figure 3.9d shows XRD spectra of synthesised NC films stored in different conditions. After being irradiated under UV 254 for 16 hours, the XRD spectra peak split and became shaper. This is because the NC film loses ligands and aggregates to bulk. In contrast, the film XRD spectra do not change when stored in an ambient environment with RH.80%. Possible explanations for the excellent environmental stability of the synthesised perovskite NC film can be attributed to the strong binding of zwitterionic ligands.

3.3 Nucleation and growth control with short-chain ligands

OTAc/OTAm Modified Nanocrystals. Short-chain length ligands, such as OTAc/OTAm, dodecanoic acid, dodecylamine, and hexanoic acid, produce large-size NCs and nanoplates. The nucleation and growth kinetics of NCs can be controlled using different precursor ligands. Therefore, nanocrystal size distribution can be narrowed with proper precursor ligands. In addition, the conductivity of NC film can be enhanced by using short-chain precursor ligands. To further improve the performance of PeQLEDs, short-chain length precursor ligands are used to replace OA/OAm, which aims to narrow the size distribution of NCs while increasing their conductivity. NCs aggregate if the precursor ligand chain length is too short. OTAc and OTAm were selected in this thesis due to the proper chain length, which can maintain an efficient repulsive force between NCs. The amount of OTAc/OTAm used in the method is optimised. The total amount of acid or amine ligands is fixed as 3.3 mmol (approximately 1 mL for OA or OAm). The molar ratio of OA: OAm: OTAc: OTAm is 3:3:2:2 (0.6, 0.6, 0.2,0.2 mL), 2:2:3:3 (0.4, 0.4, 0.3, 0.3 mL), and 3:3:8:8 (0.3, 0.3, 0.4, 0.4 mL). With the increment of the number

of short-chain ligands, the EQE of the device increases. However, the NCs severely aggregate when the molar ratio of OA: OAm: OTAc: OTAm is 1:1:4:4 (0.2, 0.2, 0.4, 0.4 mL).

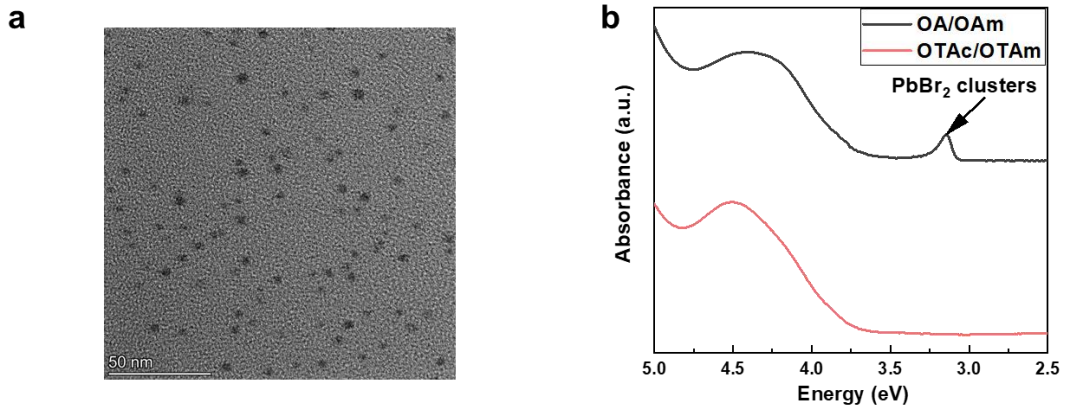

Figure 3.10 | (a) TEM image of formed $PbBr_2$ clusters in OA/OAm method (b) absorption spectra of precursor solutions with different precursor ligands.

OA/OAm NC synthesised by PbX_2 precursors ordinarily suffers from inhomogeneous nucleation due to the formation of clusters induced by the high concentration of halo plumbate ionic solute. The observed $PbBr_2$ clusters are presented in the TEM image (Figure 3.10a). By partially replacing OA/OAm ligands with OTAc/OTAm, cluster forming can be inhibited, as shown in Figure 3.10b. To further explore the influence of OTAc/OTAm, the NC nucleation and growth evolution were monitored by in-situ PL measurement. Figure 3.11a and b are measured in-situ PL of synthesised $CsPbBr_3$ NCs. It is observed that the OTAc/OTAm method synthesised NCs possess a narrower size distribution and larger particle size than the OA/OAm method. Figure 3.11c and d are extracted emission peak evolution of synthesised $CsPbBr_3$ NCs. They indicate that the OTAc/OTAm method forms larger particle sizes and grows faster than the OA/OAm method in 2 s. Then, the NC growth in the OTAc/OTAm method is inhibited by the resurfacing agent, while the OA/OAm method maintains growth and leads to aggregation. The OA/OAm method formed many nuclei at 200 ms, much more than the OTAc/OTAm method, as shown in Figure 3.11e. This is comprehensive as $PbBr_2$

clusters provide an extra nucleation pathway. The extracted PL FWHM evolution of different methods is presented in Figure 3.11f. It is observed that the OTAc/OTAm method has a narrower FWHM, indicating better size distribution.

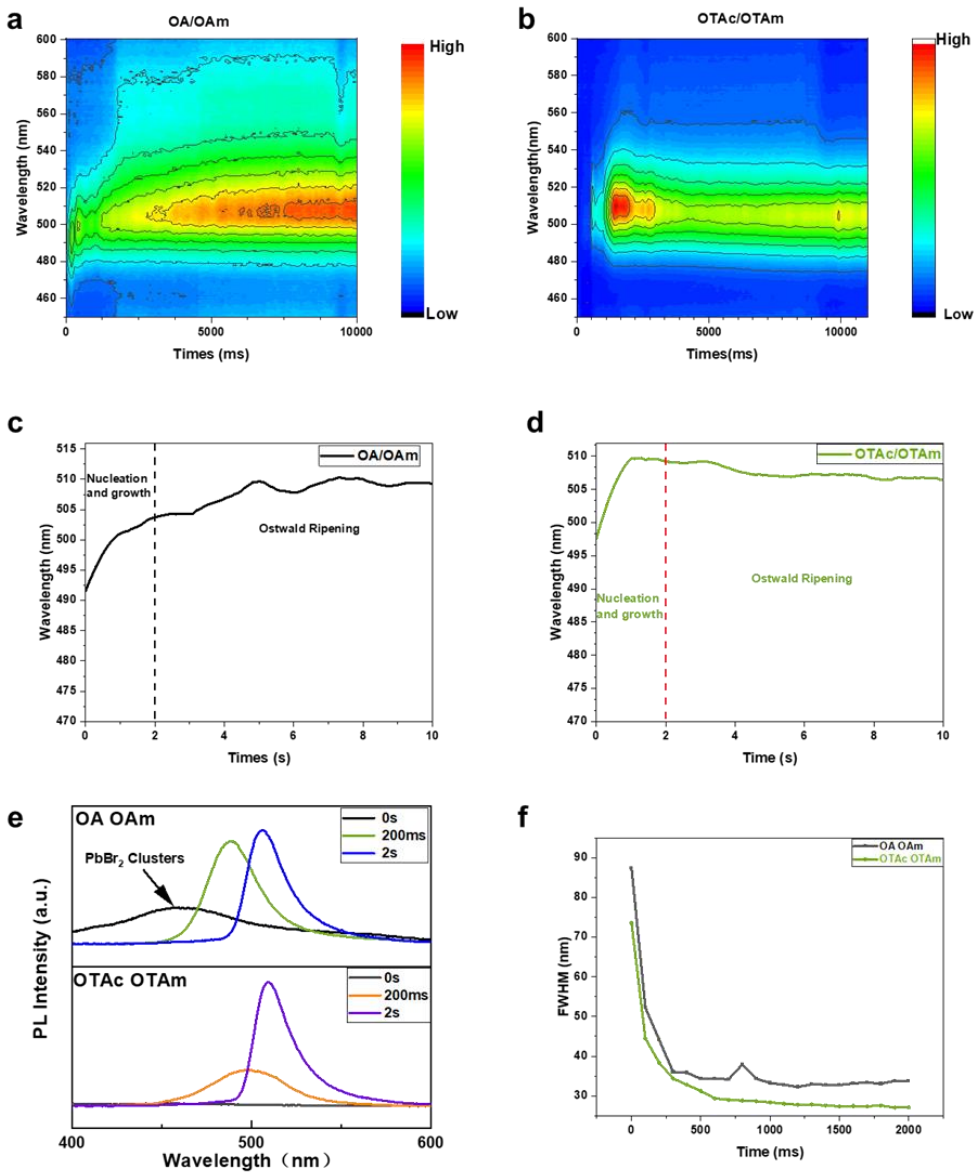

Figure 3.11 | In-situ PL spectra of synthesised PeNCs. In-situ PL of perovskite NCs nucleation and growth is (a) OA/OAm and (b) OTAc/OTAm. Extracted Emission peak evolution of (c) OA/OAm and (d) OTAc/OTAm based $CsPbBr_3$ NCs. (e) extracted PL from in-situ PL measurement at different reaction times, 0 s, 200 ms, and 2 s. (f) extracted PL FWHM evolution in the synthesis process. Due to the quantum confinement effect, the size of the nanocrystal correlated to its emission peak.

Works in Chapter 3 were published: Zhang, X., Wang, Q., Yao, Z., Deng, M., Wang, J., Qian, L., Ren, Y., Yan, Y., Xiang, C., 2023. Adv. Sci. 10, 1–7. Zhang, X., Yao, Z., Deng, M., Wu, R., Wang, J., Ren, Y., Wang, C., Jia, G., Qian, L., Xiang, C., 2024. J. Mater. Chem. C.

The size distribution of NCs is further characterised by DLS measurement, as shown in Figures 3.12a and b. The OTAc/OTAm method has a peak particle size at 17 nm with an FWHM of 5.6 nm, while the OA/OAm method exhibits a peak particle size at 13 nm with an FWHM of 12 nm. The result indicates that the OTAc/OTAm method achieves a narrower size distribution.

Figure 3.12c is XRD spectra synthesised NC films. The peaks are marked by corresponding lattice planes. The OTAc/OTAm NCs have a narrower FWHM. For example, the peak FWHM of the (200) lattice plane is 0.442 degrees for OTAc/OTAm NCs and 0.682 degrees for OA/OAm NCs. The results imply that OTAc/OTAm precursor ligands can improve the crystallinity of PeNCs. The crystal faces are marked based on the standard PDF card JCPDS No.18-0365 in Figure 3.12d.

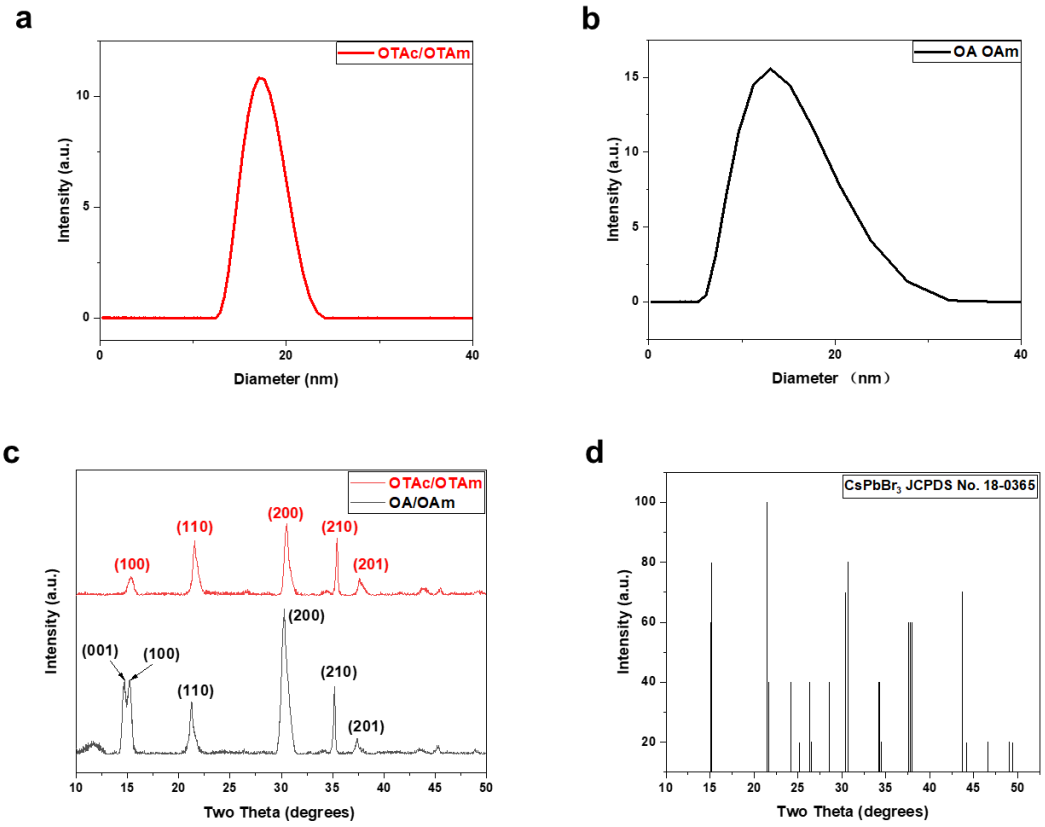

Figure 3.12 | Measured perovskite NCs size distribution by DLS (a) OTAc/OTAm, (b) OA/OAm. (c) XRD pattern of different NCs films on ITO glass (d) standard PDF card of $CsPbBr_3$.

Figure 3.13a and b manifest TEM images of different precursor ligands synthesised NCs. OTAc/OTAm NCs exhibit uniform shapes and clear images. The particle size of OTAc/OTAm evaluated is 13 nm, corresponding to the measured peak particle size in DLS (the peak particle size in DLS is several nanometers larger than TEM due to the ligand shell). The OA/OAm method shows a particle size of 8 nm (PL peak at 510 nm).

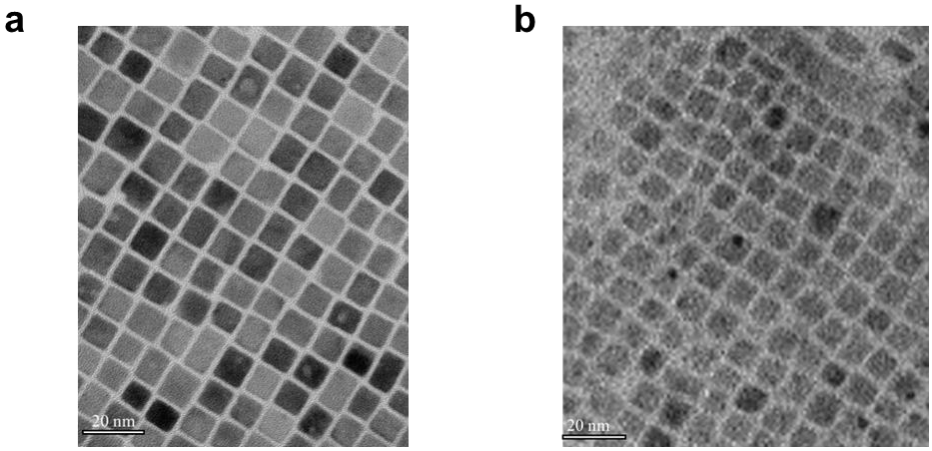

Figure 3.13 | TEM image of purified perovskite nanocrystals, (a) OTAc/OTAm, (b) OA/OAm.

The synthesised OTAc/OTAm NCs have good surface passivation and achieve good optical performance. As shown in Figure 3.14a, the synthesised OTAc/OTAm LHP NCs have narrow PL spectra with a peak of 515 nm and an FWHM of 18 nm. The narrow emission can be attributed to narrow size distribution. In addition, the emission peak is red shift compared to OA/OAm NCs. The red shift is attributed to larger particle size. The transient photoluminescence (TRPL) performance of the perovskite films is shown in Figure 3.14b. The fitting details of TRPL are listed in Table 3.2. τ_1 is the lifetime of monomolecular recombination, which consists of trap-assistant nonradiative recombination and monomolecular exciton recombination. As the OTAc/OTAm NCs possess much higher PLQY, the increased τ_1 is monomolecular exciton recombination. τ_2 is bimolecular exciton recombination. The much longer lifetime of bimolecular exciton recombination indicates that bimolecular exciton recombination is an important mechanism contributing to emissions. τ_3 is trimolecular recombination which is

attributed to Auger recombination. The effective photoluminescence lifetime of C_3-S-HBr passivated OTAc/OTAm LHP NCs was 25.75 ns, while the synthesised C_3-S-HBr DEHPA/OAm NCs were 13.82 ns, as mentioned above. The much longer effective photoluminescence lifetime of C_3-S-HBr passivated OTAc/OTAm LHP NCs indicates better passivation and reduction of defects. The near unity PLQY of the C_3-S-HBr passivated OTAc/OAm NC solution has been measured.

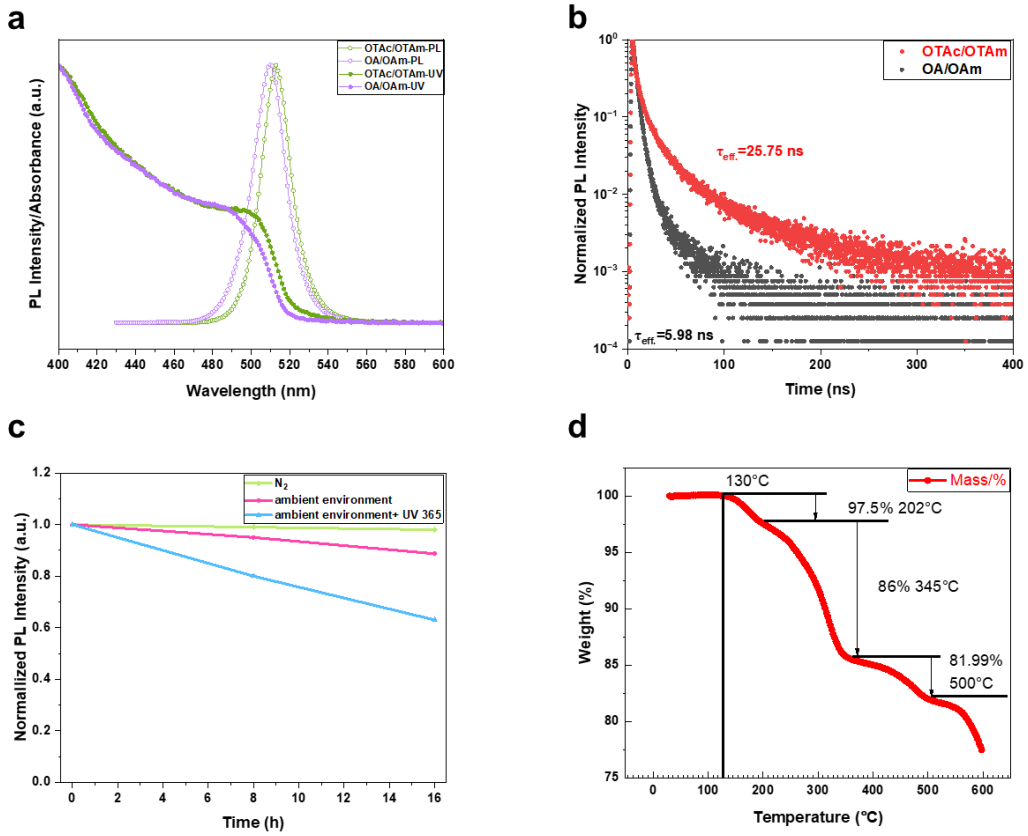

Figure 3.14 | (a) PL spectra of synthesised NCs. (b)TRPL of synthesised perovskite film. (c)PLQY of OTAc/OTAm perovskite NC film in the ambient environment and UV 365. (d) TGA curve of OTAc/OTAm perovskite NCs.

The stability of C_3-S-HBr passivated OTAc/OTAm LHP NC films is studied in the ambient environment or under UV radiation. The C_3-S-HBr passivated OTAc/OTAm perovskite NC film manifests good oxygen, moisture, and UV light resistance. Figure 3.14c shows the PL intensity of OTAc/OTAm LHP NC film kept up to 90% after 16

hours in the ambient environment (humidity 80%). When the nanocrystal film was continually exposed to UV 365 for 16 hours under the same ambient environment, it could keep nearly 60% of its initial PL intensity. In contrast, DEHPA perovskite nanocrystal films manifested better environmental stability. The relatively insufficient environmental stability of OTAc/OTAm NCs is the relatively weak binding of OTAc/OTAm ligands.

Table 3.2 | Parameters used for fitting the PL decay of C_3-S-HBr passivated OTAc/OTAm and OA/OAm perovskite nanocrystal film.

	τ1(ns)	τ2(ns)	τ3(ns)	B_1	B_2	B_3	$\tau_{eff.}$(ns)
OTAc/OTAm LHP film	14.22	73.14	2.75	1844.703	190.3808	5666.055	25.75
OA/OAm LHP film	3.75	23.32		7847.748	162.2948		5.98

As shown in Figure 3.14d, the ligands weight ratio of OTAc/OTAm nanocrystals was only 18%. This value is much less than C_3-S-HBr passivated DEHPA/OAm NCs. The relatively low ligand content of C_3-S-HBr passivated OTAc/OTAm NCs influences the stability of perovskite nanocrystal film. However, the film stability of C_3-S-HBr passivated OTAc/OTAm nanocrystals is much better than OA/OAm nanocrystals, which can satisfy the fabrication and operation requirements of QLEDs. A lower organic ligand weight ratio means better conductivity, as inorganic perovskite has high charge mobility. Therefore, it is reasonable to sacrifice partial stability to improve the electric properties of perovskite quantum dots.

The surface chemistry and ligands binding of synthesised NCs are characterised. Figure 3.15a is the FTIR spectra of synthesised NCs. In the FTIR spectra of C_3-S-HBr passivated OTAc/OTAm NC film, there are two peaks at 1465 cm^{-1} and 1589 $cm^{-1,}$ which can be attributed to C-H bending and quaternary ammonium groups (antisymmetric deformation of primary amine salt) respectively. In contrast, these two peaks for DEHPA-synthesized nanocrystals were extremely weak. The result indicates that C_3-S-HBr

passivated OTAc/OTAm NCs had a higher original precursor ligands ratio, which means C_3-S-HBr passivated DEHPA NCs achieve more efficient in-situ ligand exchange. However, C_3-S-HBr passivated OTAc/OTAm have short chain lengths and can achieve better conductivity. The resurface agent was mainly used for passivation. The competition between precursor ligands and zwitterionic ligands prohibited unwanted ligand exchange. The two absorption peaks at 1165 cm^{-1} and 1035 cm^{-1} are related to the sulfonic groups (symmetric stretching of SO_2 and antisymmetric stretching of S-O).

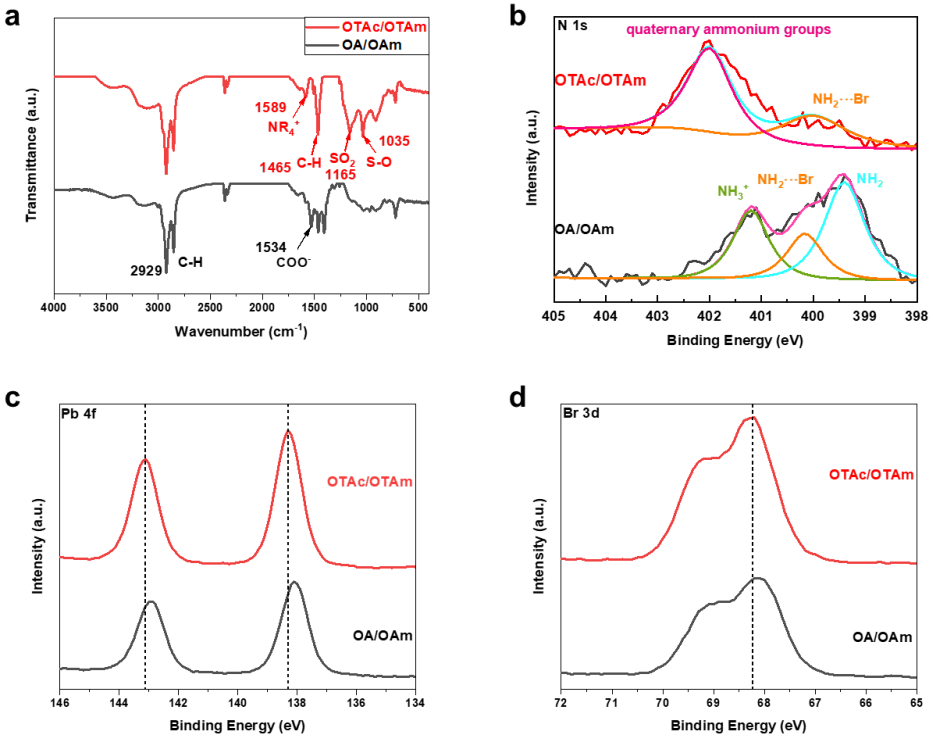

Figure 3.15 | (a) FTIR spectra of C_3-S-HBr passivated OTAc/OTAm and OA/OAm NCs. High-resolution XPS of C_3-S-HBr passivated OTAc/OTAm and OA/OAm perovskite NC film, (d)Pb 4*f*, (e)Br 3*d*, (f) N 1*s*.

The film XPS measurement demonstrated strong chemical interaction between resurfacing agents and perovskite NCs. This result is similar to DEHPA-synthesized nanocrystals. In Figure 3.15b, c, and d, it is observed that the Pb 4*f*, Br 3*d*, and N 1*s* peaks of C_3-S-HBr passivated OTAc/OTAm LHP NC film all shift to higher binding energy compared with the OA/OAm LHP NC film, indicating that C_3-S-HBr passivated

OTAc/OTAm LHP NCs have more potent surface ligands binding. Moreover, for the N 1*s* peaks of C_3-S-HBr passivated OTAc/OTAm LHP NCs, the peak intensity of binding energy located at 402 eV is more potent than at 400 eV. The strong peak can be attributed to quaternary ammonium ions. Together with the results in FTIR measurements, the OTAc/OTAm nanocrystal surface is well passivated with C_3-S-HBr. Moreover, the perovskite nanocrystal films exhibited excellent charge mobility compared to OA/OAm nanocrystal films.

3.4 Device performance with different ligands

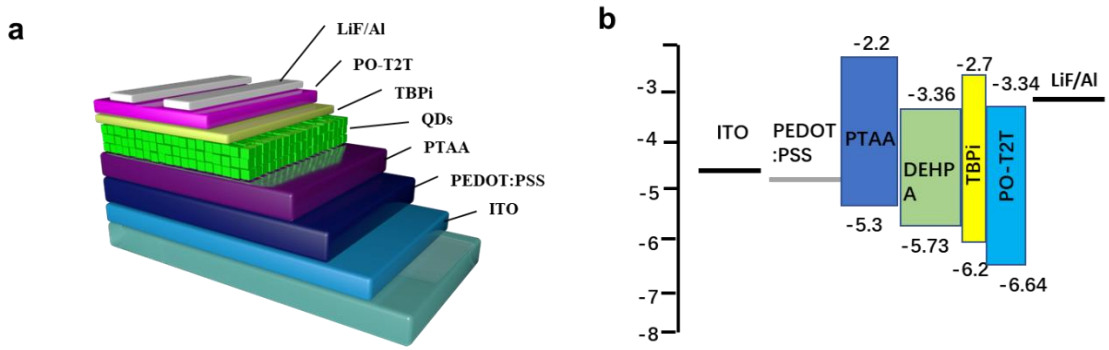

Figure 3.16 | (a) Schematic diagram of PeQLED structure. (b) Energy diagram of perovskite QLEDs.

The C_3-S-HBr passivated DEHPA/OAm NCs are applied to QLEDs. As shown in Figure 3.16a, the fabricated device structure is ITO/PEDOT: PSS/PTAA/LHP NCs/TPBI/PO-T2T/LiF/Al. Figure 3.16b is an energy level diagram of the device structure. The energy levels of QD film are characterised by UPS measurement. The energy level of perovskite film indicates that C_3-S ligands do not block carrier injection. TPBi is a good electron injection layer. However, the single TPBi ETL layer has the disadvantage of low charge transport ability, resulting in low current density and high turn-on voltage. In addition, perovskite NC film presents fluorescence quenching when directly touched with PO-T2T(Fang et al., 2021). Therefore, the double ETL structure design is applied. The double ETL structure designed can achieve efficient electron

injection and fast charge transport. Moreover, this design can also balance the charge of the whole device as PO-T2T possesses comparable carrier mobility compared to PTAA.

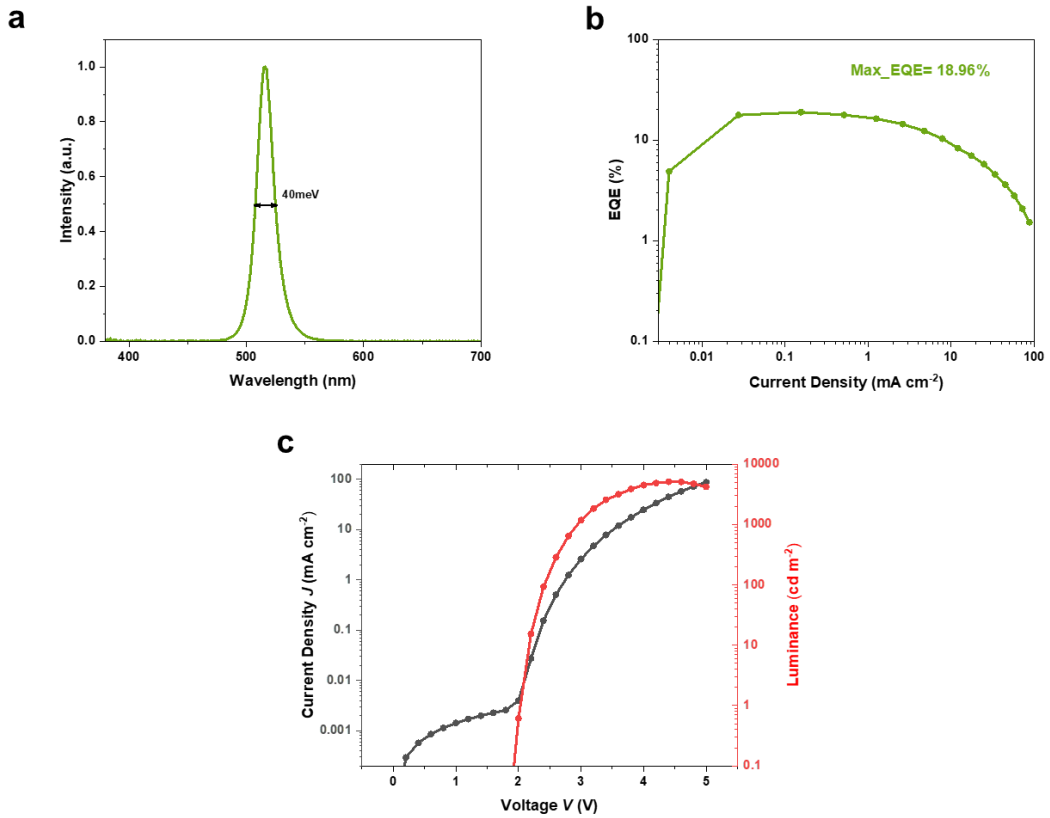

Figure 3.17 | (a) Electroluminescence spectra of QLEDs. (b) EQE versus current density of perovskite QLEDs. (c) Luminescence and current density versus voltage of perovskite QLEDs.

The EL of the fabricated device is located at 515 nm with an FWHM of 18 nm in Figure 3.17a. For the first time of device fabrication, the EQE was only 5%. After optimising the fabrication process and thickness of the hole and electron transport layers, the external efficiency of our champion device reached 18.96%. Details of device performance are described by luminescence and EQE versus current density in Figure 3.17b. Luminescence and current density versus voltage are depicted in Figure 3.17c. According to these curves, the fabricated PeQLEDs achieved a sub-bandgap turn-on voltage of 2 V (defined as voltage where luminance is 1 cd·m^{-2}), which indicates good charge injection in the low voltage range. The device reaches maximum EQE quickly after turning on. However, the device shows noticeable EQE roll-off in high current

density, and the maximum luminance is only 5113 cd·m^{-2}. As the ligand content of C_3-S-HBr passivated DEHPA/OAm QDs is very high, the EQE roll-off and low maximum luminance can be explained by the excess insulating contents in the QD film. Although the perovskite QD film shows excellent stability, the fabricated device is quickly broken due to charge accumulation when operating at a relatively high current density.

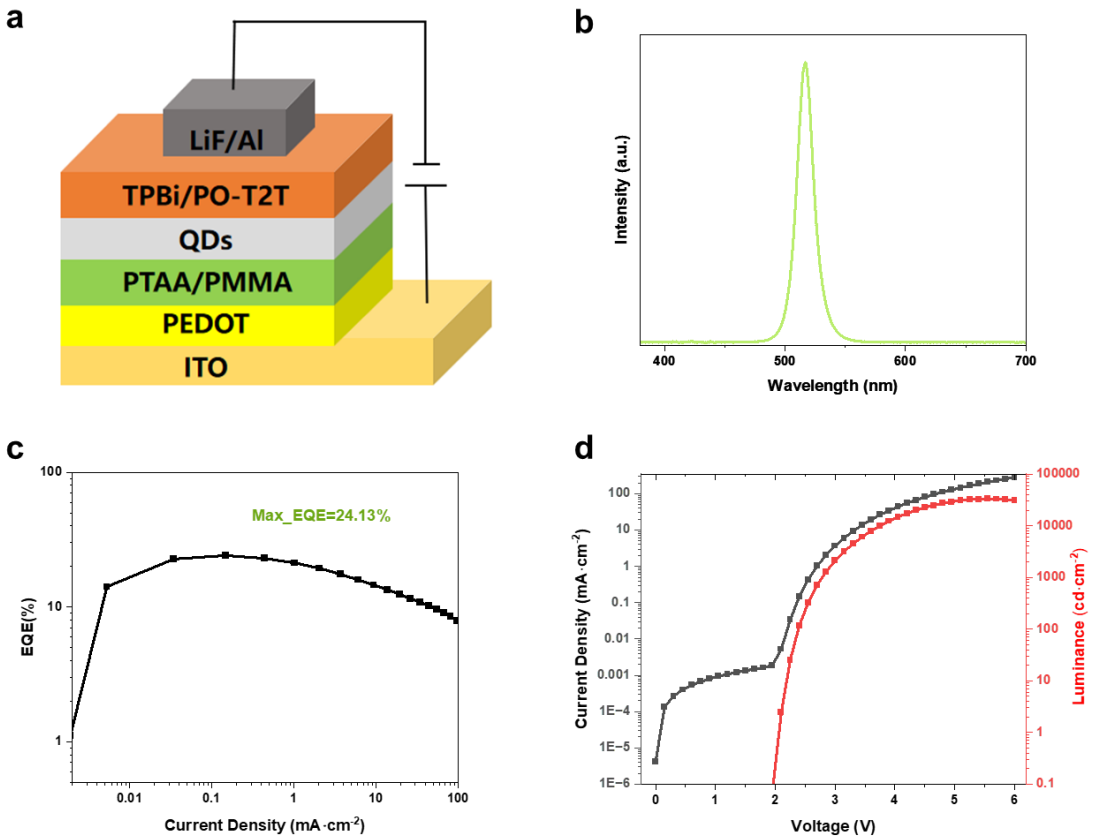

Figure 3.18 | (a) Device Structure of perovskite QLED. (b) Electroluminescence of Green QLEDs. (c) EQE versus current density of green perovskite QLEDs. (d) J-V-L of perovskite QLEDs.

Efficient and stable PeQLEDs are fabricated using C_3-S-HBr passivated OTAc/OTAm NCs. The device structure for C_3-S-HBr passivated OTAc/OTAm NCs is ITO/PEDOT: PSS/PTAA/PMMA/LHP NCs/TPBI/PO-T2T/LiF/Al as manifested in Figure 3.18a. For C_3-S-HBr passivated OTAc/OTAm NCs, there is an interface layer PMMA on the hole transport layer PTAA(Wang et al., 2023). The C_3-S-HBr passivated

OTAc/OTAm NCs have lower ligand contents than C_3-S-HBr passivated DEHPA/OAm QDs. The C_3-S-HBr passivated OTAc/OTAm NCs film exhibits fluorescence quenching on PTAA. Therefore, this interface layer is covered on PTAA to reduce fluorescence quenching and balance charge injection of the QLEDs(Wang et al., 2023). In addition, the polymer PMMA can further passivate lead defects of perovskite nanocrystal films(Shen et al., 2023).

The EL of the champion device is located at 517 nm with FWHM at 16.1 nm, as manifested in Figure 3.18b. Compared to corresponding PL spectra, the EL redshift has a narrower FWHM caused by Forster resonance energy transfer and field-induced Stark effect. The maximum EQE of optimised PeQLEDs reaches 24.13%, as shown in Figure 3.18c. The device also reaches maximum EQE fast after turning it on. Figure 3.18d is the *J-V-L* curve of the device; the device turn-on voltage is 2 V with a maximum luminance of 33009 cd m^{-2} at 5.55 V. Compared to C_3-S-HBr passivated DEHPA/OAm QDs, the C_3-S-HBr passivated OTAc/OTAm NCs have a much higher device luminance and relieve the EQE roll-off. This can be attributed to improved charge transport ability by short-chain length ligands.

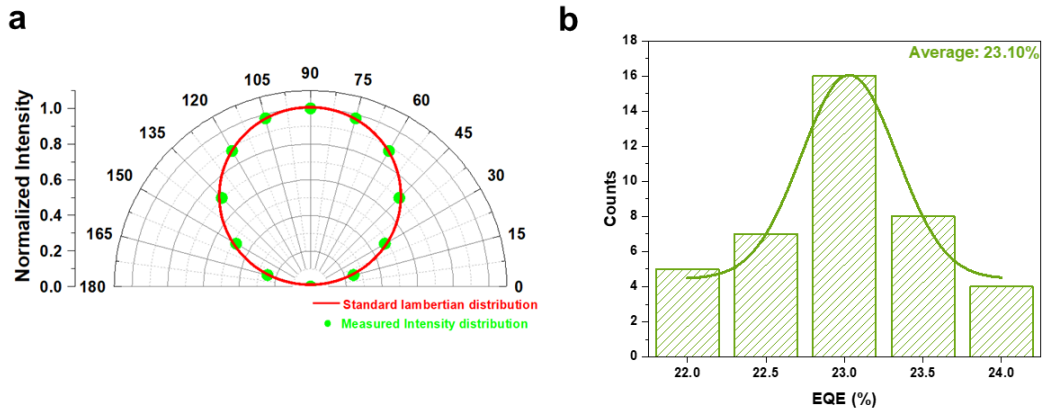

Figure 3.19 | (a) Measured intensity distribution and standard Lambertian distribution. (b) EQE distribution of 40 devices.

The angular intensity distribution of fabricated LEDs is measured to ensure they are Lambertian emissions, as shown in Figure 3.19a. To prove the reproducibility of the

experiments, the performance of 40 devices is measured. The calculated average EQE of 40 devices is 23.10±0.53%. The EQE distribution of 40 devices is fitted using the Gauss Function.

The energy diagram of C_3-S-HBr passivated OTAc/OTAm NCs-based devices is shown in Figure 3.20a. Compared to C_3-S-HBr passivated DEHPA/OAm NCs, C_3-S-HBr passivated OTAc/OTAm NCs film energy levels shift upper and have a lower hole injection barrier. Moreover, the fabricated hole-only device proves that C_3-S-HBr passivated OTAc/OTAm NC films have higher charge transport ability (Figure 3.20b). The hole-only device based on C_3-S-HBr passivated OTAc/OTAm NC exhibited much higher current density than OA/OAm NC film when under the same voltage bias.

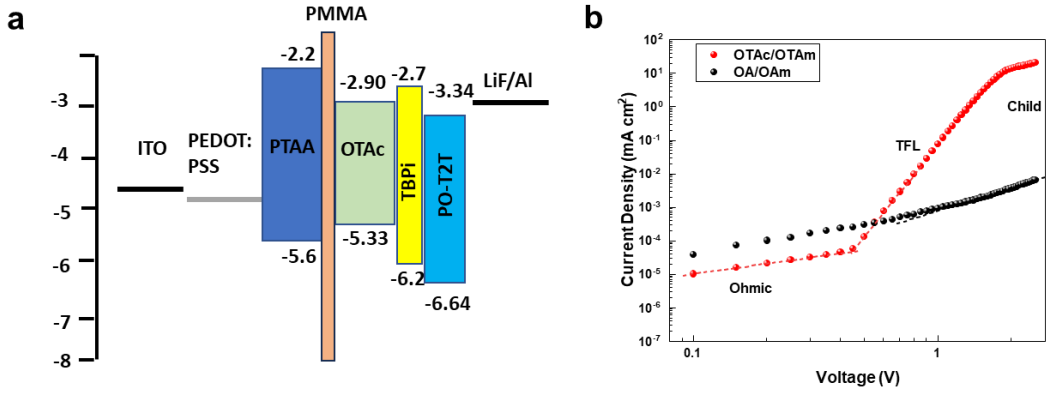

Figure 3.20 | (a) energy diagram of devices based on C3-S-HBr passivated OTAc/OTAm NCs (b) current density versus voltage curve of hole-only device with different perovskite NC films.

The amine ligand used after injecting the C_3-S-HBr resurfaces agent is F-PEA for the champion device, as shown in Figure 3.1a. F-PEA ligand shows a maximum EQE of 24.13%. In contrast, PEA manifests a maximum EQE of 21.60%, while DOAm exhibits a maximum EQE of 14.80%. NCs synthesised with other amine ligands, such as PEA and DOAm, exhibit lower EQE than F-PEA. Other ligands used in the posttreatment process, such as F-OPA and HPA, are also tried (Figure 3.21b). The three ligands show different device performances with a maximum EQE of 1.54, 7.58, and 19.13%, respectively. The

OPA ligands have the best device performance among the three ligands. HPA and F-OPA induce PeNCs ligand loss and lead octahedral decomposition. This is because HPA and F-OPA have stronger polarity and higher dissociation constants than OPA.

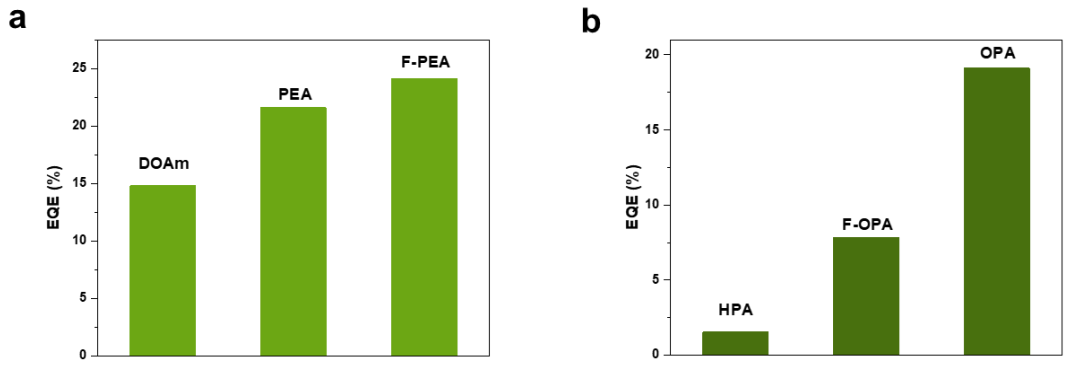

Figure 3.21 | (a) device EQE with different amine ligands synthesised NCs (b) device EQE with different acid ligands used in posttreatment.

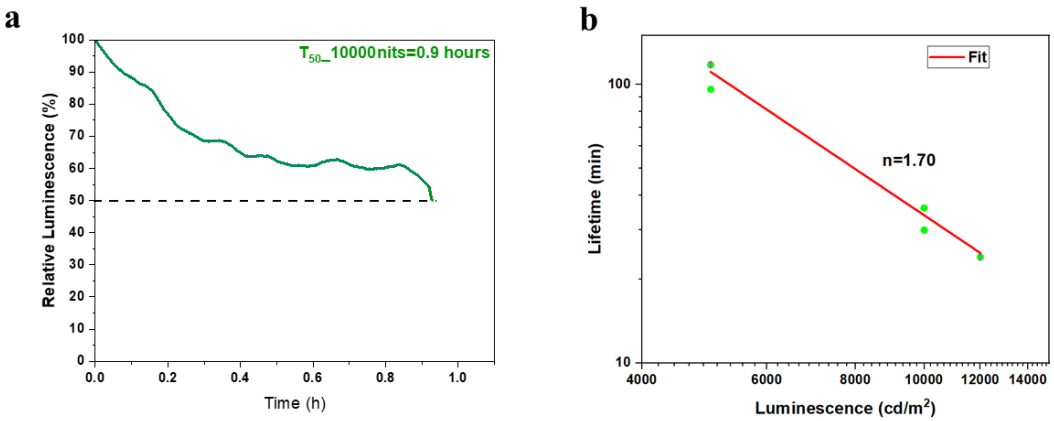

Figure 3.22 | (a) Operation stability of perovskite QLEDs. (b) Device operation lifetime of fabricated PeQLEDs at different initial luminescence.

The device operation stability is also measured here. Figure 3.22a is the measured operation lifetime of the champion device. At the initial brightness of 10000 cd·m^{-2}, the T_{50} (the time when the luminance drops to 50% of the initial value) reached 54 min. The T_{50} at 1000 cd·m^{-2} was estimated to fit with the empirical equation.

$$L_0^n \times T_{50} = constant \quad (3.1)$$

Works in Chapter 3 were published: Zhang, X., Wang, Q., Yao, Z., Deng, M., Wang, J., Qian, L., Ren, Y., Yan, Y., Xiang, C., 2023. Adv. Sci. 10, 1–7. Zhang, X., Yao, Z., Deng, M., Wu, R., Wang, J., Ren, Y., Wang, C., Jia, G., Qian, L., Xiang, C., 2024. J. Mater. Chem. C.

where L_0 is the initial brightness and n is the acceleration factor. The acceleration factor is calculated by fitting the T50 data at different initial brightness levels. The fitting line is manifested in Figure 3.22b. The device achieved record operation stability and EQE with a planar device structure that did not contain an extra outcoupling design in 2023. Currently, the degradation of PeQLEDs is attributed to the instability of PeQDs. PeQLEDs accumulate charges due to unbalanced charge injection or charge transport. The accumulated charges induce ligand loss of PeQD films, decreasing PLQY. Strong ligands have higher binding energy to PeQDs than weak ligands OA/OAm. Thus, the ligands loss and PLQY quenching induced by accumulated charge can be relieved. As a result, the device operation stability is improved.

Figure 3.23a is the TRPL of the C_3-S-HBr passivated OA/OAm NC film. The measured effective lifetime is 12.20 ns, and this value is much lower than the passivated DEHPA/OAm and OTAc/OTAm PeNCs. The C_3-S-HBr passivated OA/OAm NCs-based device is also fabricated as a reference for contrast. The peak EQE of the device is 12.52%.

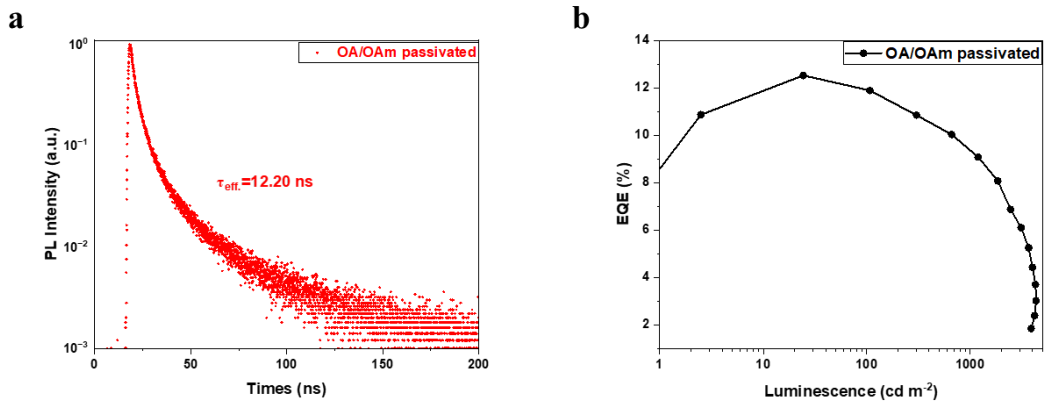

Figure 3.23 | OA/OAm nanocrystals passivated with C_3-S-HBr (a) TRPL of perovskite NC film, (b) EQE versus luminescence curve of fabricated device.

3.5 Summary

This chapter develops strategies to synthesise stable LHP NCs for EL applications, including in-situ ligand exchange with potent ligands, homogenous nucleation, and

growth control. Moreover, the device structure is customised according to the properties of LHP NCs. Stable and efficient $CsPbBr_3$ NCs are synthesised and achieve a peak EQE of 24.13% with world record operation lifetime.

First is defects passivation with ligands engineering. Several potent ligands are used to passivate LHP NCs. The zwitterionic ligands (C_3-S) react with HBr to form a resurfacing agent. This resurfacing agent is used for in-situ passivation and suppression of Ostwald ripening. Amine ligands (PEA, DOAm, DDDAm, F-PEA) assist passivating PeNCs in the in-situ ligands exchange process. In the purification process, OPA ligands are added to reduce ligand loss. The obtained LHP NCs exhibited excellent optical properties and good environmental stability. UV-vis absorption spectra, PL spectra, PLQY, and TRPL, characterise the optical properties of LHP NCs.

Precursor ligands significantly influence the performance of synthesised LHP NCs. C_3-S-HBr passivated OA/OAm $CsPbBr_3$ NCs do not manifest good device performance. The peak EQE for the champion device is 12.52%, with a maximum luminescence of 4000 $cd \cdot m^{-2}$. DEHPA is applied to replace the OA to improve device performance. DEHPA can facilitate the C_3-S ligands exchange process. The surface ligands are characterised by FTIR and XPS measurements. TGA measures the ligand's weight ratio of different LHP NCs. Consequently, the optical properties and environmental stability of QDs are further enhanced. However, the PeQELD performance is not satisfactory. The maximum EQE of the champion QLEDs based on C_3-S-HBr passivate DEHPA $CsPbBr_3$ QDs is 18.96% with a maximum luminance of 5113 $cd \cdot m^{-2}$.

Short chain-length ligands can improve the conductivity of LHP NCs. OTAc/OTAm ligands are used to increase the EQE and luminance. In addition, it is observed that intermediate $PbBr_2$ clusters can be eliminated by partially replacing OA/OAm with OTAc/OTAm. Therefore, using OTAc/OTAm can control the nucleation paths of synthesis. Uniform shape LHP NCs with narrow size distribution are synthesised. The C_3-S-HBr passivated OTAc/OTAm NCs show good optical and electrical properties. The fabricated device exhibits ultra-narrow EL spectra at 517 nm with an FWHM of 16 nm.

Works in Chapter 3 were published: Zhang, X., Wang, Q., Yao, Z., Deng, M., Wang, J., Qian, L., Ren, Y., Yan, Y., Xiang, C., 2023. Adv. Sci. 10, 1–7. Zhang, X., Yao, Z., Deng, M., Wu, R., Wang, J., Ren, Y., Wang, C., Jia, G., Qian, L., Xiang, C., 2024. J. Mater. Chem. C.

A peak EQE of 24.13% is achieved with maximum luminance over 30000 $cd \cdot m^{-2}$. Nevertheless, the environmental stability of these NCs is slightly weaker than the C_3-S-HBr passivated DEHPA NCs. There is an interface layer between C_3-S-HBr passivated OTAc/OTAm NCs and PTAA HTL. These devices achieve a world record operation lifetime for green PeQLEDs.

Works in Chapter 3 were published: Zhang, X., Wang, Q., Yao, Z., Deng, M., Wang, J., Qian, L., Ren, Y., Yan, Y., Xiang, C., 2023. Adv. Sci. 10, 1–7. Zhang, X., Yao, Z., Deng, M., Wu, R., Wang, J., Ren, Y., Wang, C., Jia, G., Qian, L., Xiang, C., 2024. J. Mater. Chem. C.

Chapter 4. Pure Red $CsPbI_3$ Quantum Dots and Electroluminescence

4.1 Background

The particle size of deep blue $CsPbBr_3$ is usually 3~4 nm, while the particle size of pure red $CsPbI_3$ NCs is 4~5 nm. It is hard to gain such small NCs due to synthesis difficulty. In addition, ultra-small-size NCs possess a larger surface area and high surface defect density, which induce aggregation and regrowth of NCs, resulting in PL redshift(Xu et al., 2018). As mentioned in the previous report, LHP NCs are intrinsic ionic with dynamic surfaces, which quickly lose surface ligands(De Roo et al., 2016; Tan et al., 2018). These characteristics exacerbate the instability of small-size LHP NCs and require good surface passivation for high PLQY. As the usually used thermodynamic equilibrium method to control the particle size can only achieve crimson and sky-blue emission(Dong et al., 2018), it is challenging to synthesise stable deep blue $CsPbBr_3$ and pure red $CsPbI_3$ NCs. In this method, the small-size NCs are passivated well with excess halide ions in solution and achieve high PLQY. However, the PLQY dropped significantly after purification and NC regrowth due to ligand loss. To my knowledge, there is no report of stable pure red $CsPbI_3$ NCs for EL applications because of NCs regrowth after twice purification. LEDs based on deep blue $CsPbBr_3$ are rarely reported(Bi et al., 2021; Tu et al., 2021; M. Zhang et al., 2023). Efforts for small-size $CsPbI_3$ NC synthesis are focused on post-treatment and passivation of defects, as mentioned in the previous report, to enhance the performance of LEDs by improving the charge transport ability of QDs (Lan et al., 2021; Ya‐Kun Wang et al., 2021). Although $CsPbI_3$ NCs-based QLEDs have achieved EQE exceeding 20% with an emission wavelength of 636 nm~ 640 nm, the results do not satisfy industrial needs due to the broadened FWHM (usually around 40 nm).

By following the synthesis method proposed for $CsPbBr_3$ NCs in the previous chapter, a resurfacing agent for $CsPbI_3$ NCs is synthesised, which is reacted by hydroiodic acid and 5-amino valeric acid (5AVA) at 80 ℃(Y. Li et al., 2024a). Although the resurfacing agent (5AVAI) can improve PLQY and stability of $CsPbI_3$ NCs, it cannot enhance the quantum confinement or decrease the particle size of $CsPbI_3$ NCs. The

optimised champion QLED based on the 5AVAI $CsPbI_3$ NCs achieved 24.45% EQE with an EL of 645 nm. A growth control strategy is proposed to synthesise ultra-small-size $CsPbBr_3$ or $CsPbI_3$ quantum dots. Acids were introduced after nucleation to control the acid-base equilibrium and prohibit harmful Ostwald ripening. In addition, it can further exchange weak oleylamine ligands. Taking pure red $CsPbI_3$ QDs synthesis as an example, the comparison of our method and the previously reported method is manifested in Figure 4.1.

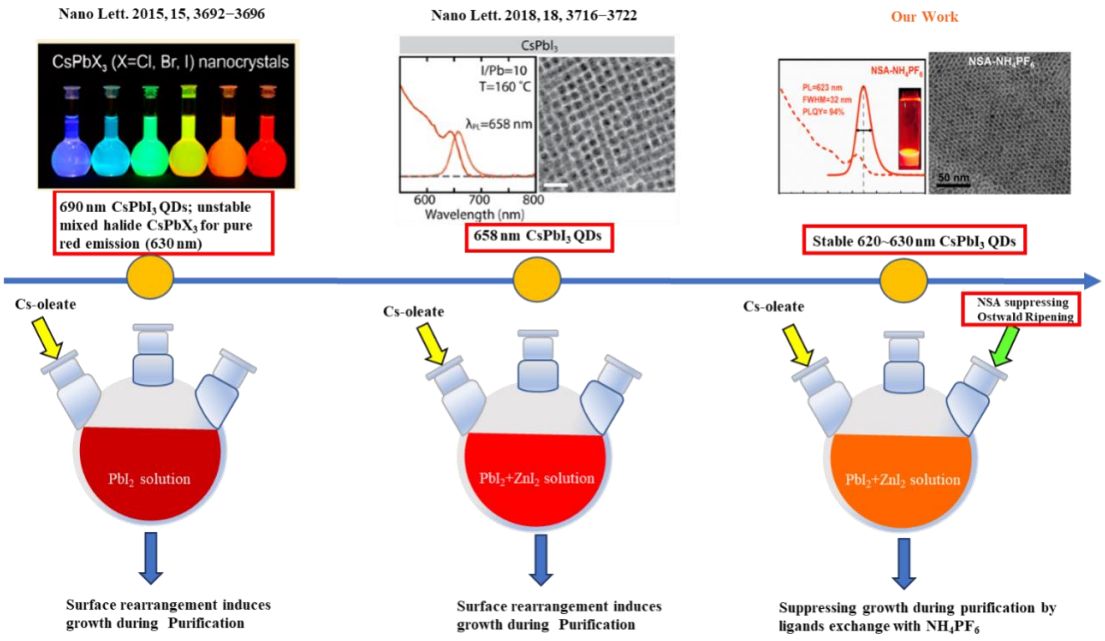

Figure 4.1 | Comparison of the previously reported method and our synthesis strategy.

4.2 Resurface agent 5AVAI passivated $CsPbI_3$ NCs

Initially, C_3-S-HI was used as a resurfacing agent to synthesise $CsPbI_3$ QDs. However, the fabricated devices show low EQE and current density. It is possible that the chain length of C_3-S-HI is too long to achieve good charge transport ability for small-size $CsPbI_3$ QDs. Therefore, 5AVAI, which has a 5-carbon chain, was used. The in-situ ligands exchange mechanism of 5AVAI passivated $CsPbI_3$ NCs is similar to the C_3-S-HBr passivated $CsPbBr_3$ NCs described in the previous chapter. Cs cations and I anions vacancies are major surface defects of $CsPbI_3$ NCs. 5AVA is also a kind of zwitterionic ligand. Figure 4.2 is a schematic illustration of the in-situ ligand exchange process, which has the exact ligand exchange mechanism as the C_3-S-HBr(Y. Li et al., 2024a).

Specifically, the proton transfer between OA and OAm ligands is enhanced, inducing OA/OAm ligand desorption and facilitating zwitterionic ligand bound to NCs. The molecular form OAm is significantly decreased by adding 5AVAI.

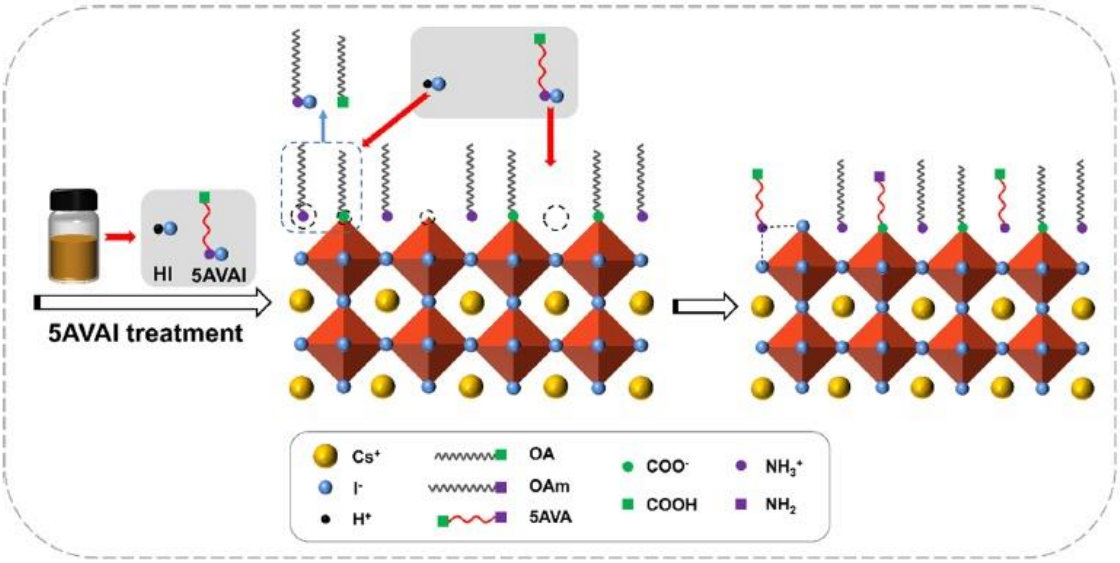

Figure 4.2 | Schematic illustration of resurface agent 5AVAI exchange OA/OAm ligand and passivating $CsPbI_3$ NCs(Y. Li et al., 2024a).

The amount of 5AVAI added in synthesis is explored. The optimised amount of 5AVAI is 0.2 mmol, which possesses 95% PLQY for the champion sample. The NCs passivated with 5AVAI exhibited better optical properties than OA/OAm NCs. In Figure 4.3a, the synthesised OA/OAm $CsPbI_3$ NCs have PLQY of 69%, while 5AVAI passivated NCs manifest PLQY of 87%. In addition, the PL spectra indicate that 5AVAI passivated NCs have narrower FWHM and the emission peak blue shifts. It is known that excess iodine anions cause perovskite NCs emission peak blue shift.

As shown in Figure 4.3b, the synthesised 5AVAI passivated $CsPbI_3$ NC solution demonstrates good storage stability and maintains 70% PLQY after storing it in the air for 20 days. On the contrary, the OA/OAm NCs degrade to a yellow phase without optical activity. TEM images of Figure 4.3c and d are synthesised $CsPbI_3$ NC with or without 5AVAI passivation. Passivated $CsPbI_3$ NCs are monodispersed with uniform shape and have a size distribution of 5.29 ± 0.76 nm. In contrast, OA/OAm NCs show various shapes

and possess a size distribution of 5.88 ± 1.16 nm. In addition, NC aggregation is also observed in Figure 4.3d, which explains the PLQY decrease in OA/OAm NCs. The result corresponds to the PL spectra.

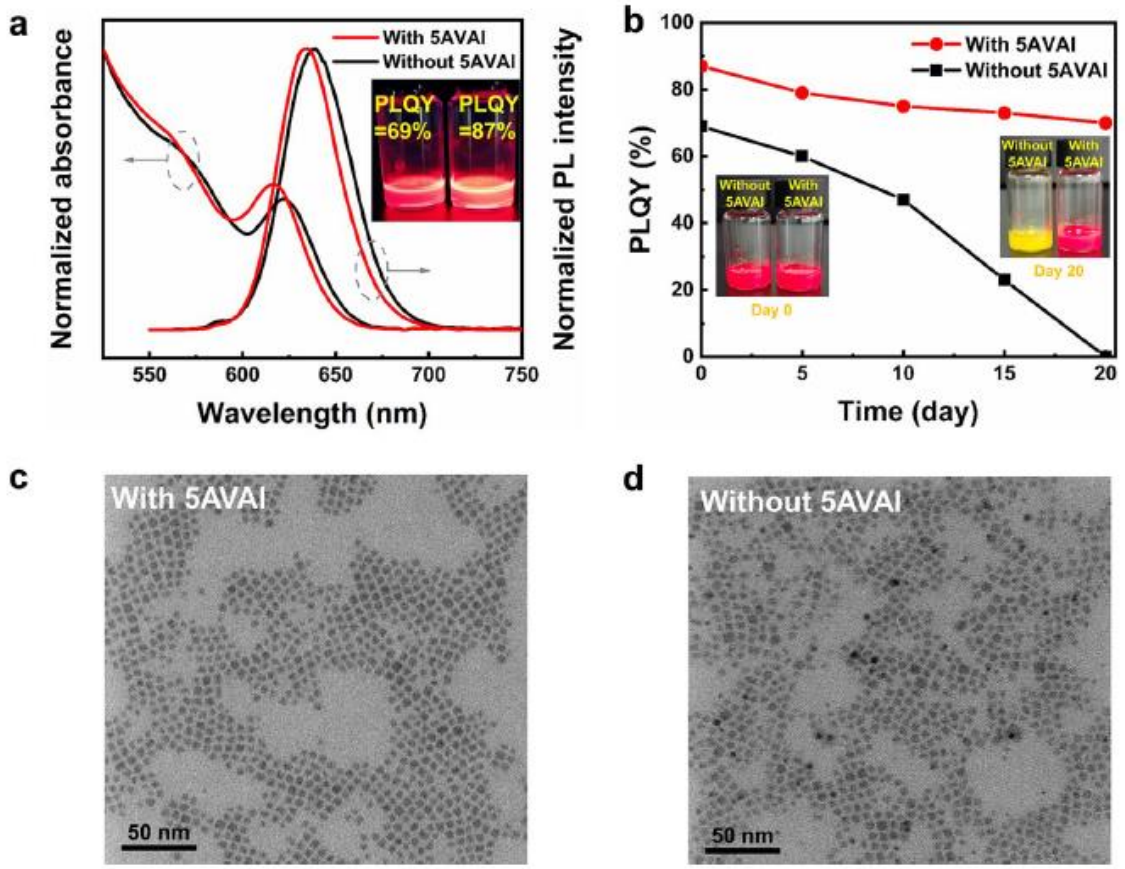

Figure 4.3 | Optical properties and TEM images of synthesised PeNCs with or without 5AVAI. (a) Absorption and PL spectra of synthesised $CsPbI_3$ QDs. The inset images are QD solutions (left: without 5AVAI; right: with 5AVAI) under UV light excitation (365 nm) and the measured PLQY. (b) Stability of synthesised $CsPbI_3$ QDs stored in ambient conditions (temperature of 25 ± 5 °C and humidity of 50 ± 10%), the inset images are QD solutions after different storage days. TEM images of $CsPbI_3$ QDs (c) with 5AVAI, (d) without 5AVAI(Y. Li et al., 2024a).

The synthesised NC films are characterised by FTIR measurement (Figure 4.4a). Compared to NCs without 5AVAI, the C-N stretching vibration peak at 907 cm^{-1} is dramatically enhanced. This peak is attributed to 5AVA. The result indicates that

zwitterionic ionic ligands 5AVA are bound to the NC surface. Figure 4.4b is TGA curve of different PeNC powders. The measured temperature range is 0 to 500 ℃ as organic ligands thoroughly decompose at 500 ℃. 5AVA ligands have short-chain lengths compared to OA/OAm ligands. Therefore, ligand weight ratio of 5AVAI passivated $CsPbI_3$ NCs decreases. The ligand weight ratio of 5AVA passivated PeNCs is 32%, while without passivation is 34%.

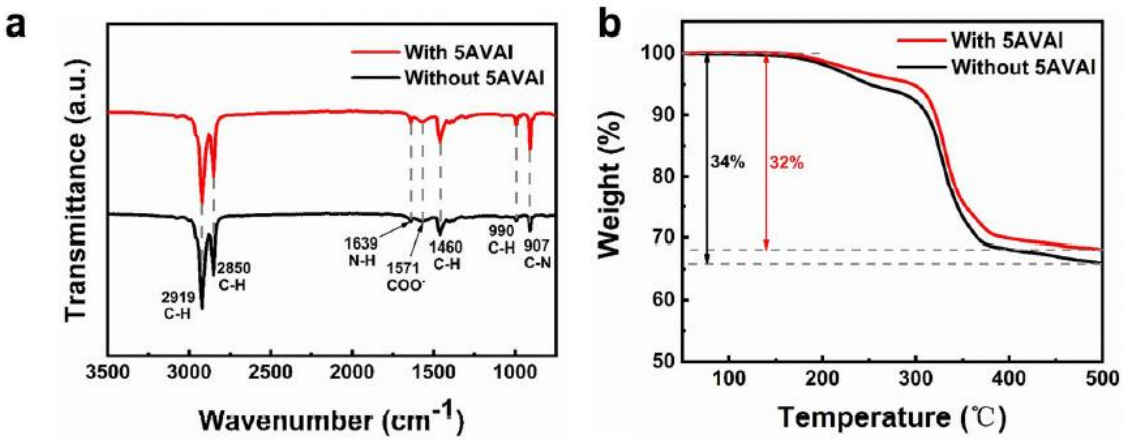

Figure 4.4 | (a) FITR spectra of synthesised NC films with or without 5AVAI passivation. (b) TGA curve of synthesised NCs with or without 5AVAI(Y. Li et al., 2024a).

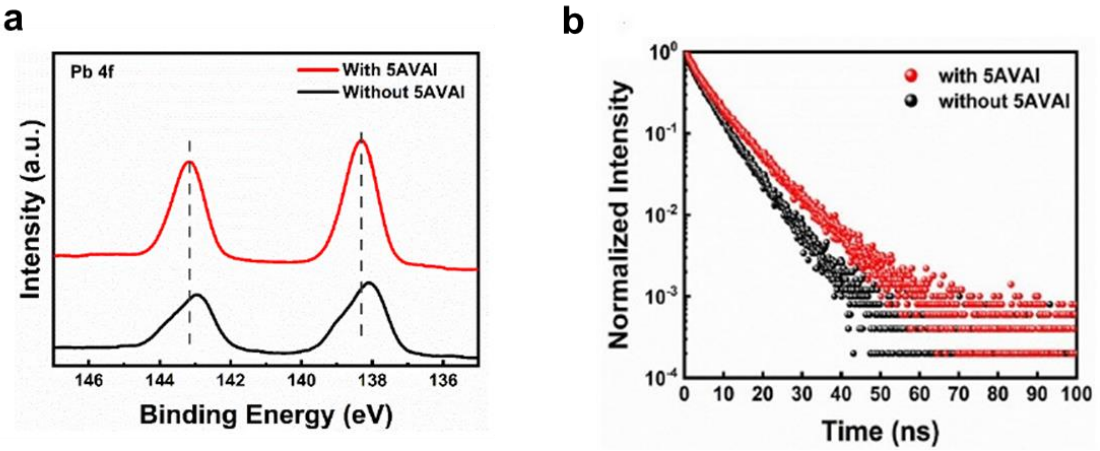

Figure 4.5 | (a)XPS Pb 4*f* of synthesised NC films with or without 5AVAI passivation. (b) TRPL of synthesised NCs with or without 5AVAI(Y. Li et al., 2024a).

Moreover, the binding energy of Pb 4*f* of NC films shifts to higher energy when

treated with 5AVA, as shown in Figure 4.5a. The binding energy shift is attributed to the strong binding of 5AVA ligands. In addition, the XPS Pb 4*f* spectra peaks of NCs without 5AVA are asymmetrical due to uncoordinated Pb atoms. The result indicates that there are lots of vacancies in PeNC films without 5AVA. Figure 4.5b is the TRPL of synthesised NC films. The average exciton lifetime calculated from the fitting curves is 7.1 ns for NCs with 5AVAI. For OA/OAm NCs, the average exciton lifetime is 5.5 ns. The longer exciton lifetime indicates the efficient passivation of surface defects in 5AVAI NCs.

4.3 Pure red $CsPbI_3$ synthesised by growth suppression

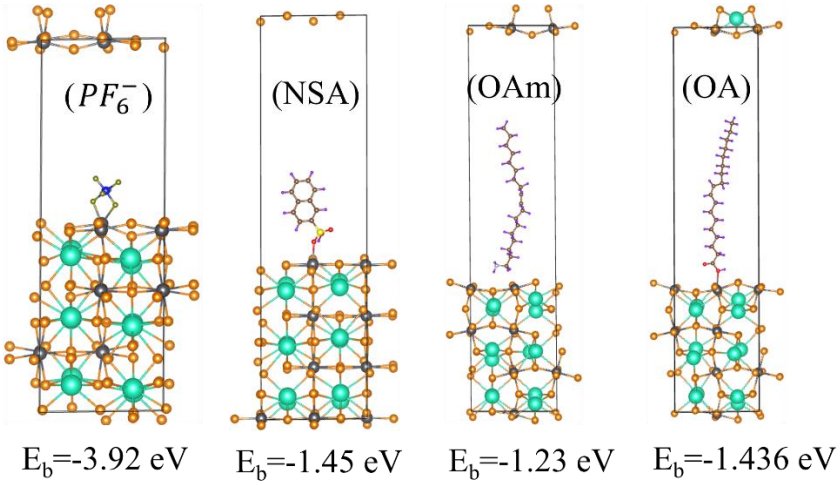

Figure 4.6 | Calculated binding energy of OA, OAm, NSA, and NH_4PF_6 ligands through DFT.

For pure red $CsPbI_3$ QDs synthesis, the 2-naphthalene sulfonic acid (NSA) are used. The injected NSA ligand can push the proton transfer process between OA^- and $OAmH^+$, thus producing lots of $OAmH^+$ and removing OA/OAm ligands from QD surfaces(Almeida et al., 2018). The chemical reactions of this reverse process are shown as follows:

$$OAm + OA \leftrightarrow OAmH^+ + OA^- \quad (4.1)$$

$$OAm + NSA \rightarrow OAmH^+ + NSA^- \quad (4.2)$$

It is demonstrated here (Figure 4.6) that the sulfonic acid group has more muscular binding energy with Pb atoms on the QDs surface compared to OAm by DFT calculation, which replaces the original weak-bounding OAm ligands on the surface of QDs to reduce the generation of active perovskite ionic sites. The naphthalene ring of the NSA ligand also has a considerable steric hindrance, inhibiting the overgrowth of QDs. The function of NSA ligands is similar to C_3-S-HBr used for $CsPbBr_3$, but NAS ligands are aromatic molecules possessing strengths in electron transport.

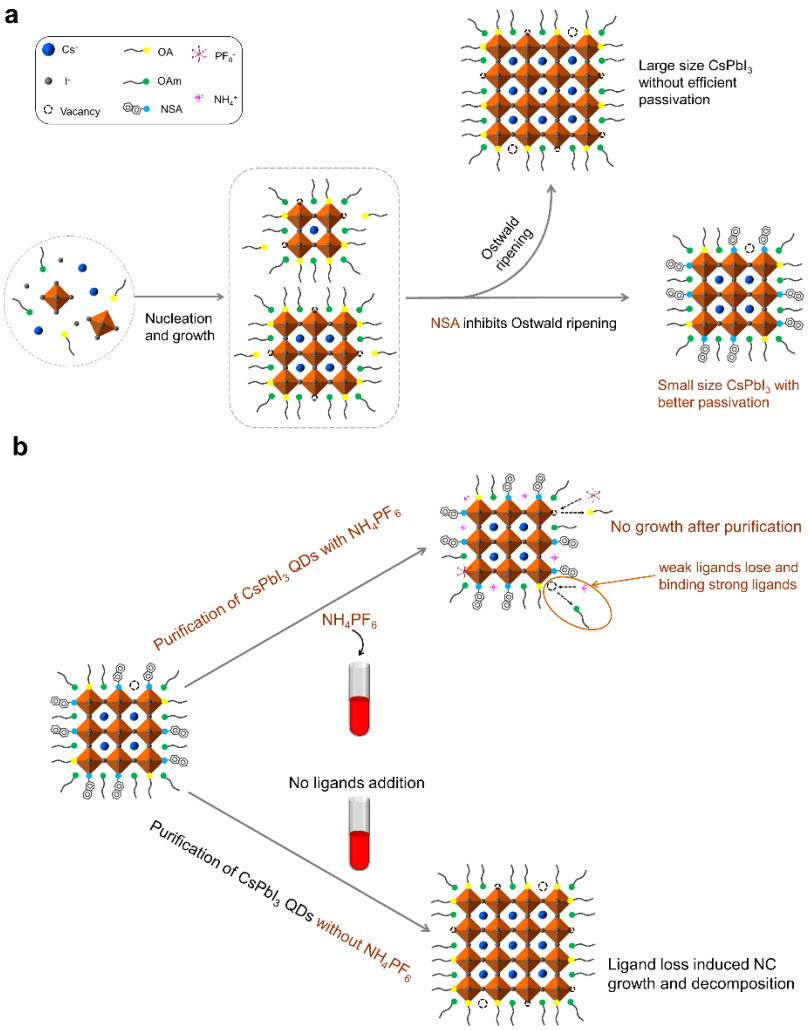

Figure 4.7 | (a) Schematical diagram of synthesising NSA-treated $CsPbI_3$ QDs (b) Schematical diagram of NH_4PF_6 treatment in the purification process.

The schematical diagram of synthesising NSA-treated $CsPbI_3$ QDs is shown in Figure 4.7a(Y. Li et al., 2024b). In the purification process of QDs, ammonium hexafluorophosphate (NH_4PF_6) is introduced to bind QD surfaces and passivate the defects strongly, avoiding deteriorating the stability and optical properties of QDs in the purification process (Figure 4.7b). Moreover, inorganic ligands can also improve the electrical conductivity of perovskite QDs. With the design of suppression overgrowth of QDs, monodispersed, strong-confined, and single-phase $CsPbI_3$ QDs are synthesised, which usually have an average particle size of 4~5 nm. The QDs have bright photoluminescence (PL) emission at 620~630 nm with an FWHM of 32 nm and PLQY over 90%. Pure red QLEDs were fabricated based on strong quantum confinement $CsPbI_3$ QDs. The champion device shows a maximum EQE of 26.04% for EL at 628 nm.

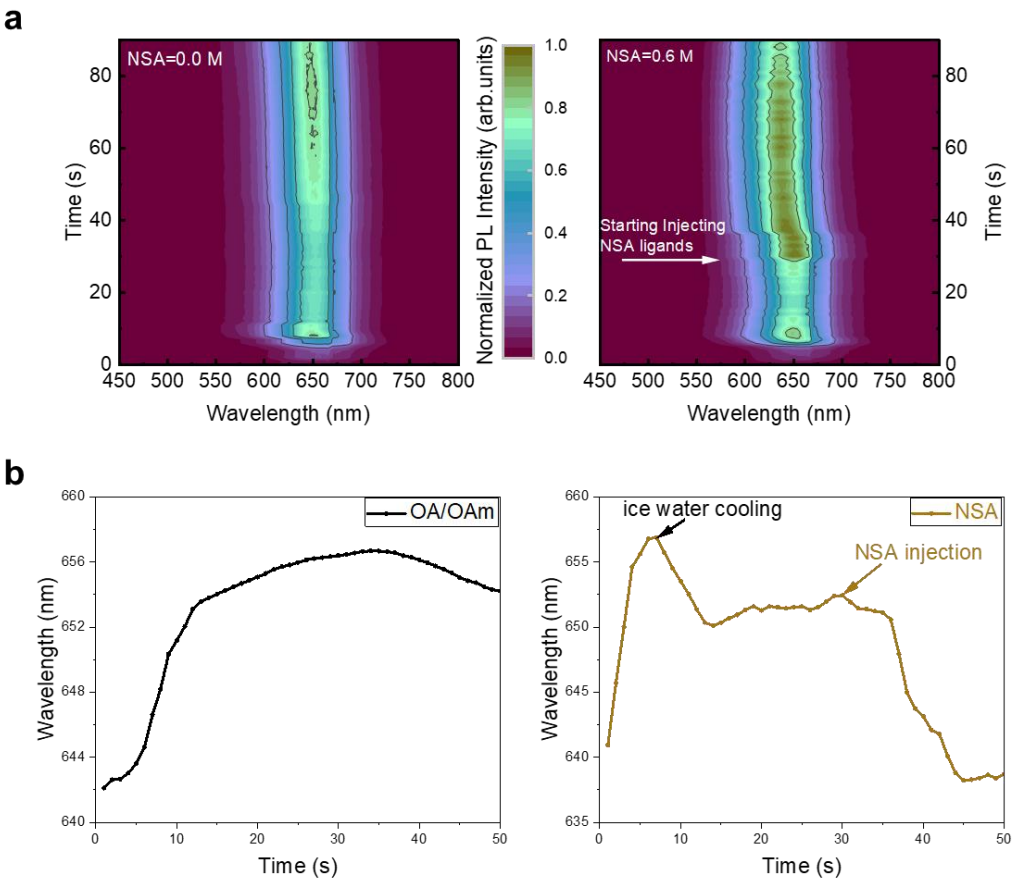

Figure 4.8 | (a) In-situ PL measurement of synthesised $CsPbI_3$ NCs with/without NSA addition (b) Extract PL wavelength evolution of $CsPbI_3$ NCs from in-situ PL

measurements.

Suppression Ostwald ripening with NSA ligands. In-situ PL spectroscopy is used to study the PL evolution of QDs nucleation and growth (Figure 4.8). The PL intensity of NSA-treated QDs is increased after adding NSA ligands. In addition, the PL wavelength of NSA-treated QDs blue shift after injecting NSA ligands. The wavelength evolution extracted from in-situ PL spectra is manifested in Figure 4.8b. After the injection of NSA ligand, compared with OA/OAm QDs (without NSA treatment), the blue shift of the PL spectrum and the enhancement of PL intensity of NSA-treated QDs indicate that the harmful ripening is inhibited, and the defects are passivated. Compared with OA, NSA has a higher dissociation constant and is more polar, which can be used to substitute weak acids. NSA can promote the proton process between OA/OAm(Grisorio et al., 2022). Thus, NSA can promote debonding surface OA/OAm ligands and etching defective octahedra.

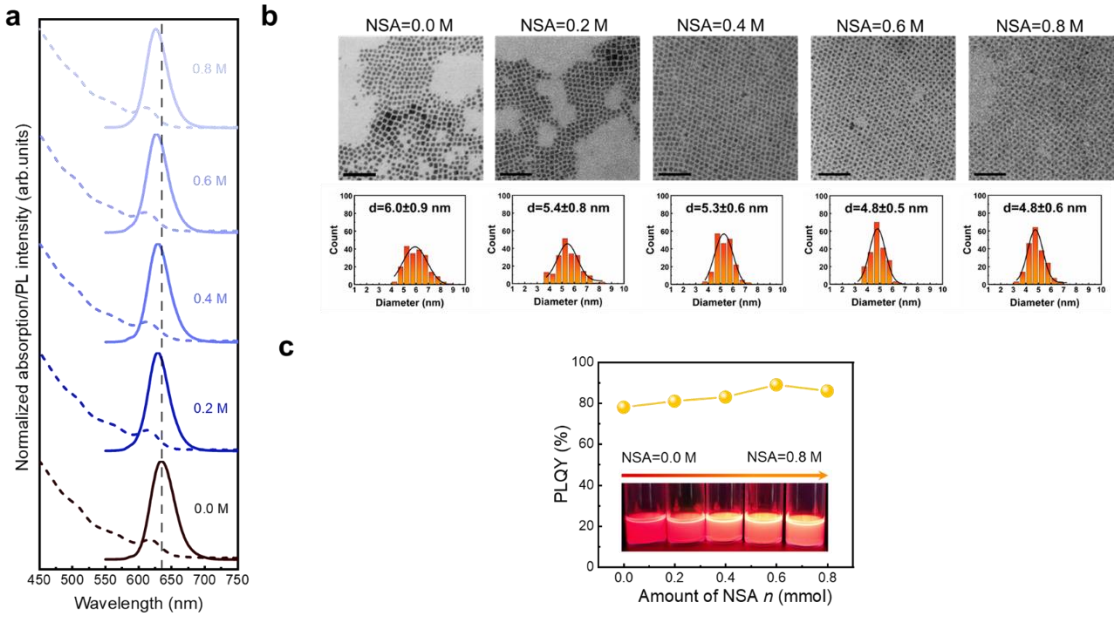

Figure 4.9 | Optical properties and morphology of synthesised PeNCs with different NSA ligands amounts. (a) Absorption and PL spectra of $CsPbI_3$ QDs synthesised with varying

amounts of NSA. (b) The TEM images (scale bar 50 nm) of $CsPbI_3$ QDs synthesised with different NSA amounts. (c) PLQY of $CsPbI_3$ QDs synthesised with different NSA amounts. Inset: Photos of $CsPbI_3$ QDs synthesised with different NSA amounts under UV light (365 nm).

Different amounts of NSA ligands (0, 0.2, 0.4, 0.6, 0.8 mmol) added after nucleation are studied to optimise the best concentration of NSA ligands. PL spectra of synthesised $CsPbI_3$ NC and TEM image are manifested in Figure 4.9. The calculated size distribution according to the TEM images is 6.0± 0.9, 5.4± 0.8, 5.3± 0.6, 4.8± 0.5, 4.8± 0.6 nm for different amounts of NSA ligands (0, 0.2, 0.4, 0.6, 0.8 mmol). With the increased amount of NSA addition, the size of NCs decreases, and size distribution is narrowed. The measured PLQY of synthesised NCs also increases with NSA addition. However, the optimised amount of NSA is 0.6 mmol as PLQY slightly decreases when excess NSA is added. The introduction of potent binding NSA ligands inhibits the ripening of QDs in the synthesis process. In addition, the optical properties of NCs are also improved with NSA ligands.

The DFT calculated that NSA's binding energy is 1.45 eV, a more substantial binding energy than OAm, which is only 1.23 eV, as Figure 4.6 exhibited. The stronger binding indicates that NSA can improve QD surface stability. The stronger binding of NSA is also demonstrated experimentally. The measured FTIR spectra (800 cm^{-1} to 1400 cm^{-1}) of synthesised $CsPbI_3$ NCs with or without NSA addition are shown in Figure 4.10a. The NSA-treated NCs have two peaks at 1030 cm^{-1} and 1090 cm^{-1}, respectively, which can be attributed to the stretching vibration of S-O- and S=O, respectively. The peak at 1260 cm^{-1} is a C-S stretching vibration. The XPS characterisation in Figure 4.10b shows that the binding energy of Pb 4*f* shifts to a higher level, indicating NSA has a stronger binding interaction with Pb atoms on the surface of QDs.

Works in Chapter 4 were published: Li, Y., Deng, M., Zhang, X., Qian, L., Xiang, C., 2024a. Nano-Micro Lett. 16, 1–10. Li, Y., Deng, M., Zhang, X., Xu, T., Wang, X., Yao, Z., Wang, Q., Qian, L., Xiang, C., 2024b. Nat. Commun. 15, 5696.

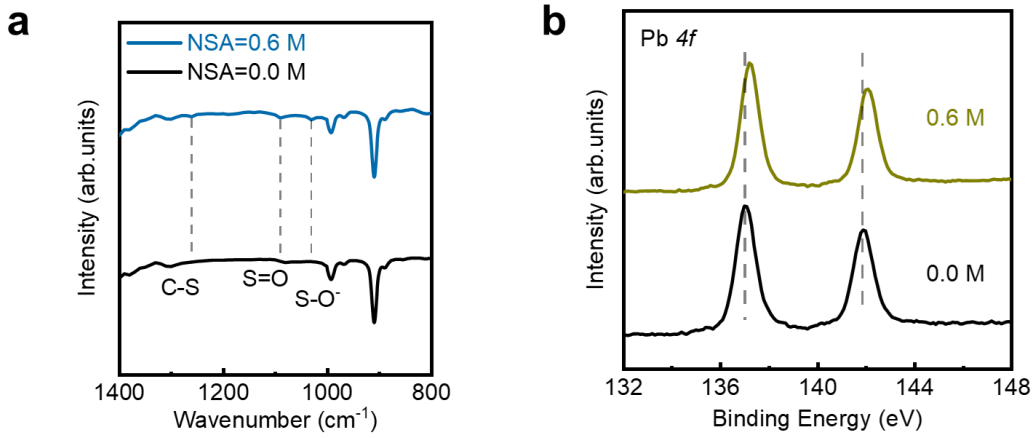

Figure 4.10 | (a) FTIR of synthesised $CsPbI_3$ QDs with or without NSA treatment (b) XPS Pb 4*f* spectra of synthesised $CsPbI_3$ QDs with or without NSA treatment.

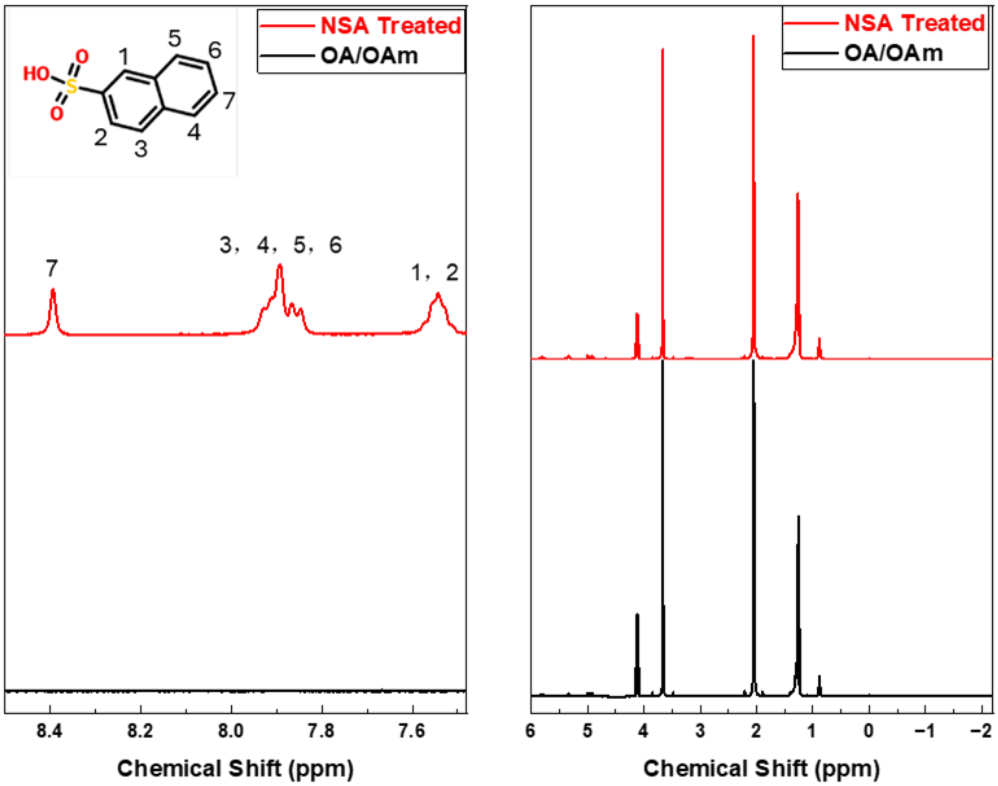

Figure 4.11| ^{1}H-NMR spectra of synthesised $CsPbI_3$ NCs with or without NSA treatment.

To further demonstrate the existence of NSA ligands on the QDs surface, ^{1}H-NMR spectra of NSA-treated QDs are measured and manifested in Figure 4.11. Those

characteristic peaks of NSA are in the range of 7.4 ppm to 8.5 ppm, and the corresponding hydrogen atoms are labelled. ^{1}H-NMR spectra of NSA-treated $CsPbI_3$ NCs exhibited characteristics of NSA, while OA/OAm NCs do not have peaks above 6 ppm. The result implies that NSA ligands are on the NSA-treated $CsPbI_3$ NCs surface.

Figures 4.12a and b are TEM images of merged $CsPbI_3$ NCs. The synthesised OA/OAm $CsPbI_3$ NCs produce a non-perovskite yellow phase and aggregate to a large size after being stored in the air for 3 days. From the enlarged picture, it is evident that large-size NCs are fused from small-size nanocrystals. The aggregation of small-size NCs is induced by ligands loss of weakly binding OA/OAm ligands, which is defects-driven. The NSA-treated $CsPbI_3$ NCs are stored in the air for 3 days and remain monodispersed (Figure 4.12c). The synthesised NC stability is enhanced by employing NSA ligands.

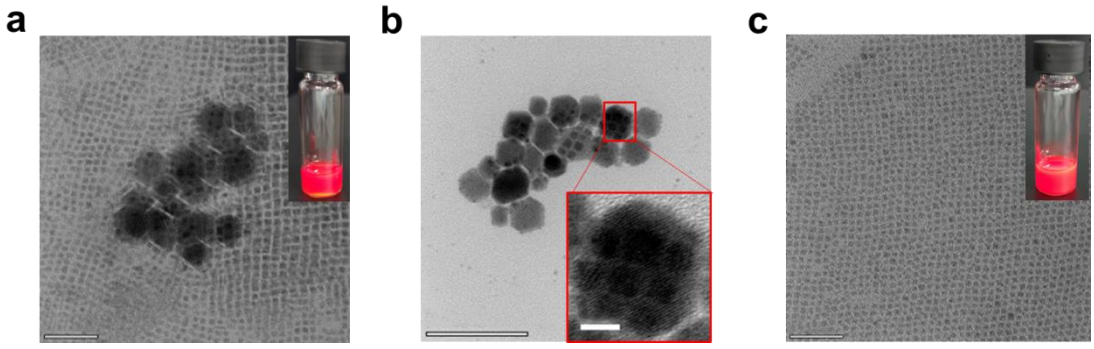

Figure 4.12| Storage Stability of QDs with or without NSA treatment. TEM images of $CsPbI_3$ QDs synthesised with different NSA amounts at ambient storage (temperature 25±5 °C, humidity 50±10%) for 3 days, the illustration is a photograph of the corresponding QDs in natural light, (a) NSA (0.0 mmol, scale bar 50 nm). (b) The TEM image of CsPbI3 QDs with NSA of 0.0 mmol (scale bar 100 nm); the QDs are fused into large-size nanocrystals, and the illustrations are high-resolution TEM images of nanocrystals (scale bar 10 nm). (c) NSA (0.6 mmol, scale bar 50 nm).

Passivation and growth suppression with NH_4PF_6 ligands. The synthesised NSA-treated $CsPbI_3$ NCs are further treated with NH_4PF_6 ligands in the purification process to

replace the residual weak ligands (OA/OAm). According to the DFT simulation, the binding energy of PF_6^- are 3.92 eV, which is much higher than the binding energy of OA/OAm (Figure 4.6). TEM, absorption, and PL spectra are used to characterise the morphology and photophysical properties of purified NCs in Figure 4.13. The NSA-NH_4PF_6 $CsPbI_3$ NCs have an emission peak at 623 nm with an FWHM of 32 nm, while OA/OAm $CsPbI_3$ NCs possess an emission wavelength of 639 nm with a broad FWHM over 40 nm. In addition, the NSA-NH_4PF_6 $CsPbI_3$ QDs show a much higher PLQY of 94%, indicating good surface passivation. As well known, inorganic salt ligands have relatively low steric hindrance compared to organic ligands, which is beneficial for deep defect passivation and the increment of surface ligand density. By partially replacing the organic ligands with inorganic salt, the charge transport ability of synthesised $CsPbI_3$ NCs can also be improved.

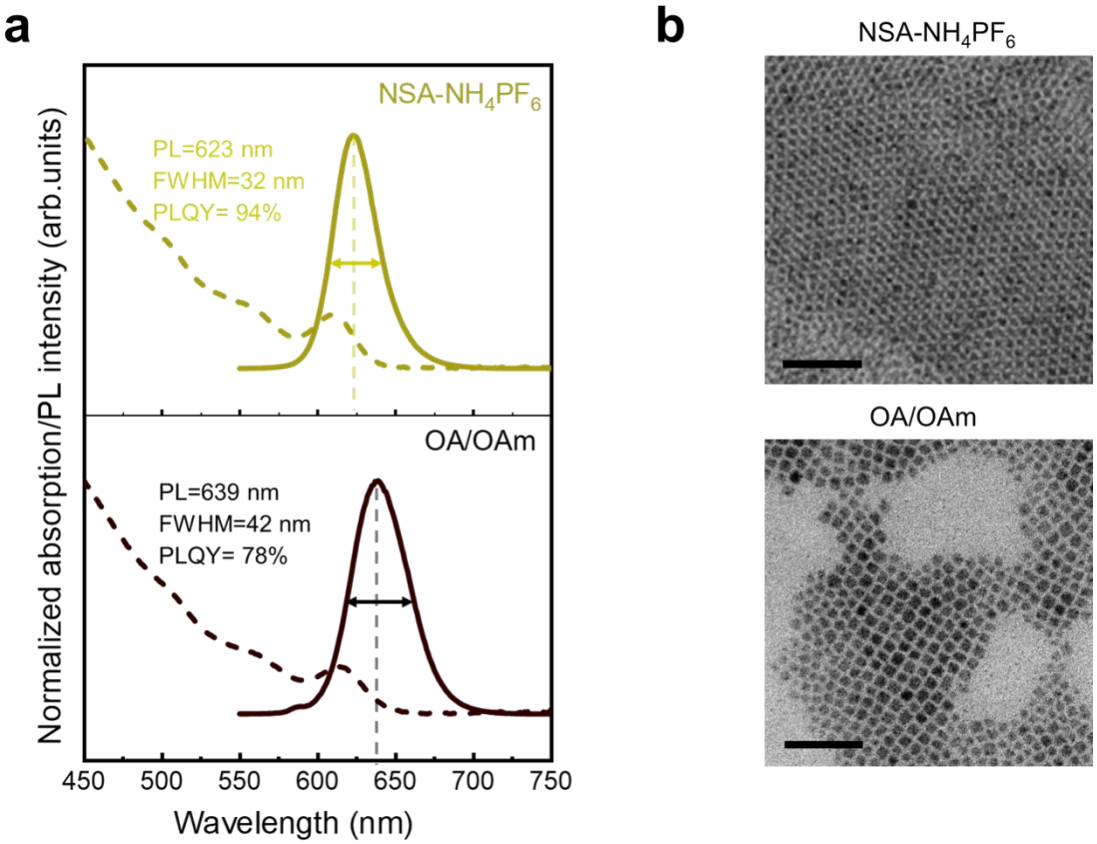

Figure 4.13 | (a) absorption and PL spectra of synthesised NSA-NH4PF6 $CsPbI_3$ NCs and

OA/OAm $CsPbI_3$ NCs (b) TEM images of NSA-NH4PF_6 $CsPbI_3$ QDs and OA/OAm $CsPbI_3$ QDs (scale bar 50 nm).

TEM images of $CsPbI_3$ QDs with OA/OAm and NSA-NH_4PF_6 are shown in Figure 4.13b. The NSA-NH_4PF_6 $CsPbI_3$ QDs show uniform shape and good size distribution. The corresponding statistic size distribution of synthesised NCs is manifested in Figure 4.14, from which the NSA-NH_4PF_6 QDs exhibit significantly smaller sizes and narrower size distribution than OA/OAm QDs. In the purification process, the polar solvent removes weak OA/OAm ligands and exposes the surface defects, inducing the regrowth and decomposition of small-size $CsPbI_3$ nanocrystals(Grisorio et al., 2022; Sun et al., 2018). For the NSA-NH_4PF_6 QDs, the potent ligands NH_4PF_6 immediately passivate the surface defects and replace the removed weak OA/OAm ligands, preventing nanocrystal regrowth and degradation.

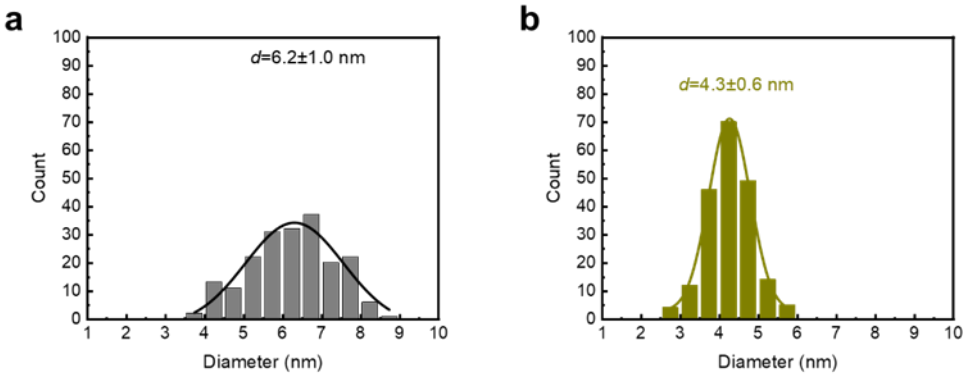

Figure 4.14 | Corresponding statistic size distribution of TEM images of NCs (a) OA/OAm QDs (b) NSA-NH_4PF_6 QDs.

TRPL decay spectra are shown in Figure 4.15a. The calculated average photoluminescence lifetime of NSA-NH_4PF_6 QDs film is 7.9 ns, while for OA/OAm QDs film, the average photoluminescence lifetime is 4.3 ns. The corresponding details of TRPL calculations are listed below in Table 4.1. The result indicates that non-radiative recombination of NSA-NH_4PF_6 QDs film is suppressed, and surface defects are reduced, which coincides with measured higher PLQY. The storage stability of the synthesised

$CsPbI_3$ QD solution is evaluated. Both OA/OAm and NH_4PF_6 QD solution are stored in the ambient environment (relative humidity 80%). As shown in Figure 4.15b, OA/OAm QDs suffer from decomposition and severe photoluminescence quenching, whose PLQY decreased to 0 after being stored for 25 days. In comparison, the PLQY of NSA-NH_4PF_6 QDs remained at 80% of the initial value after 50 days of storage. The enhanced stability is attributed to the strong binding of NH_4PF_6 ligands. The excellent photophysical properties and stability of QDs demonstrated the success of pure red $CsPbI_3$ QDs synthesis.

Table 4.1 | Fitting parameters of TRPL of synthesised $CsPbI_3$ NC films

	τ_1(ns)	τ_2(ns)	A_1	A_2	$\tau_{eff.}$(ns)
NSA-NH_4PF_6 QD film	7.96	14.456	0.9179	0.6396	7.9
OA/OAm QD film	2.62	6.28	0.4819	0.5524	4.3

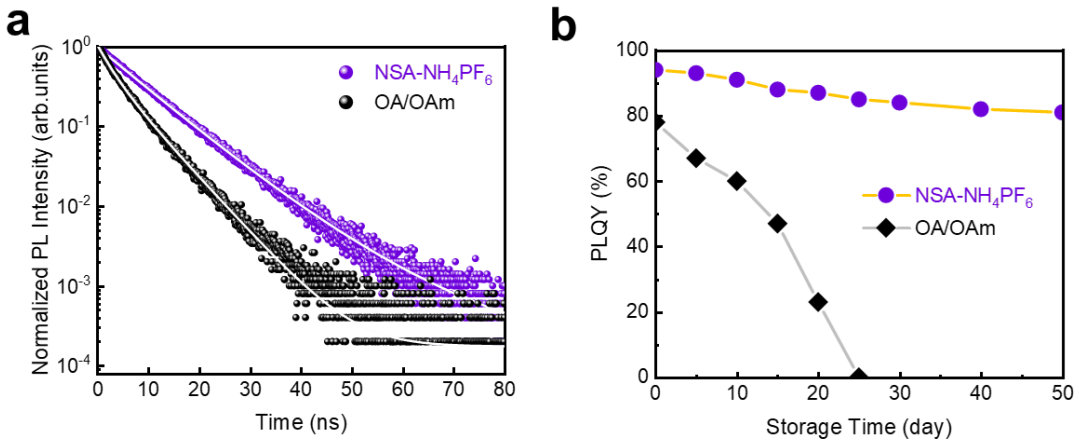

Figure 4.15 | (a) transient photoluminescence decay spectra of synthesised $CsPbI_3$ nanocrystals (b) storage stability of synthesised $CsPbI_3$ nanocrystal solution in the air (RH. 80%).

To experimentally demonstrate the strong binding of NSA and NH_4PF_6 ligands, we characterised the surface ligand states of NSA-NH_4PF_6 QDs and OA/OAm QDs. Figure 4.16a shows the results of FTIR. For OA/OAm QDs, peaks at 1750 cm^{-1} and 1573 cm^{-1}

are attributed to the stretching vibration of C=O and carboxylic acid groups of OA, respectively. Meanwhile, peaks at 1642 cm^{-1} and 908 cm^{-1} can be attributed to N-H bending vibration and C-N stretching vibration of OAm, respectively. After introducing the NSA and NH_4PF_6 ligands into the synthesis and purification process, there are two peaks at 1097 cm^{-1} and 1024 cm^{-1} for NSA-NH_4PF_6 QDs, which can be attributed to the stretching vibration of the sulfonyl group, while the peak at 803 cm^{-1} belongs to stretching vibration of the PF_6^- group. In addition, for NSA-NH_4PF_6 QDs, an N-H tensile signal corresponding to the cation (NH_4^+) was manifested, indicating that NH_4^+ of NH_4PF_6 binded on QD surfaces. Meanwhile, the intensity of the characteristic peak of OAm at 908 cm^{-1} (C-N) decreases significantly, indicating the successful replacement of OAm ligands. These results indicate that substantial weakly bounded OA/OAm ligands were replaced by NSA and NH_4PF_6 ligands in the synthesis and purification process of QDs. The designed ligands exchange on QD surfaces was efficient and successful.

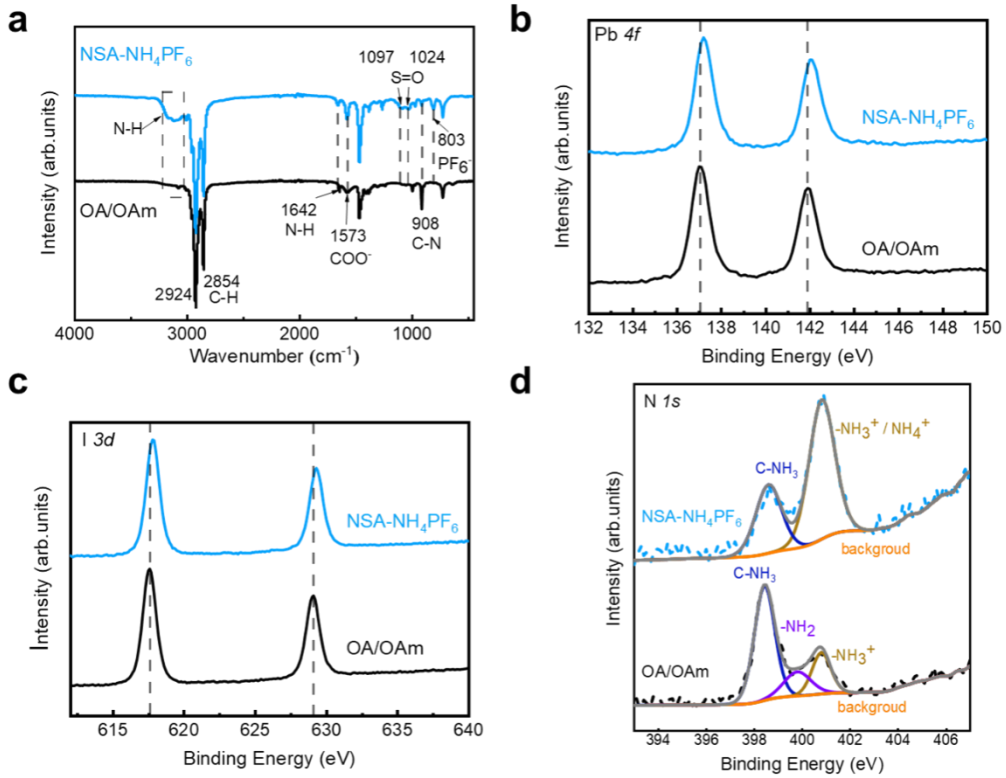

Figure 4.16 | (a) FTIR of OA/OAm and NSA-NH_4PF_6 QDs. XPS of (b) Pb 4*f*, (c) I 3*d*, and (d) N 1*s* of OA/OAm and NSA-NH_4PF_6 QDs.

The chemical states of the surface elements of $CsPbI_3$ QDs synthesised by different ligands are further characterised by XPS. The specific XPS spectra of Pb 4*f* and I 3*d* are

shown in Figures 4.16b and c, respectively. Compared to OA/OAm QDs, the binding energies of Pb 4*f* and I 3*d* of NSA-NH_4PF_6 QDs move to a higher level, which indicates that NSA and PF_6^- bind to Pb more strongly than OA. Furthermore, from the XPS spectrum of N 1*s* (Figure 4.16d) compared with OA/OAm QDs, the peak of C-NH_3, belonging to OAm, is weakened and the peak belonging to $-NH_3^+$ and NH_4^+ is enhanced after treatment with NSA and NH_4PF_6 ligands. In addition to the disappearance of the amine group ($-NH_2$) at 399.8 eV, I believe that NSA replaces OAm, and NH_4^+ replaces $OAmH^+$.

To further characterise surface ligands binding of synthesised NC, XPS F 1*s* spectra and TGA measurements are displayed. Figure 4.17 is XPS F 1*s* spectra of NH_4PF_6 and NSA-NH_4PF_6 QDs. Compared to NH_4PF_6, the XPS F 1*s* binding energy shifts to a low level, which indicates PF_6^- binding to Pb atoms. The measured TGA of QDs in 4.17b indicates that NSA-NH_4PF_6 QDs have a lower ligands weight ratio. However, NSA-NH_4PF_6 QDs have a smaller size of 4 nm, while OA/OAm QDs have a larger size of 6 nm. Usually, the smaller size means a larger surface area needs more ligands for passivation, which should have a higher ligand-weight ratio. Thus, the TGA result means many NH_4PF_6 and NSA ligands are bound on the surface, whose relative molecular mass is lower than OA or OAm.

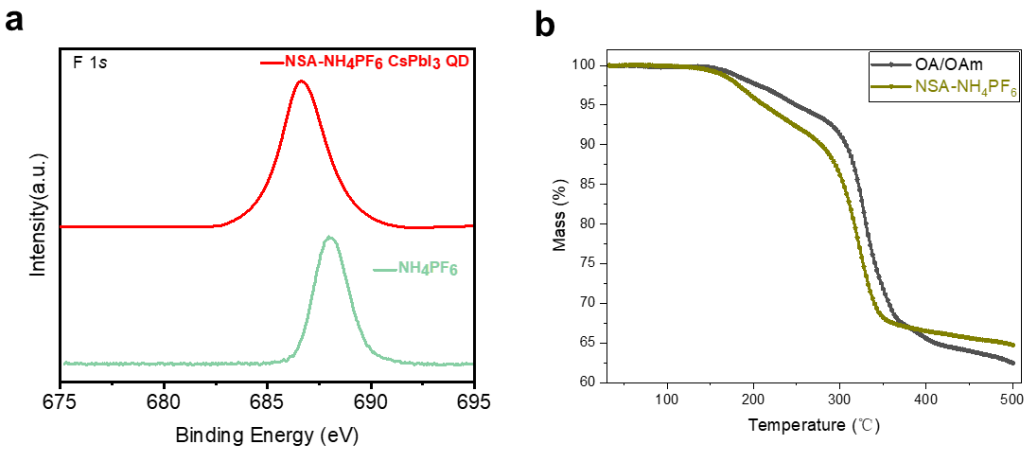

Figure 4.17 | (a) XPS of F 1*s* of NSA-NH_4PF_6 QDs and NH_4PF_6. (b) TGA curve of OA/OAm and NSA-NH_4PF_6 QDs.

4.4 Device performance

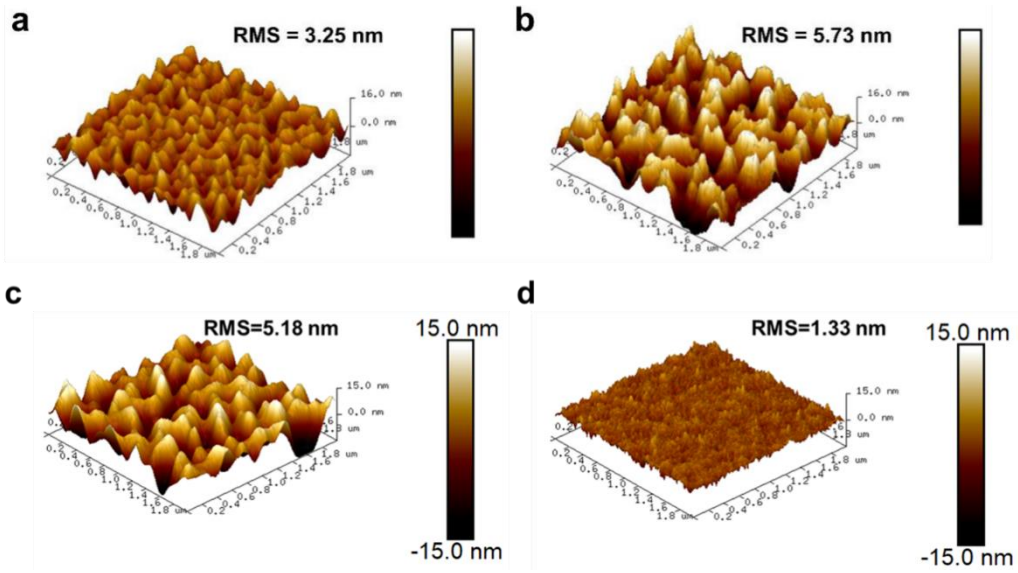

Figure 4.18 | AFM images of synthesised $CsPbI_3$ QDs (a) 5AVAI passivated QDs (645/38 nm), (b) OA/OAm QDs (650/42 nm), (c) ultra-small size OA/OAm QDs (639/42 nm), (d) NSA-NH_4PF_6 QDs (623/32 nm).

The synthesised $CsPbI_3$ QDs with different ligands were employed to fabricate QLEDs. Good film quality is essential to device performance. Charges accumulate on the bulge of films, causing charge imbalance in devices. Before device fabrication, the AFM of synthesised QD films is measured. As shown in Figures 4.18a and b, the root-mean-square (RMS) roughness of 5AVAI passivated $CsPbI_3$ QD film is 3.25 nm, while OA/OAm QD film (650/42 nm) has a rougher surface with an RMS of 5.73 nm. Figures 4.18c and d are AFM images of NSA-NH_4PF_6 and ultra-small size OA/OAm $CsPbI_3$ films, respectively. The RMS of NSA-NH_4PF_6 QD film is only 1.33 nm, while ultra-small size OA/OAm QD films have an RMS of 5.18 nm. The smooth film surfaces of 5AVAI and NSA-NH_4PF_6 QDs indicate better film quality. This might be explained by passivated PeNCs having a better hydrophobic surface shell, which is good wet on HTL.

Experiments are designed to verify whether the roughness of perovskite QD films is related to thickness or processing. The results are exhibited in Figure 4.19. For NSA-NH_4PF_6 QD films, the film roughness is almost the same for different QD concentrations or spin coating speeds. For OA/OAm QD films, when QD concentration increases, the roughness slightly decreases but still manifests a relatively rough surface compared to

NSA-NH_4PF_6 QD films. The roughness of OA/OAm film is also independent of the spin-coating speeds. The result demonstrates that roughness is irrelevant to film thickness or processing. Agglomerations of perovskite QDs are induced by ligand loss or surface defects.

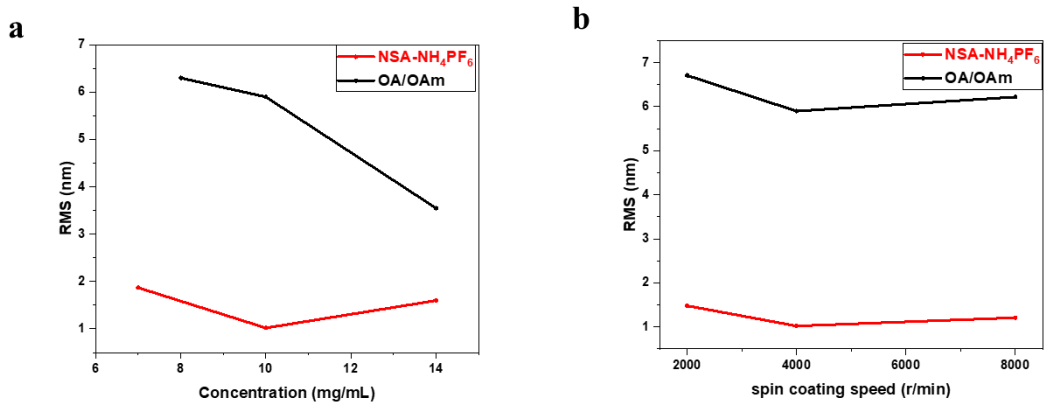

Figure 4.19 | (a) different concentrations of NSA-NH_4PF_6 and OA/OAm QDs film roughness, spin-coating speed at 4000 r min^{-1}. (b) different spin-coating speeds of NSA-NH_4PF_6 and OA/OAm QDs film roughness, QD concentration is 10 mg mL^{-1}.

Figure 4.20a exhibits the structure and various layer thicknesses of QLEDs. The structure is ITO/PEDOT: PSS/PTAA/$CsPbI_3$ QDs/TmPyPB/PO-T2T/LiF/Al. The thicknesses are measured using the TEM image manifested in Figure 4.20b. The sample is prepared by a focus ion beam (FIB). The thickness of QD film is only 8.77 nm, which is about two QD layers. The ultrathin QD films are beneficial for charge transport and decrease charge accumulation. The overall thickness of ETL is 45.96 nm, while the overall thickness of HTL is 41.40 nm.

The EQE limit of the fabricated devices is explored by simulation using the Setfos 5.4 software. Figure 4.20c is the measured refractive index of NSA-NH_4PF_6 $CsPbI_3$ QD films using an ellipsometer. The device structure, as depicted in Figure 4.20d, served as the base for simulations. Consequently, the EQE limitation of the QLEDs is 29%. The relationship of EQE limitation between different layer thicknesses is investigated. For more information, please visit the supplementary information of the published work(Y. Li et al., 2024b).

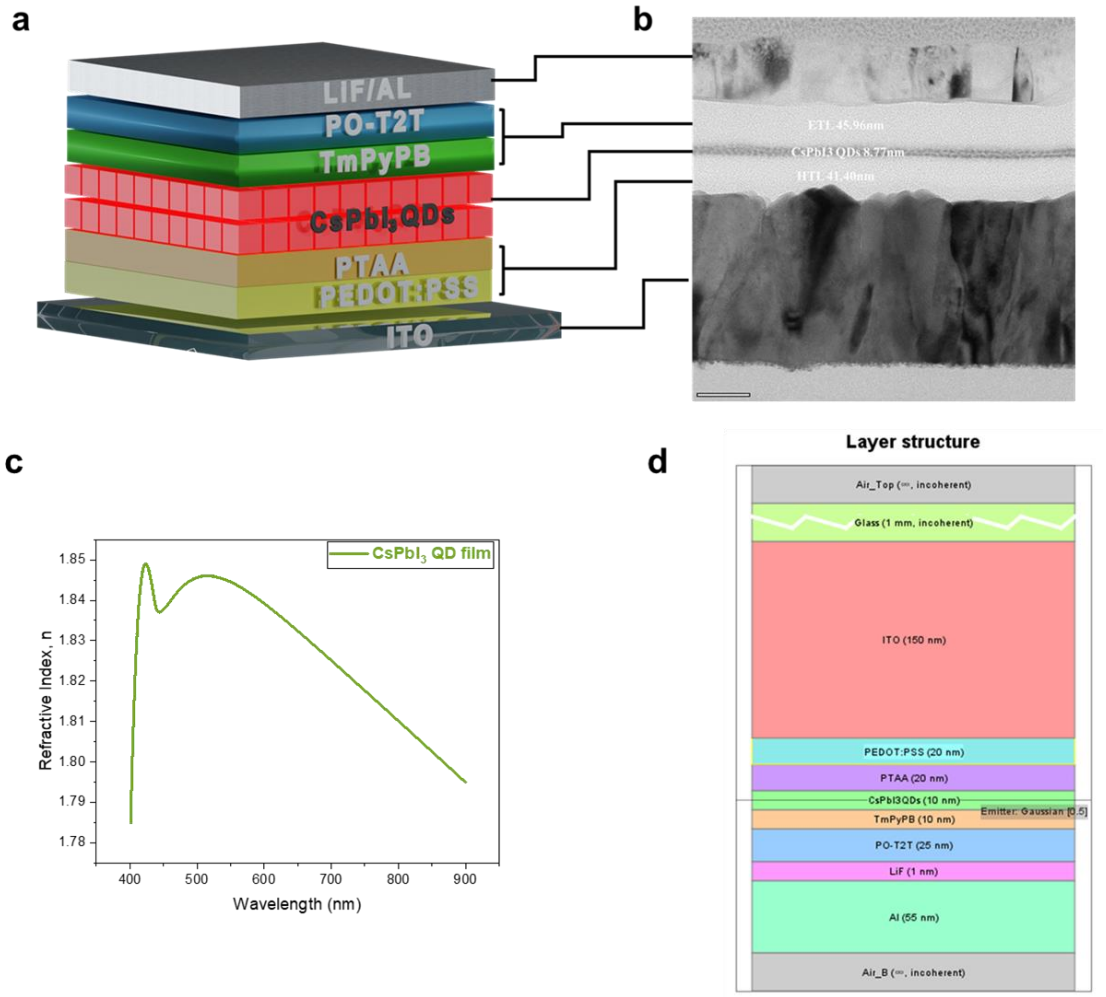

Figure 4.20 | Device structure and simulation of $CsPbI_3$ QLEDs. (a) $CsPbI_3$ QLEDs device structure diagram. (b) Cross-sectional TEM images (scale bar 50 nm) of LEDs based on NSA-NH_4PF_6 $CsPbI_3$ QDs. (c) Ellipsometry measurement of a synthesised NSA-NH_4PF_6 $CsPbI_3$ QD film. (d) Device structure used for simulation of optical waveguide mode distribution.

The NC bandgap is calculated by Tauc plots in Figures 4.21a and b. The bandgap of OA/OAm NCs is 1.940 eV and 1.974 eV for NSA-NH_4PF_6 QDs. The valance band energy level and fermi level of QDs are calculated using the UPS in Figure 4.21c. The energies from the fermi energy level to the vacuum level are 3.62 and 3.60 eV for OA/OAm and NH_4PF_6 QDs, respectively. For OA/OAm QDs, the fermi energy to valance band energy level is 1.70 eV. For NSA-NH_4PF_6 QD, the value is 1.62 eV. Therefore, the calculated valence band energy level of OA/OAm NC is -5.32 eV, while for NSA-NH_4PF_6 QDs, the valence band energy level is -5.22 eV. The conduction band energy levels of NCs can be

calculated, which is -3.38 eV for OA/OAm QDs and -3.24 eV for NH_4PF_6 QDs. Bandgaps and energy levels of 5AVAI passivated NC films are also computed using Tauc plots and UPS measurements.

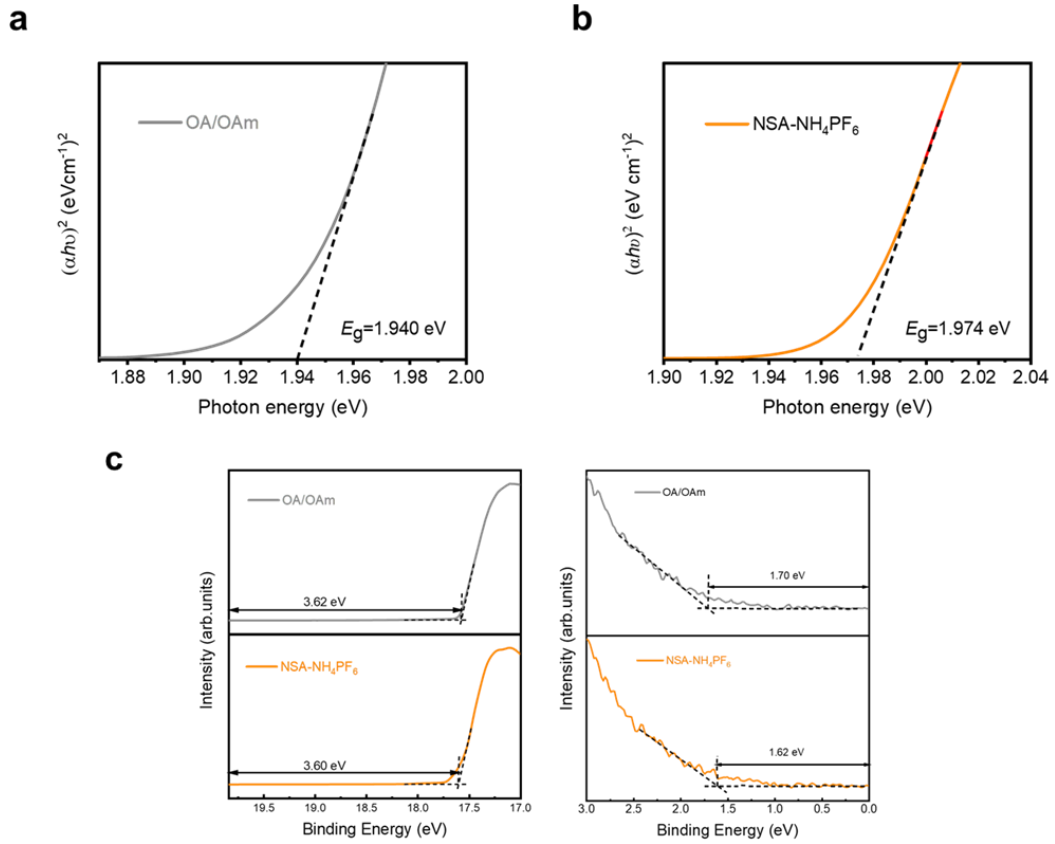

Figure 4.21 | Tauc plots of $CsPbI_3$ QD films treated with different ligands, (a) oleci OA/OAm QDs, (b) NSA-NH_4PF_6 QDs. Measured energy levels of different QD films, (c) UPS of OA/OAm and NSA-NH_4PF_6 QD film.

According to the calculated band energy levels of QDs, the device band energy diagram can be drawn as shown in Figure 4.22a. The QLEDs fabricated with NSA-NH_4PF_6 $CsPbI_3$ QDs show EL emission at 628 nm with an FWHM of 33 nm (Figure 4.22b), whose CIE coordinate is pure red (0.691, 0.308) as shown in Figure 4.22c. The stability of EL spectra of QLEDs based on NSA-NH_4PF_6 QDs is demonstrated by applying different voltages, as shown in Figure 4.22d. The devices based on 5AVAI QDs have EL emission at 645 nm. The corresponding OA/OAm counterpart shows EL emission at 651 nm.

Works in Chapter 4 were published: Li, Y., Deng, M., Zhang, X., Qian, L., Xiang, C., 2024a. Nano-Micro Lett. 16, 1–10. Li, Y., Deng, M., Zhang, X., Xu, T., Wang, X., Yao, Z., Wang, Q., Qian, L., Xiang, C., 2024b. Nat. Commun. 15, 5696.

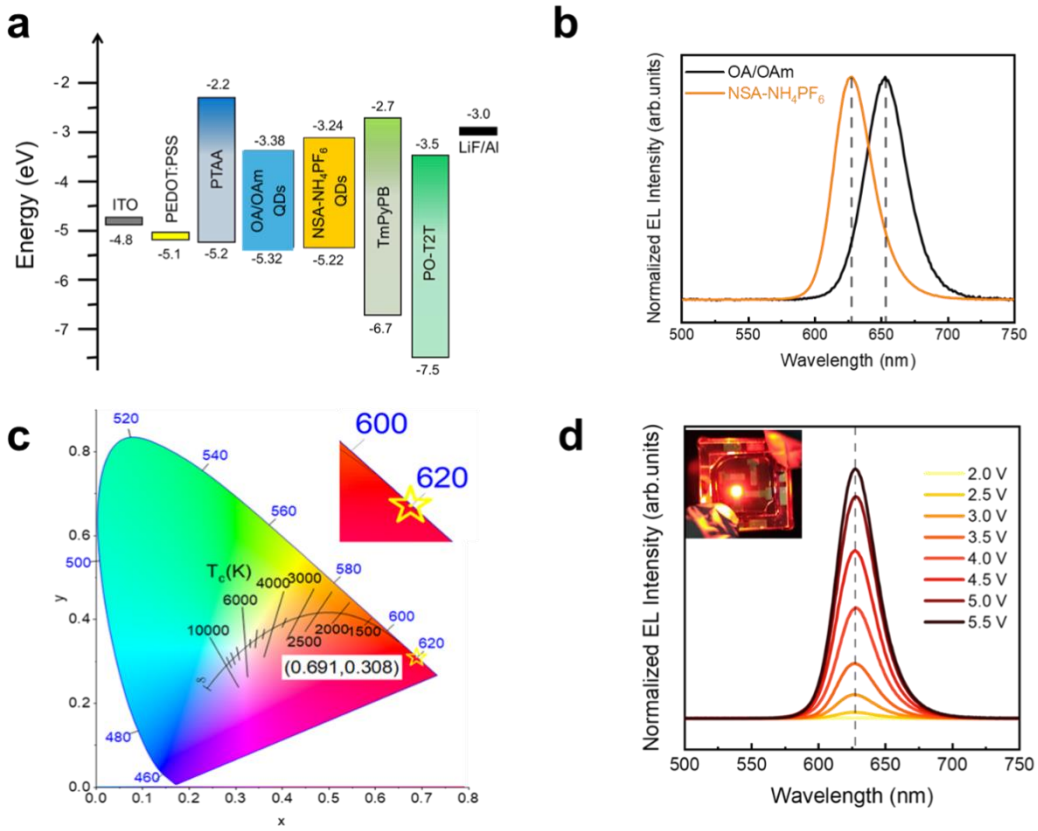

Figure 4.22 | (a) The energy level diagram of fabricated QLEDs. (b) The normalised EL spectra of QLEDs. (c) The emission chromaticity diagram of fabricated NSA-NH_4PF_6 $CsPbI_3$ QLEDs. (d) EL spectra of NSA-NH_4PF_6 $CsPbI_3$ QLEDs under different voltage biases.

Figure 4.23a is the current density (*J*)-voltage (*V*) luminance (*L*) curves of the champion QLED devices. The QELDs based on NSA-NH_4PF_6 QDs achieved a sub-bandgap turn-on voltage which is 1.8 V. Compared with OA/OAm QDs-based QELD, the NSA-NH_4PF_6 QDs-based QLED has a higher current density, which indicates better conductivity of NSA-NH_4PF_6 NCs. As mentioned above, this is because of the replacement of long-chain organic ligands by inorganic ligand NH_4PF_6, which improved the carrier transport ability of QDs.

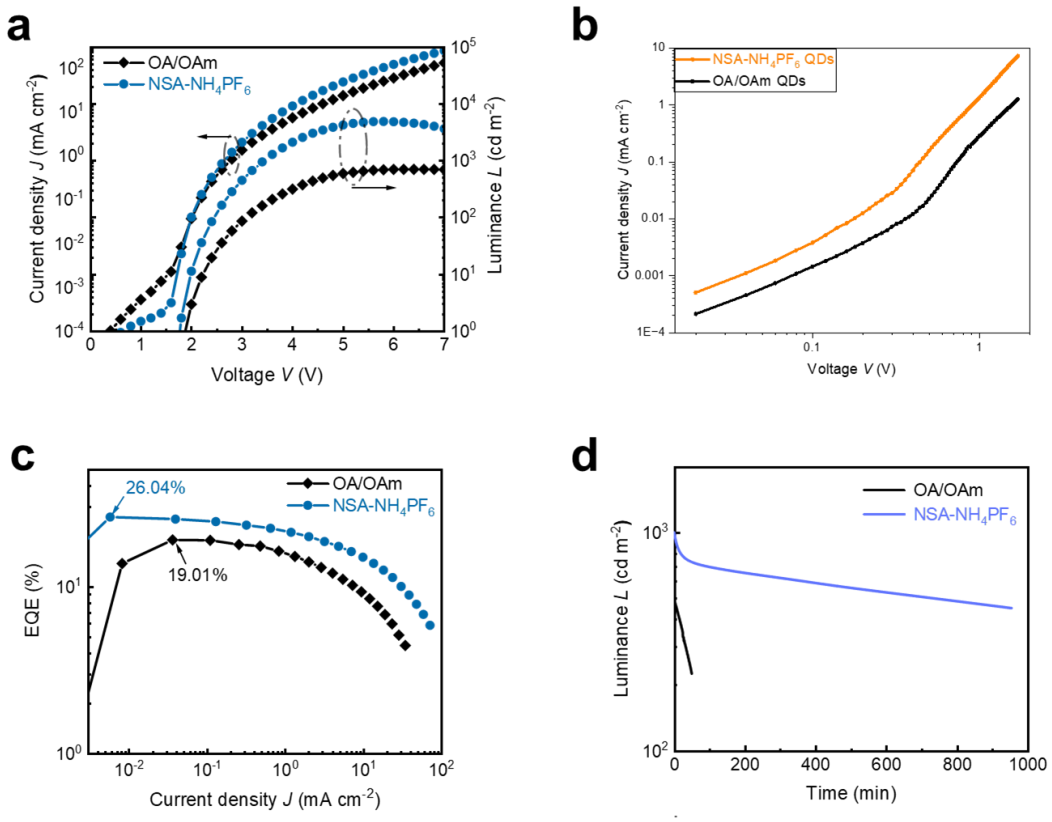

Figure 4.23 | (a) *J-V-L* curves of fabricated QLEDs. (b) *J-V* curve of the electron-only device for NSA-NH_4PF_6 and OA/OAm QDs. (c) EQE curves of fabricated QLEDs. (d) Operational stability of QLEDs.

The good conductivity of NSA-NH_4PF_6 NCs is further proved, as shown in Figure 4.23b. The electron-only device based on NSA-NH_4PF_6 NCs has a higher current density at the same voltage bias. In addition, the upshift of valance band energy levels of NH_4PF_6 QDs decreased the hole injection barrier of devices. As a result, in Figure 4.23c, the champion device of NSA-NH_4PF_6 QDs-based QLEDs possesses maximum luminance at 5.8 V, which is 4203 cd·m^{-2} with a peak EQE of 26.04%, while the peak EQE of champion OA/OAm QLED is 19.01% with a maximum luminance of the of 696 cd·m^{-2}. The operational stability of QLEDs is evaluated as shown in Figure 4.23d. For champion devices prepared by NSA-NH_4PF_6 $CsPbI_3$ QDs, half-lifetime (T_{50}, defined as the time when the brightness drops to half of the initial brightness is 729 mins at the initial brightness of 1000 cd·m^{-2}, while T_{50} of champion devices based on OA/OAm $CsPbI_3$ QDs

is about 43 min (L_0= 500 cd·m^{-2}). The QLEDs based on 5AVAI QDs achieve a peak EQE of 24.45%, while its OA/OAm court part has a peak EQE of 18.63%.

The average EQE of 25 devices for OA/OAm QDs and NH_4PF_6 QDs is 16.89% and 24.00%, respectively, which exhibits excellent reproducibility (Figure 4.24a). Moreover, the QD synthesis also presents good reproducibility, as shown in Figure 4.24b. Through this strategy, the efficient pure red emission of QLEDs based on $CsPbI_3$ QDs is realised, representing pure red PeLEDs' best performance (Supplementary Information Table A1-2).

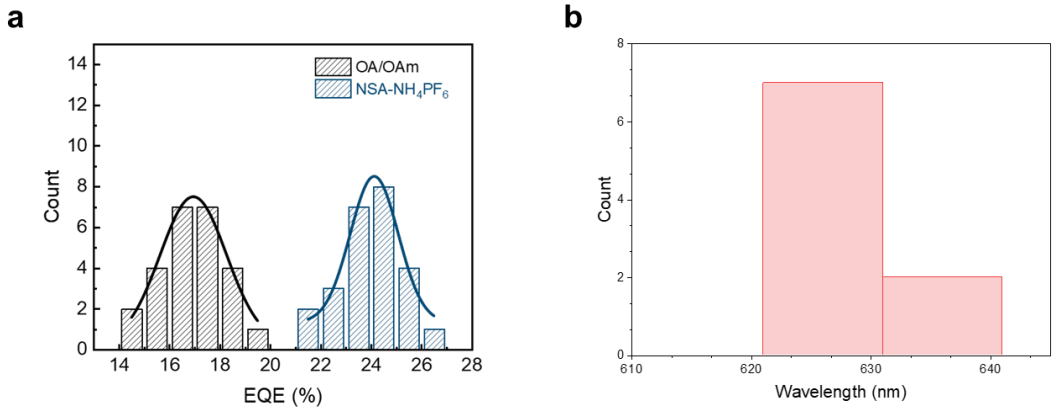

Figure 4.24 | (a) Average peak EQE of 25 fabricated QLEDs. (b) The emission wavelength of 9 batch synthesis of QDs.

4.5 Summary

In this chapter, stable small-size $CsPbI_3$ QDs are synthesised. 5AVAI is a similar resurfacing agent to C_3-S-HBr. 5AVAI passivates defects on small-size $CsPbI_3$ QDs surface and enhances the environment stability. Weak OA/OAm are exchanged. The 5AVAI passivated QDs manifest PLQY over 90% with good storage ability. The device performance is significantly improved compared to OA/OAm $CsPbI_3$ QDs. The 5AVAI passivated NCs achieved a maximum EQE of 24.45% at 645 nm with an FWHM of 38 nm.

In addition, stable pure-red $CsPbI_3$ QDs are synthesised by regulating the growth of QDs. The spontaneous growth led by the defective surface is prohibited with NSA ligands.

Works in Chapter 4 were published: Li, Y., Deng, M., Zhang, X., Qian, L., Xiang, C., 2024a. Nano-Micro Lett. 16, 1–10. Li, Y., Deng, M., Zhang, X., Xu, T., Wang, X., Yao, Z., Wang, Q., Qian, L., Xiang, C., 2024b. Nat. Commun. 15, 5696.

Overgrowth during purification is also prohibited by using potent binding NH_4PF_6 ligands. The average size of NSA-NH_4PF_6 $CsPbI_3$ QDs is 4.3 nm. The PL spectra show an emission wavelength of 623 nm with an FWHM of 32 nm. PLQY of NSA-NH_4PF_6 $CsPbI_3$ QDs reaches 94%. PeQLEDs based on NSA-NH_4PF_6 $CsPbI_3$ QDs achieve a peak EQE of 26.04% at 628 nm. The measured operation lifetime is T_{50} of 23053 minutes at 100 $cd \cdot m^{-2}$. These devices exhibit efficient pure red emission, representing the highest efficiency of pure red PeQLED.

Works in Chapter 4 were published: Li, Y., Deng, M., Zhang, X., Qian, L., Xiang, C., 2024a. Nano-Micro Lett. 16, 1–10. Li, Y., Deng, M., Zhang, X., Xu, T., Wang, X., Yao, Z., Wang, Q., Qian, L., Xiang, C., 2024b. Nat. Commun. 15, 5696.

Chapter 5. Light-emitting Diodes Structure Design

5.1 Background

PeQLEDs are currently considered promising candidates for displays(Bi et al., 2023; Rainò et al., 2022; Wan et al., 2023; Wang et al., 2020b). PeQELDs have achieved high efficiency in recent years, with EQE of 29.4% for green(Zhang et al., 2024), 18% for blue (480 nm)(Jiang et al., 2022), and 28.5% for red (644 nm)(H. Li et al., 2024). However, the low operation lifetime prohibits commercial applications of PeQLEDs(Han et al., 2022). The commonly used PeQELDs structure (Figure 5.1a) suffers from low charge mobility and instability of the transport layer(Yang et al., 2022). In addition, the interface between perovskite QD films and transport layers induces exciton quenching. The charge balance of PeQLEDs is not good as the perovskite QD film is usually an n-type semiconductor. The device charge imbalance leads to charge accumulation, increasing non-radiative Auger recombination. Charge accumulation also induces ligand loss of QD films, resulting in EQE decrease of QLEDs. The PeQLEDs produce lots of joule heat when operating at the high current density, increasing temperatures (Sun et al., 2023; Yang et al., 2022; Zhao et al., 2020).

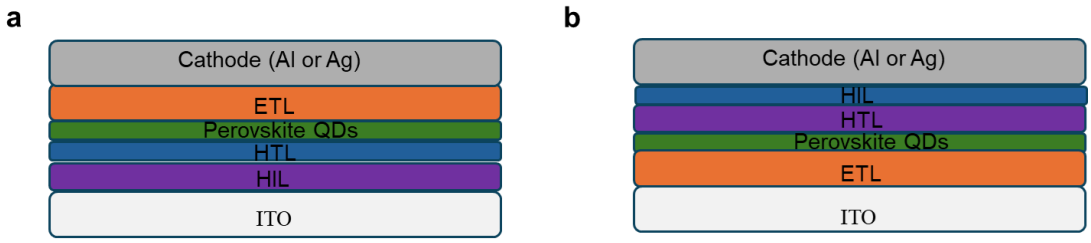

Figure 5.1 | (a) Normal PeQLED structure, (b) Inverted PeQLED structure.

To solve those problems, some strategies for improving the performance of traditional QLEDs merit attention, such as inserting interface layers(Dai et al., 2014), double ETL(Chen and Chen, 2022; Ye et al., 2022), thin QD films(Gao et al., 2023), and

inorganic ETL with an inverted device structure (Figure 5.1b)(Lim et al., 2018). Organic transport layers with high charge mobility, such as PTAA, PO-T2T, and TmPyPB, are used. However, the energy level of PO-T2T does not match perovskite QD well and causes a relatively significant electron injection barrier. In addition, PO-T2T induces perovskite NC film fluorescence quenching(Fang et al., 2021). Buffer layers, such as TPBi and TmPyPB, are introduced here to solve the problem(Deng et al., 2024b; Fang et al., 2021). The device charge balance can also be controlled by adjusting the thickness of various layers. In addition, for OTAc/OTAm $CsPbBr_3$ QDs passivated with C_3-S-HBr, organic polymer layers are inserted into the QLEDs to relieve fluorescence quenching. The fabricated red $CsPbI_3$ QDs device structure uses ultra-thin QD film to reduce joule heat.

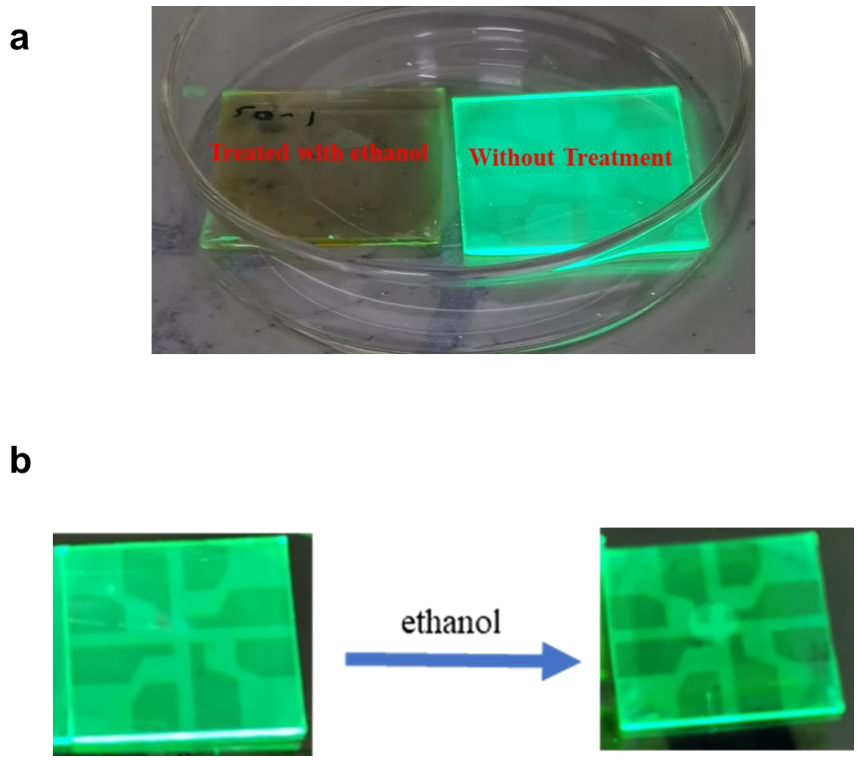

Figure 5.2 | Perovskite NC films treated with ethanol by spin coating (a) OA/OAm NCs, (b) C3-S-HBr passivated DEHPA NCs.

Perovskite QD films cannot resist polar solvents in the device fabrication process. The perovskite QD films are peeled off or quenched by ethanol (Figure 5.2). ZnO with

nonpolar solvents can induce the destruction and redissolution of the underlying perovskite film. In addition, the annealing temperatures for ZnO nanoparticles are limited to the high-temperature tolerance of perovskite films. Therefore, inverted PeQLED structures are designed to use ZnMgO as ETL. Inverted structures have many advantages here(Kwak et al., 2012; Mashford et al., 2013). As ZnO nanoparticles are the first layer for spin-coating, they can be annealed at relatively high temperatures regardless of perovskite films. Besides, the bottom cathode directly connects to the n-type metal oxide or an active-matrix panel-based n-type thin-film transistor (TFT), reducing the pixels driving voltage and improving the device stability(Liu et al., 2018).

5.2 Polymer Interface Layers for Green PeQELDs

Double ETL structures (green: TPBi/PO-T2T; red: TmPyPB/PO-T2T) have achieved high-performance green PeQLEDs. Herein, the device structure of both red and green devices uses this structure for high-performance devices. According to studies, PO-T2T causes fluorescence quenching to perovskite QD films and device energy levels mismatch. To solve this problem, an interface layer is inserted to relieve fluorescence quenching and work as an electron injection layer. For green devices, TPBi is used, while TmPyPB is used for red(Deng et al., 2024a).

The hole transport layer, PTAA, is observed to cause fluorescence quenching to C_3-S-HBr passivated OTAc/OTAm $CsPbBr_3$ NC films. PO-T2T is a molecular with P=O function groups, which is Lewis base. As a result, the strong basicity induces the formation of defects and surface traps in QDs (Morad et al., 2024). Inspired by the double ETL structure design, two polymers, poly(methylmethacrylate) (PMMA) and poly (vinyl pyrrolidone) (PVP), are used as the hole interface buffer layers for devices based on C_3-S-HBr passivated OTAc/OTAm $CsPbBr_3$ NCs. The effects of the two polymers are explored. Figure 5.3a shows the absorption and PL spectra of synthesised QDs(Wang et al., 2023). Figure 5.3b measures the relative PL intensity of perovskite film on different substrates. The perovskite film has the highest intensity on the PMMA substrate. As shown in Figure 5.3c, the PLQY of perovskite QD solution significantly decreases after

Works in Chapter 5 were published: Shen, P., Zhang, X., Wu, R., Zhang, T., Qian, L., Xu, W., Kang, K., Zhao, D., Xiang, C., 2023. ACS Appl. Mater. Interfaces. Wang, Q., Zhang, X., Qian, L., Xiang, C., 2023. ACS Appl. Mater. Interfaces 15, 28833–28839.

forming films on the PTAA substrate due to the formation of nonradiative recombination centres. The perovskite film PLQY is only 44.23% with PTAA substrate. The fluorescence quenching is relieved on the PVP substrate. In contrast, films on the PMMA substrate obtain PLQY of 72.44%.

Exciton dynamics are investigated using TRPL spectra (Figure 5.3d). The TRPL spectra of perovskite QD films on different substrates indicate that films on the PMMA substrate have longer average exciton lifetimes. The fitted average exciton lifetimes of PTAA/QD, PVP/QD, and PMMA/QD are 6.22, 7.86, and 9.93 ns. This can be attributed to the reduced interface trap density of the PMMA/QD interface compared to the PTAA/QD interface. The carbonyl group in PMMA and PVP can combine with uncoordinated Pb^{2+} ions, passivating the perovskite interface.

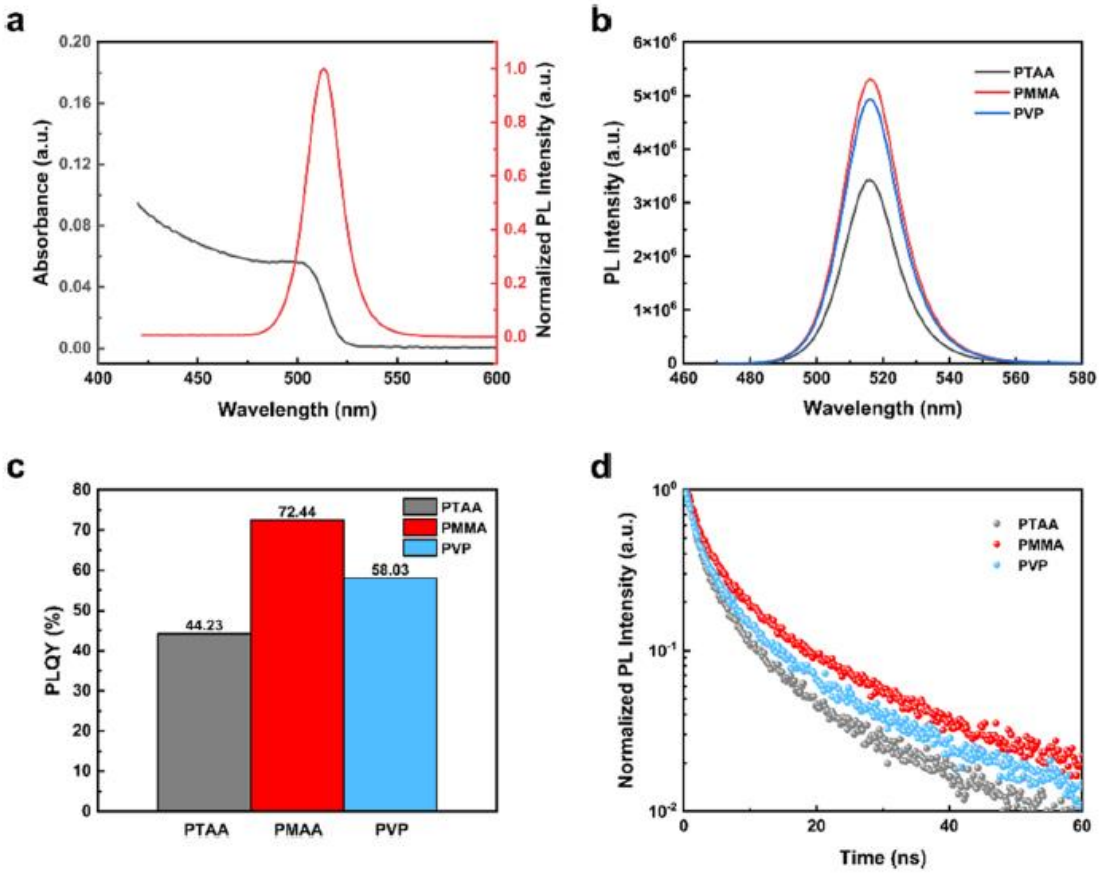

Figure 5.3 | (a) Absorption and PL spectra of C_3-S-HBr passivated OTAc/OTAm $CsPbBr_3$ NCs. C_3-S-HBr passivated OTAc/OTAm $CsPbBr_3$ NC film (b) PL intensity, (c) PLQY, (d) TRPL on different substrates.

Works in Chapter 5 were published: Shen, P., Zhang, X., Wu, R., Zhang, T., Qian, L., Xu, W., Kang, K., Zhao, D., Xiang, C., 2023. ACS Appl. Mater. Interfaces. Wang, Q., Zhang, X., Qian, L., Xiang, C., 2023. ACS Appl. Mater. Interfaces 15, 28833–28839.

The defect density is evaluated using the SCLC method. The fabricated hole-only device structure is ITO/PEDOT: PSS/PTAA/perovskite films/TAPC/Ag. The current density (J) versus voltage (V) curves are shown in Figure 5.4a(Wang et al., 2023). The trap states in devices are filled when the applied voltage exceeds the trap-filling limit voltage (V_{TFL}). The V_{TFL} of the PTAA device is 0.82 V. With the polymer buffer layers, the V_{TFL} significantly decreases. V_{TFL} of the PMMA and PVP devices is 0.45 and 0.66 V, respectively. The trap density is calculated by following the equation. The details of the SCLC method are described in the methodology chapter.

$$N_t = \frac{2\varepsilon\varepsilon_0 V_{TFL}}{ed^2} \tag{5.1}$$

Therefore, the calculated defect density of the PTAA/QD films is 3.27×10^{17} cm^{-3}, while the defect density of the QD films inserting PMMA and PVP as buffer layers is 1.83×10^{17} and 2.65×10^{17} cm^{-3}, respectively. The calculated defect density of QDs with buffer layers is significantly lower than PTAA/QD film. High defect density leads to charge accumulation in devices, impeding the operational stability of perovskite QLED devices. The SEM image of the cross-section of the single-carrier device is shown in Figure 6.4b. The QD layer thickness is around 250 nm to ensure an accurate evaluation of defect density. It is worth noting that the thickness of the hole interface buffer layer (2 to 3nm) and MoO_3 layer (10nm) is much thinner than other layers and not marked here.

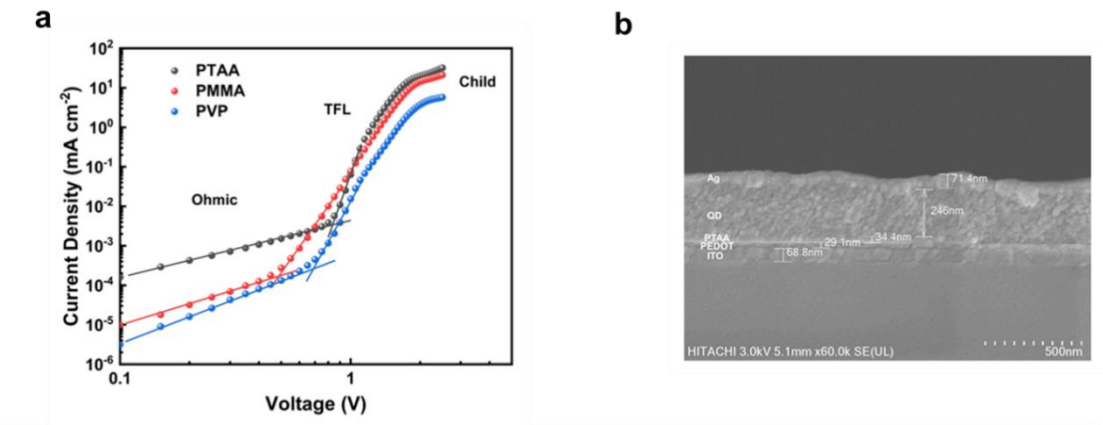

Figure 5.4 | (a) J-V curves of hole-only devices with different perovskite film substrates,

(b) Cross-section TEM image of fabricated green PeQLEDs.

5.3 Inverted Device Structure with ZnMgO ETL

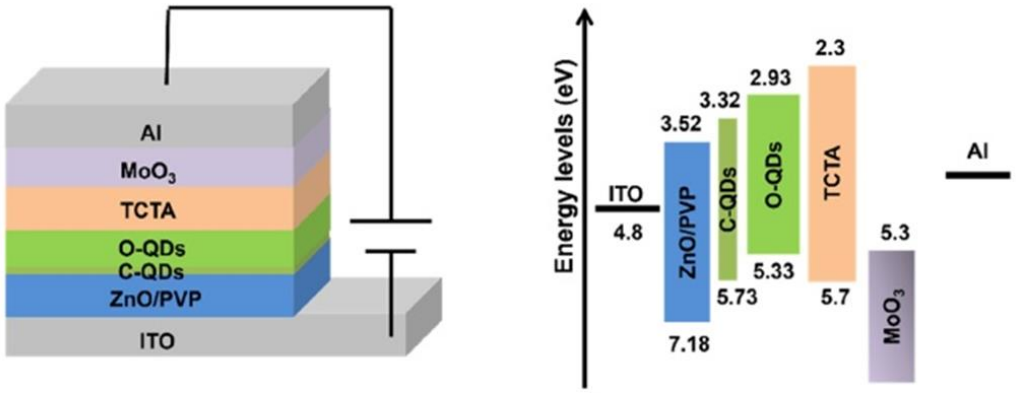

Figure 5.5 | Designed inverted green PeQLED structure and corresponding diagram of energy levels.

ZnO is believed to achieve stable PeQLEDs as ZnO is a stable ETL with high charge mobility and suitable energy levels. However, the performance of green PeQLEDs with ZnO ETL is limited to the interfacial reactions between ZnO nanoparticles and perovskite films. The deprotonation reaction of the ammonium cations at the ZnO/perovskite interface can induce the decomposition of perovskites. An inverted device structure is designed to solve the problem, as shown in Figure 5.5(Shen et al., 2023). Here, C_3-S-HBr passivated OTAc/OTAm $CsPbBr_3$ NCs are notated as "O-QDs", while C_3-S-HBr passivated DEHPA $CsPbBr_3$ NCs are notated as "C-QDs". The difference between the two QDs is explained in Chapter 3. Specifically, O-QDs have good conductivity due to short chain length ligands and low ligands weight ratio. In contrast, C-QDs have high ligand contents and good polar solvent resistance. A polymer interface layer (PVP) is also inserted to relieve the fluorescence quenching and interface reactions. Additionally, a double perovskite layer structure is designed to obtain a balance between the electric and optical properties of emission layers.

Works in Chapter 5 were published: Shen, P., Zhang, X., Wu, R., Zhang, T., Qian, L., Xu, W., Kang, K., Zhao, D., Xiang, C., 2023. ACS Appl. Mater. Interfaces. Wang, Q., Zhang, X., Qian, L., Xiang, C., 2023. ACS Appl. Mater. Interfaces 15, 28833–28839.

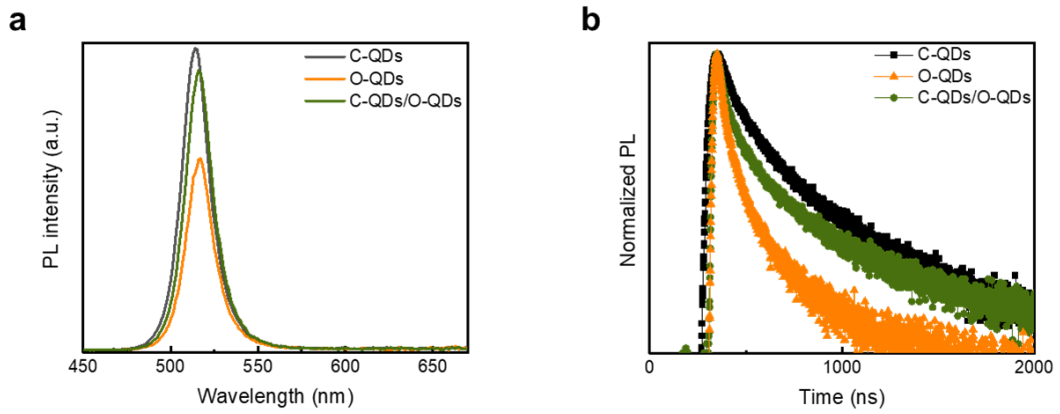

Figure 5.6 | (a) PL intensity and (b) TRPL of different perovskite films on ZnO/PVP substrates.

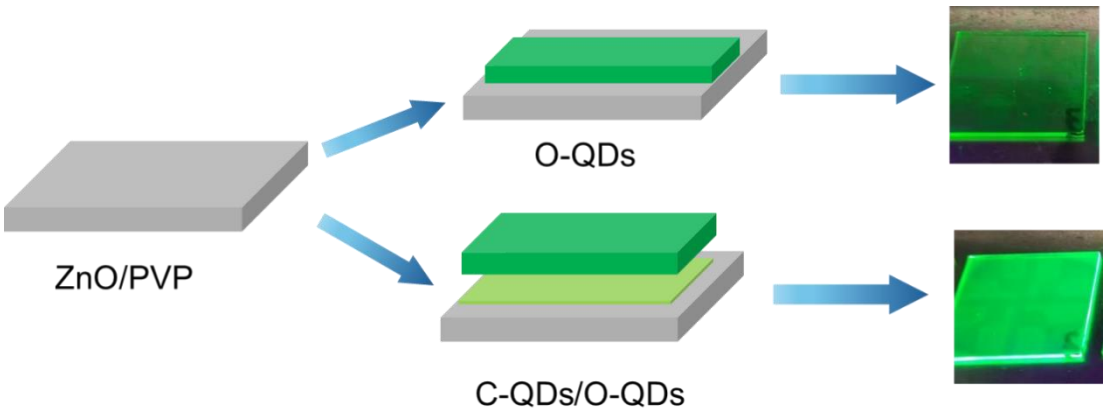

Figure 5.7 | Schematical illustration of the fabrication process of different perovskite films on ZnO/PVP substates.

Figure 5.6a shows different perovskite film PL intensities on ZnO/PVP substrates. C-QDs film exhibits the highest PL intensity on the ZnO/PVP substates. It is observed that the fluorescence of O-QDs is severely quenched. The exciton quench is relieved by inserting a C-QDs layer (5 mg mL^{-1} at 4000 rpm) into the interface between ZnO/PVP substrates and O-QDs. The measured TRPL spectra manifest similar results (Figure 5.6b). C-QDs present the longest average exciton lifetime on ZnO/PVP substrates. O-QDs have the shortest average exciton lifetime due to high interface trap states. The perovskite film average exciton lifetime increases by inserting a C-QDs layer. Figure 5.7 is the

schematical illustration of the double perovskite film fabrication process. The advantages of using C-QDs as buffer layers are good device conductivity and suitable energy levels compared to adding a polymer on ZnO/PVP as a buffer layer.

5.4 Device performance

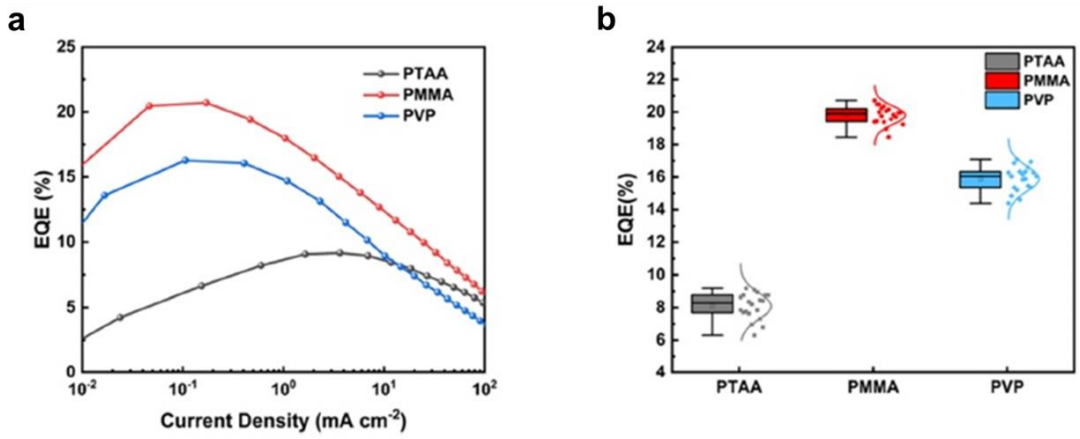

Figure 5.8 | (a) EQE versus current density curves and (b) EQE distribution of PeQLEDs with different buffer layers.

The device performance of C_3-S-HBr passivated OTAc/OTAm NCs is measured to explore the influence of different polymer buffer layers. The device structure used here is the same as in Chapter 3. The structure is ITO/PEDOT: PSS/PTAA/buffer layer or no buffer layer/ LHP NCs/TPBi/PTAA/Al. As shown in Figure 5.8a, the maximum EQE of the devices without buffer layers is only 9.18%. Comparatively, the device performance is significantly improved for PeQLEDs with buffer layers. The peak EQE of the champion device with a PMMA buffer layer is 20.71%. Although the device with PVP buffer layers gains a peak EQE OF 17.09%, it is much higher than 9.18%. Figure 5.8b shows the EQE distributions of all devices. The distribution indicates good repeatability of experiments and methods.

The device performance of the designed inverted structures is also investigated (Figure 5.9)(Shen et al., 2023). The O-QDs devices show relatively large current densities under the same voltage bias. This is because O-QDs have good conductivity. However,

the inverted device structure manifests much lower current densities, EQE, and higher turn-on voltage than common device structures. The peak EQE of the champion device of double perovskite films is 13.1%. This is a record value for inverted Green PeQELDs, as shown in Table 5.1.

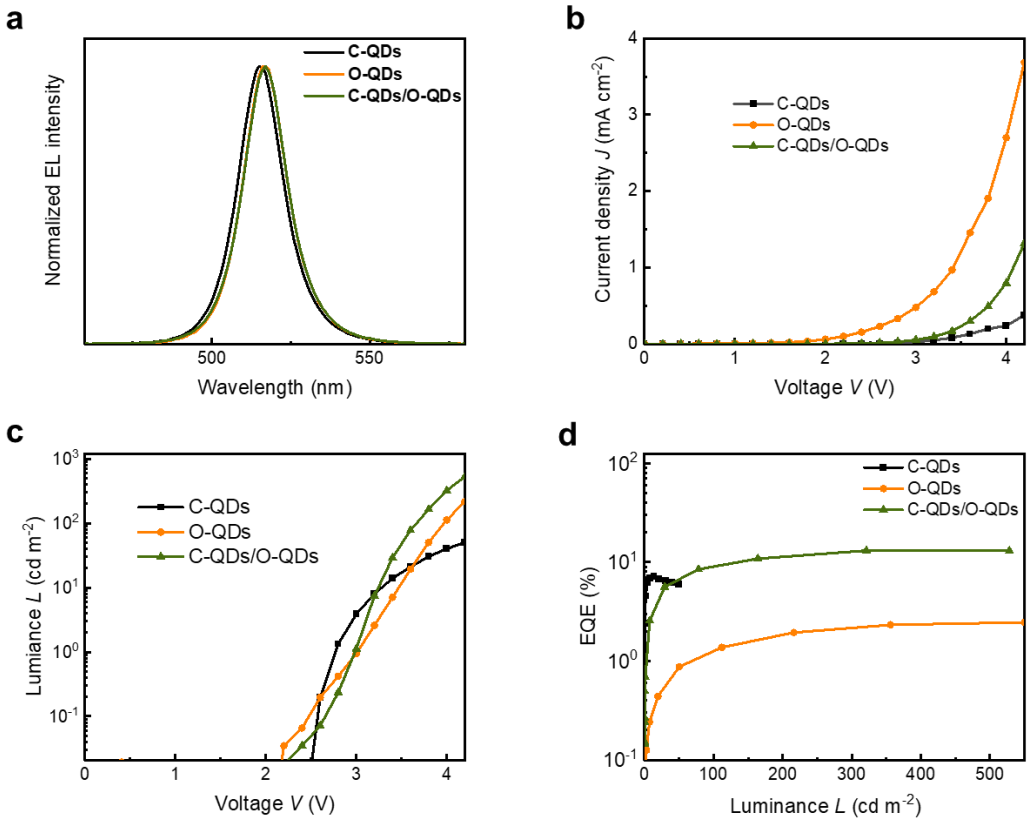

Figure 5.9 | (a) EL spectra, (b) current density versus voltage curves, (c) Luminance versus voltage curves, and (d) EQE versus luminance curves of fabricated inverted PeQLEDs with different perovskite films.

Works in Chapter 5 were published: Shen, P., Zhang, X., Wu, R., Zhang, T., Qian, L., Xu, W., Kang, K., Zhao, D., Xiang, C., 2023. ACS Appl. Mater. Interfaces. Wang, Q., Zhang, X., Qian, L., Xiang, C., 2023. ACS Appl. Mater. Interfaces 15, 28833–28839.

Table 5.1 | Summary of performance of inverted PeQLEDs.

Perovskite	EL (nm)	EQE (%)	T_{50} (s)	Year
ITO/ZnLiO/ZnMgO/$CsPbBr_3$ QDs/TCTA/NPD/HATCN/Liq/Al	519.7	5.71	/	2018(Moyen et al., 2018)
ITO/ZnMgO/$FAPbBr_3$ QDs/TFB/MoOx/Al	535	12.7	290 (2300 $cd \cdot m^{-2}$)	2023(Du et al., 2023)
ITO/ZnMgO/$CsPbBr_3$ QDs/NPB/HATCN/MoO_3/A	517	5.95	/	2020(J. Pan et al., 2020)
ITO/ZnO/PFN-Br/$CsPbBr_3$ QDs/TCTA/ MoO_3/Al	516	/	/	2023(Chiu et al., 2023)
ITO/ZnO/PVP/C-$CsPbBr_3$/ O-$CsPbBr_3$ QDs/TCTA/ MoO_3/Al	517	13.1	/	Our work

5.5 Summary

In this chapter, different device structures are designed to improve the performance of PeQELD. Inserting the interface layer between QDs and charge transport layers can reduce interface traps, fluorescence quenching, and balance charge injection. Thus, this strategy efficiently increases EQE and the operation lifetime. However, the designed inverted device structure does not show advantages over typical structures. This is due to the ionic nature of perovskite QDs and energy level mismatch.

Works in Chapter 5 were published: Shen, P., Zhang, X., Wu, R., Zhang, T., Qian, L., Xu, W., Kang, K., Zhao, D., Xiang, C., 2023. ACS Appl. Mater. Interfaces. Wang, Q., Zhang, X., Qian, L., Xiang, C., 2023. ACS Appl. Mater. Interfaces 15, 28833–28839.

Chapter 6. Conclusion and Recommended Future Work

The thesis starts with a review of QDs and introduces the history of perovskite. The LHP NCs are an intersection of QDs and LHP. Owing to the good electronic and optical properties of LHP NCs, they are promising candidates for next-generation displays. However, LHP NCs are unstable due to their ionic nature. The PeQLEDs' operation lifetime is far from that of Cd-based QLEDs. As the commercial EL application of traditional QDs is around the corner, it is urgent to improve the stability of LHP to satisfy rigorous industrial standards. The weak ligand binding and uncontrollable synthesis of LHP NCs hinders the improvement of materials' stability. Moreover, the PeQELDs suffer from unbalanced charge injection, interface traps, and energy level mismatch. As a result, this thesis aims to explore the synthesis mechanism to control the kinetics of the process with different ligands. Additionally, the fundamental mechanisms of LEDs are investigated to improve the device's performance.

Stable and efficient green LHP NCs are synthesised by in-situ ligand exchange. A novel potent ligands agent is prepared by reacting zwitterionic ligands with HBr. This method improved the traditional HT method synthesis for perovskite nanocrystals as it is difficult for the conventional method to achieve efficient, vigorous ligand exchange. The nanocrystal films achieve excellent environmental stability, high photoluminescence efficiency, and temperature stability. Moreover, the nucleation and growth process is controlled with short-chain length acids/bases and the resurfacing agents. With short chain length acid/base, the cluster intermediates that induce non-uniform nucleation are eliminated. Homogeneous nucleation is achieved. The synthesised nanocrystal distribution is narrowed. Harmful Ostwald ripening is prohibited by the added resurface agent, which can also passivate surface defects. The fabricated green perovskite QLEDs achieved operation stability T_{50} of 54 min at 10000 nits with high efficiency exceeding

24%. The peak emission is 517 nm with an FWHM of 16 nm.

Stable pure-red $CsPbI_3$ QDs are synthesised by regulating the growth of QDs. Defective surface-induced spontaneous growth is hindered by proper strong organic acid passivation. In addition, overgrowth in the purification process is also impeded by strong binding inorganic salt. The pure-red $CsPbI_3$ QDs gained an average size of 4.3 nm with an emission wavelength of 623 nm, whose full width of half maximum is only 32 nm with 94% photoluminescence quantum yield. PeQLEDs, based on them, achieve an EQE of 26.04% at 628 nm, and the T_{50} lifetime is 23053 minutes at 100 $cd \cdot m^{-2}$.

Efficient double ETL structures are designed for PeQELDs and achieve good device performance. Interface traps and fluorescence quenching are reduced. Adding buffer layers balances the charge injection of the device. The operation lifetime of PeQELDs is significantly improved. However, it is unsuccessful in utilising the inorganic ETL ZnO for PeQLEDs.

Although monumental achievements have been made with the endeavours of researchers in perovskite QD synthesis, future works are still needed to meet the requisites of repeatable, efficient, and stable perovskite QD production. The yield of the HT method is 40~60% and causes a massive waste of raw materials. Further improvement and optimisation of the HT method are necessary to decrease production costs. TOPO can be used as a solvent to replace the ODE, achieving 100% yield(Akkerman et al., 2022). It is suggested to use TOPO to improve the synthesis method.

In addition, perovskite QDs are passivated and stabilised by various ligands, but an incomplete understanding of the perovskite surface chemistry makes it challenging to fine-regulate the surface ligand configuration. Researchers can only obtain quantitative information on perovskite QD surfaces, such as the ligand types and overall ligand weight ratio. As for the specific number and distribution of ligands on the perovskite surface, researchers cannot draw reliable conclusions to quantify this information. It is suggested to use molecular dynamics simulation to obtain this information. From the device perspective, perovskite QDs seem incompatible with inorganic metal oxide charge

transport layers using inverted device structures. The essential condition for using the typical structure is to develop perovskite QDs with good polar solvent resistance that can bear metal oxides. Such stable perovskite QDs are supposed to increase the operation lifetime of devices to industrial standards. The stable perovskite QDs are highly dependent on the surface configuration and ligands. Therefore, future work on perovskite surface chemistry should focus on fine control ligand categories, distribution, and binding on surfaces. It is suggested that PeNCs be synthesised with DDDAm and PEA ligands, which can construct a compact hydrophobic layer on the surface.

Besides materials, the complicated device degradation mechanism in PeQELDs needs to be elucidated. There is limited research on this topic. However, there is plenty of research on QLEDs to analyse device failure. Things are not the same for PeQLEDs, but these research methods are inspiring, and researchers in the field of PeQLEDs are benefiting from these publications. It is necessary to establish a device degradation model for researchers in the field of PeQLED. PeNCs lose ligands and degrade because of accumulated charge, while joule heat is produced due to low power conversion efficiency. It is suggested that joule heat and PeNC degradation are the two most important mechanisms for device degradation. The device degradation model shall be established based on those mechanisms.

In conclusion, with proper device structure design, the stability of PeQELD is dramatically enhanced. The improvement in this thesis is mainly attributed to the sound quality of synthesised LHP NCs. Future works should focus on stable materials synthesis and device degradation mechanism investigation to achieve the commercial applications of PeQLEDs,

Reference

Akkerman, Q.A., Nguyen, T.P.T.T., Boehme, S.C., Montanarella, F., Dirin, D.N., Wechsler, P., Beiglböck, F., Rainò, G., Erni, R., Katan, C., Even, J., Kovalenko, M. V., BeiglbÃ¶ck, F., RainÃ², G., Erni, R., Katan, C., Even, J., Kovalenko, M. V., 2022. Science (80-.). 377, 1406–1412.

Akkerman, Q.A., Rainò, G., Kovalenko, M. V., Manna, L., 2018. Nat. Mater. 17, 394–405.

Almeida, G., Goldoni, L., Akkerman, Q., Dang, Z., Khan, A.H., Marras, S., Moreels, I., Manna, L., 2018. ACS Nano 12, 1704–1711.

Aristidou, N., Eames, C., Sanchez-Molina, I., Bu, X., Kosco, J., Saiful Islam, M., Haque, S.A., 2017. Nat. Commun. 8, 1–10.

Bi, C., Yao, Z., Hu, J., Wang, X., Zhang, M., Tian, S., Liu, A., Lu, Y., de Leeuw, N.H., Sui, M., Tian, J., 2023. ACS Energy Lett. 8, 731–739.

Bi, C., Yao, Z., Sun, X., Wei, X., Wang, J., Tian, J., 2021. Adv. Mater. 33.

Blöchl, P.E., 1994. Phys. Rev. B 50, 17953–17979.

Bodnarchuk, M.I., Boehme, S.C., Ten Brinck, S., Bernasconi, C., Shynkarenko, Y., Krieg, F., Widmer, R., Aeschlimann, B., Günther, D., Kovalenko, M. V., Infante, I., 2019. ACS Energy Lett. 4, 63–74.

Brown, A.A.M., Hooper, T.J.N., Veldhuis, S.A., Chin, X.Y., Bruno, A., Vashishtha, P., Tey, J.N., Jiang, L., Damodaran, B., Pu, S.H., Mhaisalkar, S.G., Mathews, N., 2019. Nanoscale 11, 12370–12380.

Brus, L., 1986. J. Phys. Chem. 90, 2555–2560.

Brus, L.E., 1984. J. Chem. Phys. 80, 4403–4409.

Cai, Y., Wang, H., Li, Y., Wang, L., Lv, Y., Yang, X., Xie, R.J., 2019. Chem. Mater. 31, 881–889.

Chen, H., Liu, T., Zhou, P., Li, S., Ren, J., He, H., Wang, J., Wang, N., Guo, S., 2020. Adv. Mater. 32, 1905661.

Chen, H.F., Yang, S.J., Tsai, Z.H., Hung, W.Y., Wang, T.C., Wong, K.T., 2009. J. Mater.

Chem. 19, 8112–8118.

Chen, J., Liu, D., Al-Marri, M.J., Nuuttila, L., Lehtivuori, H., Zheng, K., 2016. Sci. China Mater. 59, 719–727.

Chen, M., Zou, Y., Wu, L., Pan, Q., Yang, D., Hu, H., Tan, Y., Zhong, Q., Xu, Y., Liu, H., Sun, B., Zhang, Q., 2017. Adv. Funct. Mater. 27.

Chen, O., Zhao, J., Chauhan, V.P., Cui, J., Wong, C., Harris, D.K., Wei, H., Han, H.S., Fukumura, D., Jain, R.K., Bawendi, M.G., 2013. Nat. Mater. 12, 445–451.

Chen, Z., Chen, S., 2022. Adv. Opt. Mater. 10, 2102404.

Chiba, T., Hayashi, Y., Ebe, H., Hoshi, K., Sato, J., Sato, S., Pu, Y.-J.J., Ohisa, S., Kido, J., 2018. Nat. Photonics 12, 681–687.

Chiba, T., Hoshi, K., Pu, Y.J., Takeda, Y., Hayashi, Y., Ohisa, S., Kawata, S., Kido, J., 2017. ACS Appl. Mater. Interfaces 9, 18054–18060.

Chiu, F.B., Wu, Y.W., Yang, S.H., 2023. ACS Omega 8, 19109–19118.

Dai, J., Xi, J., Li, L., Zhao, J.F., Shi, Y., Zhang, W., Ran, C., Jiao, B., Hou, X., Duan, X., Wu, Z., 2018. Angew. Chemie - Int. Ed. 57, 5754–5758.

Dai, X., Zhang, Z., Jin, Y., Niu, Y., Cao, H., Liang, X., Chen, L., Wang, J., Peng, X., 2014. Nature 515, 96–99.

Deng, M., Li, Y., Zhang, X., Wu, C., Ding, S., Zhang, T., Zhou, M., Li, R., Xiang, C., 2024a. ACS Photonics.

Deng, M., Li, Y., Zhang, X., Wu, C., Zhang, T., Qian, L., Xiang, C., 2024b. Adv. Opt. Mater. 12, 1–8.

Dong, Y., Qiao, T., Kim, D., Parobek, D., Rossi, D., Son, D.H., 2018. Nano Lett. 18, 3716–3722.

Dong, Y., Wang, Y.K., Yuan, F., Johnston, A., Liu, Y., Ma, D., Choi, M.J., Chen, B., Chekini, M., Baek, S.W., Sagar, L.K., Fan, J., Hou, Y., Wu, M., Lee, S., Sun, B., Hoogland, S., Quintero-Bermudez, R., Ebe, H., Todorovic, P., Dinic, F., Li, P., Kung, H.T., Saidaminov, M.I., Kumacheva, E., Spiecker, E., Liao, L.S., Voznyy, O., Lu, Z.H., Sargent, E.H., 2020. Nat. Nanotechnol. 15, 668–674.

Du, Y., Gao, Y., Si, J., Du, Z., Xu, R., Hu, Q., Hao, X., Gong, X., Zhang, Z., Zhao, H., Cai, P., Ai, Q., Yao, X., Cai, M., Ye, Z., Dai, X., Liu, Z., 2023. ACS Mater. Lett. 5, 1179–1187.

Era, M., Morimoto, S., Tsutsui, T., Saito, S., 1994. Appl. Phys. Lett. 65, 676–678.

Fang, T., Wang, T., Li, X., Dong, Y., Bai, S., Song, J., 2021. Sci. Bull. 66, 36–43.

Gao, Y., Li, B., Liu, X., Shen, H., Song, Y., Song, J., Yan, Z., Yan, X., Chong, Y., Yao, R., Wang, S., Li, L.S., Fan, F., Du, Z., 2023. Nat. Nanotechnol. 18, 1168–1174.

Green, P.B., Narayanan, P., Li, Z., Sohn, P., Imperiale, C.J., Wilson, M.W.B., 2020. Chem. Mater. 32, 4083–4094.

Grisorio, R., Fasulo, F., Muñoz-García, A.B., Pavone, M., Conelli, D., Fanizza, E., Striccoli, M., Allegretta, I., Terzano, R., Margiotta, N., Vivo, P., Suranna, G.P., 2022. Nano Lett. 22, 4437–4444.

Han, T.-H., Jang, K.Y., Dong, Y., Friend, R.H., Sargent, E.H., Lee, T.-W., 2022. Nat. Rev. Mater. 7, 757–777.

Hassan, Y., Park, J.H., Crawford, M.L., Sadhanala, A., Lee, J., Sadighian, J.C., Mosconi, E., Shivanna, R., Radicchi, E., Jeong, M., Yang, C., Choi, H., Park, S.H., Song, M.H., De Angelis, F., Wong, C.Y., Friend, R.H., Lee, B.R., Snaith, H.J., 2021. Nature 591, 72–77.

Huang, H., Bodnarchuk, M.I., Kershaw, S. V., Kovalenko, M. V., Rogach, A.L., 2017. Lead Halide Perovskite Nanocrystals in the Research Spotlight: Stability and Defect Tolerance. ACS Energy Lett.

Huang, H., Zhao, F., Liu, L., Zhang, F., Wu, X., Shi, L., Zou, B., Pei, Q., Zhong, H., 2015. ACS Appl. Mater. Interfaces 7, 28128–28133.

Huang, S., Li, Z., Wang, B., Zhu, N., Zhang, C., Kong, L., Zhang, Q., Shan, A., Li, L., 2017. ACS Appl. Mater. Interfaces 9, 7249–7258.

Imran, M., Caligiuri, V., Wang, M., Goldoni, L., Prato, M., Krahne, R., De Trizio, L., Manna, L., 2018a. J. Am. Chem. Soc. 140, 2656–2664.

Imran, M., Ijaz, P., Baranov, D., Goldoni, L., Petralanda, U., Akkerman, Q., Abdelhady,

A.L., Prato, M., Bianchini, P., Infante, I., Manna, L., 2018b. Nano Lett. 18, 7822–7831.

Imran, M., Ijaz, P., Goldoni, L., Maggioni, D., Petralanda, U., Prato, M., Almeida, G., Infante, I., Manna, L., 2019. ACS Energy Lett. 4, 819–824.

Itaya, K., Uchida, I., Neff, V.D., 1986. Acc. Chem. Res. 19, 162–168.

Jang, Junho, Kim, Young Hoon, Park, S., Yoo, D., Cho, H., Jang, Jinhyeong, Jeong, H.B., Lee, H., Yuk, J.M., Park, C.B., Jeon, D.Y., Kim, Yong Hyun, Bae, B.S., Lee, T.W., 2021. Extremely Stable Luminescent Crosslinked Perovskite Nanoparticles under Harsh Environments over 1.5 Years. Adv. Mater.

Jiang, Y., Sun, C., Xu, J., Li, S., Cui, M., Fu, X., Liu, Yuan, Liu, Yaqi, Wan, H., Wei, K., Zhou, T., Zhang, W., Yang, Y., Yang, J., Qin, C., Gao, S., Pan, J., Liu, Yufang, Hoogland, S., Sargent, E.H., Chen, J., Yuan, M., 2022. Nature 612, 679–684.

Joubert, D., 1999. Phys. Rev. B - Condens. Matter Mater. Phys. 59, 1758–1775.

Kagan, C.R., Mitzi, D.B., Dimitrakopoulos, C.D., 1999. Science (80-.). 286, 945–947.

Kim, Y.H.W., Kim, S., Kakekhani, A., Park, J.J., Park, J.J., Lee, Y.H., Xu, H., Nagane, S., Wexler, R.B., Kim, D.H., Jo, S.H., Martínez-Sarti, L., Tan, P., Sadhanala, A., Park, G.S., Kim, Y.H.W., Hu, B., Bolink, H.J., Yoo, S., Friend, R.H., Rappe, A.M., Lee, T.W., 2021. Comprehensive defect suppression in perovskite nanocrystals for high-efficiency light-emitting diodes, Nature Photonics. Nature Research.

Kojima, A., Teshima, K., Shirai, Y., Miyasaka, T., 2009. J. Am. Chem. Soc. 131, 6050–6051.

Kovalenko, M. V., Protesescu, L., Bodnarchuk, M.I., 2017. Science (80-.). 358, 745–750.

Kresse, G., Furthmüller, J., 1996. Comput. Mater. Sci. 6, 15–50.

Kresse, G., Hafner, J., 1993. Phys. Rev. B 47, 558–561.

Krieg, F., Ochsenbein, S.T., Yakunin, S., Ten Brinck, S., Aellen, P., Süess, A., Clerc, B., Guggisberg, D., Nazarenko, O., Shynkarenko, Y., Kumar, S., Shih, C.J., Infante, I., Kovalenko, M. V., 2018. ACS Energy Lett. 3, 641–646.

Krieg, F., Ong, Q.K., Burian, M., Rainò, G., Naumenko, D., Amenitsch, H., Süess, A.,

Grotevent, M.J., Krumeich, F., Bodnarchuk, M.I., Shorubalko, I., Stellacci, F., Kovalenko, M. V., 2019. J. Am. Chem. Soc. 141, 19839–19849.

Kumar, S., Marcato, T., Krumeich, F., Li, Y.-T., Chiu, Y.-C., Shih, C.-J., 2022. Nat. Commun. 13, 2106.

Kwak, J., Bae, W.K., Lee, D., Park, I., Lim, J., Park, M., Cho, H., Woo, H., Yoon, D.Y., Char, K., Lee, S., Lee, C., 2012. Nano Lett. 12, 2362–2366.

v. L. Colvin, M. C. Schlamp, A. P. Allvlsatos, 1994. Nature 370, 354–357.

Lan, Y.-F., Yao, J.-S., Yang, J.-N., Song, Y.-H., Ru, X.-C., Zhang, Q., Feng, L.-Z., Chen, T., Song, K.-H., Yao, H.-B., 2021. Nano Lett. 21, 8756–8763.

Leguy, A.M.A., Hu, Y., Campoy-Quiles, M., Alonso, M.I., Weber, O.J., Azarhoosh, P., Van Schilfgaarde, M., Weller, M.T., Bein, T., Nelson, J., Docampo, P., Barnes, P.R.F., 2015. Chem. Mater. 27, 3397–3407.

Li, G., Huang, J., Zhu, H., Li, Y., Tang, J.X., Jiang, Y., 2018. Chem. Mater. 30, 6099–6107.

Li, H., Feng, Y., Zhu, M., Gao, Y., Fan, C., Cui, Q., Cai, Q., Yang, K., He, H., Dai, X., Huang, J., Ye, Z., 2024. Nat. Nanotechnol. 19, 638–645.

Li, J., Xu, L., Wang, T., Song, J., Chen, J., Xue, J., Dong, Y., Cai, B., Shan, Q., Han, B., Zeng, H., 2017. Adv. Mater. 29.

Li, J.J., Wang, Y.A., Guo, W., Keay, J.C., Mishima, T.D., Johnson, M.B., Peng, X., 2003. J. Am. Chem. Soc. 125, 12567–12575.

Li, X., Wu, Y., Zhang, S., Cai, B., Gu, Y., Song, J., Zeng, H., 2016. Adv. Funct. Mater. 26, 2435–2445.

Li, Y., Deng, M., Zhang, X., Qian, L., Xiang, C., 2024a. Nano-Micro Lett. 16, 1–10.

Li, Y., Deng, M., Zhang, X., Xu, T., Wang, X., Yao, Z., Wang, Q., Qian, L., Xiang, C., 2024b. Nat. Commun. 15, 5696.

Li, Y., Huang, H., Xiong, Y., Kershaw, S. V., Rogach, A.L., 2018. Angew. Chemie - Int. Ed. 57, 5833–5837.

Lignos, I., Morad, V., Shynkarenko, Y., Bernasconi, C., Maceiczyk, R.M., Protesescu, L.,

Bertolotti, F., Kumar, S., Ochsenbein, S.T., Masciocchi, N., Guagliardi, A., Shih, C.J., Bodnarchuk, M.I., Demello, A.J., Kovalenko, M. V., 2018. ACS Nano 12, 5504–5517.

Lignos, I., Stavrakis, S., Nedelcu, G., Protesescu, L., Demello, A.J., Kovalenko, M. V., 2016. Nano Lett. 16, 1869–1877.

Lim, J., Park, Y.S., Wu, K., Yun, H.J., Klimov, V.I., 2018. Nano Lett. 18, 6645–6653.

Lin, Y., Adilbekova, B., Firdaus, Y., Yengel, E., Faber, H., Sajjad, M., Zheng, X., Yarali, E., Seitkhan, A., Bakr, O.M., El-Labban, A., Schwingenschlögl, U., Tung, V., McCulloch, I., Laquai, F., Anthopoulos, T.D., 2019. Adv. Mater. 31.

Liu, A., Bi, C., Tian, J., 2022. Adv. Funct. Mater. 32, 2207069.

Liu, F., Zhang, Y., Ding, C., Kobayashi, S., Izuishi, T., Nakazawa, N., Toyoda, T., Ohta, T., Hayase, S., Minemoto, T., Yoshino, K., Dai, S., Shen, Q., 2017. ACS Nano 11, 10373–10383.

Liu, M., Wan, Q., Wang, H., Carulli, F., Sun, X., Zheng, W., Kong, L., Zhang, Qi, Zhang, C., Zhang, Qinggang, Brovelli, S., Li, L., 2021. Nat. Photonics 15, 379–385.

Liu, X.K., Xu, W., Bai, S., Jin, Y., Wang, J., Friend, R.H., Gao, F., 2021. Nat. Mater. 20, 10–21.

Liu, Y., Jiang, C., Song, C., Wang, Juanhong, Mu, L., He, Z., Zhong, Z., Cun, Y., Mai, C., Wang, Jian, Peng, J., Cao, Y., 2018. ACS Nano 12, 1564–1570.

Luo, Z., Xu, D., Wu, S., 2014. J. Disp. Technol. 10, 526–539.

Mashford, B.S., Stevenson, M., Popovic, Z., Hamilton, C., Zhou, Z., Breen, C., Steckel, J., Bulovic, V., Bawendi, M., Coe-Sullivan, S., Kazlas, P.T., 2013. Nat. Photonics 7, 407–412.

Morad, V., Stelmakh, A., Svyrydenko, M., Feld, L.G., Boehme, S.C., Aebli, M., Affolter, J., Kaul, C.J., Schrenker, N.J., Bals, S., Sahin, Y., Dirin, D.N., Cherniukh, I., Raino, G., Baumketner, A., Kovalenko, M. V., 2024. Nature 626, 542–548.

Moyen, E., Jun, H., Kim, H.M., Jang, J., 2018. ACS Appl. Mater. Interfaces 10, 42647–42656.

Nanocrystallites, T.S., Murray, C.B., Noms, D.J., Bawendi, M.G., 1993a. J. Am. Chem. Soc. 115, 8706–8715.

Nanocrystallites, T.S., Murray, C.B., Noms, D.J., Bawendi, M.G., 1993b. J Am Chem Soc 115, 8706–8715.

Nenon, D.P., Pressler, K., Kang, J., Koscher, B.A., Olshansky, J.H., Osowiecki, W.T., Koc, M.A., Wang, L.-W., Alivisatos, A.P., 2018. J. Am. Chem. Soc. 140, 17760–17772.

Nguyen, H.T., Duong, A.T., Lee, S., 2021. J. Mater. Res. 36, 3309–3316.

Pack, J.D., Monkhorst, H.J., 1977. Phys. Rev. B 16, 1748–1749.

Pan, G., Bai, X., Xu, W., Chen, X., Zhai, Y., Zhu, J., Shao, H., Ding, N., Xu, L., Dong, B., Mao, Y., Song, H., 2020. ACS Appl. Mater. Interfaces 12, 14195–14202.

Pan, J., Fang, F., Xie, J., Wang, L., Chen, J., Chang, J., Lei, W., Zhang, W., Zhao, D., 2020. J. Mater. Chem. C 8, 5572–5579.

Pan, J., Quan, L.N., Zhao, Y., Peng, W., Murali, B., Sarmah, S.P., Yuan, M., Sinatra, L., Alyami, N.M., Liu, J., Yassitepe, E., Yang, Z., Voznyy, O., Comin, R., Hedhili, M.N., Mohammed, O.F., Lu, Z.H., Kim, D.H., Sargent, E.H., Bakr, O.M., 2016. Adv. Mater. 28, 8718–8725.

Pan, Q., Hu, H., Zou, Y., Chen, M., Wu, L., Yang, D., Yuan, X., Fan, J., Sun, B., Zhang, Q., 2017. J. Mater. Chem. C 5, 10947–10954.

Protesescu, L., Yakunin, S., Bodnarchuk, M.I., Krieg, F., Caputo, R., Hendon, C.H., Yang, R.X., Walsh, A., Kovalenko, M. V., 2015. Nano Lett. 15, 3692–3696.

Qian, L., Zheng, Y., Choudhury, K.R., Bera, D., So, F., Xue, J., Holloway, P.H., 2010. Nano Today 5, 384–389.

Qian, L., Zheng, Y., Xue, J., Holloway, P.H., 2011. Nat. Photonics 5, 543–548.

Quarta, D., Imran, M., Capodilupo, A.L., Petralanda, U., Van Beek, B., De Angelis, F., Manna, L., Infante, I., De Trizio, L., Giansante, C., 2019. J. Phys. Chem. Lett. 10, 3715–3726.

Rainò, G., Yazdani, N., Boehme, S.C., Kober-Czerny, M., Zhu, C., Krieg, F., Rossell,

M.D., Erni, R., Wood, V., Infante, I., Kovalenko, M. V., 2022. Nat. Commun. 13, 1–8.

Ren, X., Zhang, X., Xie, H., Cai, J., Wang, C., Chen, E., Xu, S., Ye, Y., Sun, J., Yan, Q., Guo, T., 2022. Nanomaterials 12, 1–27.

De Roo, J., Ibáñez, M., Geiregat, P., Nedelcu, G., Walravens, W., Maes, J., Martins, J.C., Van Driessche, I., Kovalenko, M. V., Hens, Z., 2016. ACS Nano 10, 2071–2081.

Search, H., Journals, C., Contact, A., Iopscience, M., Address, I.P., 2015. 71.

Seth, S., Samanta, A., 2016. Sci. Rep. 6, 1–7.

Shamsi, J., Urban, A.S., Imran, M., De Trizio, L., Manna, L., 2019. Chem. Rev. 119, 3296–3348.

Shen, P., Zhang, X., Wu, R., Zhang, T., Qian, L., Xu, W., Kang, K., Zhao, D., Xiang, C., 2023. ACS Appl. Mater. Interfaces.

Shi, Z., Li, S., Li, Y., Ji, H., Li, X., Wu, D., Xu, T., Chen, Y., Tian, Y., Zhang, Y., Shan, C., Du, G., 2018. ACS Nano 12, 1462–1472.

Shirasaki, Y., Supran, G.J., Bawendi, M.G., Bulović, V., 2013. Nat. Photonics 7, 933–933.

Song, J., Fang, T., Li, J., Xu, L., Zhang, F., Han, B., Shan, Q., Zeng, H., 2018a. Adv. Mater. 30, 1805409.

Song, J., Li, J., Li, X., Xu, L., Dong, Y., Zeng, H., 2015. Adv. Mater. 27, 7162–7167.

Song, J., Li, J.J., Xu, L., Li, J.J., Zhang, F., Han, B., Shan, Q., Zeng, H., 2018b. Adv. Mater. 30, 1800764.

Sun, J.K., Huang, S., Liu, X.Z., Xu, Q., Zhang, Q.H., Jiang, W.J., Xue, D.J., Xu, J.C., Ma, J.Y., Ding, J., Ge, Q.Q., Gu, L., Fang, X.H., Zhong, H.Z., Hu, J.S., Wan, L.J., 2018. J. Am. Chem. Soc. 140, 11705–11715.

Sun, S., Lu, M., Guo, J., Yu, W.W., Shi, Z., Sun, G., Zhang, Y., 2020. J. Phys. Chem. C 124, 28277–28284.

Sun, S., Yuan, D., Xu, Y., Wang, A., Deng, Z., 2016. ACS Nano 10, 3648–3657.

Sun, Y., Ge, L., Dai, L., Cho, C., Ferrer Orri, J., Ji, K., Zelewski, S.J., Liu, Y., Mirabelli,

A.J., Zhang, Y., Huang, J.Y., Wang, Y., Gong, K., Lai, M.C., Zhang, L., Yang, D., Lin, J., Tennyson, E.M., Ducati, C., Stranks, S.D., Cui, L.S., Greenham, N.C., 2023. Nature 615.

Swarnkar, A., Marshall, A.R., Sanehira, E.M., Chernomordik, B.D., Moore, D.T., Christians, J.A., Chakrabarti, T., Luther, J.M., 2016. Science (80-.). 354, 92–95.

Tan, Y., Zou, Y., Wu, L., Huang, Q., Yang, D., Chen, M., Ban, M., Wu, C., Wu, T., Bai, S., Song, T., Zhang, Q., Sun, B., 2018. ACS Appl. Mater. Interfaces 10, 3784–3792.

Tang, P., Xie, L., Xiong, X., Wei, C., Zhao, W., Chen, M., Zhuang, J., Su, W., Cui, Z., 2020. ACS Appl. Mater. Interfaces 12, 13087–13095.

Tian, Y., Qin, Z.Y.Y., Zou, S.J.J., Li, Y.Q.Q., Wang, Y., Wang, W., Zhang, C., Tang, J.X.X., 2021. Mater. Today Energy 20, 100649.

Tong, Y., Bladt, E., Aygüler, M.F., Manzi, A., Milowska, K.Z., Hintermayr, V.A., Docampo, P., Bals, S., Urban, A.S., Polavarapu, L., Feldmann, J., 2016. Angew. Chemie - Int. Ed. 55, 13887–13892.

TPBI Xi'an Yuri Solar Co., Ltd [WWW Document], 2025. . https://www.p-oled.cn/zh-hans/products/detail/525/.

Tsai, H., Shrestha, S., Vilá, R.A., Huang, W., Liu, C., Hou, C.-H., Huang, H.-H., Wen, X., Li, M., Wiederrecht, G., Cui, Y., Cotlet, M., Zhang, X., Ma, X., Nie, W., 2021. Nat. Photonics 15, 843–849.

Tu, S., Chen, M., Wu, L., 2021. J. Mater. Chem. C 9, 17444–17450.

Vashishtha, P., Halpert, J.E., 2017. Chem. Mater. 29, 5965–5973.

Vickers, E.T., Graham, T.A., Chowdhury, A.H., Bahrami, B., Dreskin, B.W., Lindley, S., Naghadeh, S.B., Qiao, Q., Zhang, J.Z., 2018. ACS Energy Lett. 3, 2931–2939.

Wan, Q., Zheng, W., Zou, C., Carulli, F., Zhang, C., Song, H., Liu, M., Zhang, Q., Lin, L.Y., Kong, L., Li, L., Brovelli, S., 2023. ACS Energy Lett. 8, 927–934.

Wang, C., Chesman, A.S.R., Jasieniak, J.J., 2017. Chem. Commun. 53, 232–235.

Wang, F., Wang, Z., Zhu, X., Bai, Y., Yang, Y., Hu, S., Liu, Y., You, B., Wang, J., Li, Y., Tan, Z., 2021. Small 17, 1–11.

Wang, H., Dou, Y., Shen, P., Kong, L., Yuan, H., Luo, Y., Zhang, X., Yang, X., 2020a. Small 16.

Wang, H., Dou, Y., Shen, P., Kong, L., Yuan, H., Luo, Y., Zhang, X., Yang, X., 2020b. Small 16, 2001062.

Wang, Q., Zhang, X., Qian, L., Xiang, C., 2023. ACS Appl. Mater. Interfaces 15, 28833–28839.

Wang, Ya-Kun, Yuan, F., Dong, Y., Li, J., Johnston, A., Chen, B., Saidaminov, M.I., Zhou, C., Zheng, X., Hou, Y., Bertens, K., Ebe, H., Ma, D., Deng, Z., Yuan, S., Chen, R., Sagar, L.K., Liu, J., Fan, J., Li, P., Li, X., Gao, Y., Fung, M., Lu, Z., Bakr, O.M., Liao, L., Sargent, E.H., 2021. Angew. Chemie Int. Ed. 60, 16164–16170.

Wang, Yanping, Li, B., Jiang, C., Fang, Y., Bai, P., Wang, Yiqing, 2021. J. Phys. Chem. C 125, 16753–16758.

Wei, Y., Li, Xuefei, Chen, Y., Cheng, Z., Xiao, H., Li, Xinke, Ding, J., Lin, J., 2020. J. Phys. Chem. Lett. 11, 1154–1161.

Wells, H.L., 1893. Zeitschrift für Anorg. Chemie 3, 195–210.

Wu, Y., Li, X., Zeng, H., 2019. ACS Energy Lett. 4, 673–681.

Xiang, C., Wu, L., Lu, Z., Li, M., Wen, Y., Yang, Y., Liu, W., Zhang, T., Cao, W., Tsang, S.W., Shan, B., Yan, X., Qian, L., 2020. Nat. Commun. 11, 1–9.

Xie, L., Yang, J., Zhao, W., Yi, Y., Liu, Y., Su, W., Li, Q., Lei, W., Cui, Z., 2022. Adv. Opt. Mater. 10, 2200935.

Xie, M., Guo, J., Zhang, X., Bi, C., Zhang, L., Chu, Z., Zheng, W., You, J., Tian, J., 2022. Nano Lett. 22, 8266–8273.

Xu, L., Liang, H.W., Yang, Y., Yu, S.H., 2018. Chem. Rev. 118, 3209–3250.

Yan, C., Luo, C., Li, W., Peng, X., Cao, J., Zeng, X., Gao, Y., Fu, X., Chu, X., Deng, W., Chun, F., Yang, S., Wang, Q., Yang, W., 2021. ACS Appl. Mater. Interfaces 13, 57560–57566.

Yang, D., Zhao, B., Yang, T., Lai, R., Lan, D., Friend, R.H., Di, D., 2022. Adv. Funct. Mater. 32, 2109495.

Yang, Y., Zheng, Y., Cao, W., Titov, A., Hyvonen, J., Manders, J.R., Xue, J., Holloway, P.H., Qian, L., 2015. Nat. Photonics 9, 259–265.

Ye, Z., Chen, M., Chen, X., Ma, W., Sun, X., Wu, L., Lin, X., Chen, Y., Chen, S., 2022. npj Flex. Electron. 6, 1–7.

Yoo, J.J., Seo, G., Chua, M.R., Park, T.G., Lu, Y., Rotermund, F., Kim, Y.-K., Moon, C.S., Jeon, N.J., Correa-Baena, J.-P., Bulović, V., Shin, S.S., Bawendi, M.G., Seo, J., 2021. Nature 590, 587–593.

Yuan, F., Zheng, X., Johnston, A., Wang, Y., Zhou, C., Dong, Y., Chen, B., Chen, H., Fan, J.Z., Sharma, G., Li, P., Gao, Y., Voznyy, O., Kung, H., Lu, Z., Bakr, O.M., Sargent, E.H., 2020. Sci. Adv. 6, 1–9.

Yun, S., Kirakosyan, A., Yoon, S.G., Choi, J., 2018. ACS Sustain. Chem. Eng. 6, 3733–3738.

Zhang, C., Wang, B., Li, W., Huang, S., Kong, L., Li, Z., Li, L., 2017. Nat. Commun. 8.

Zhang, H., Fu, X., Tang, Y., Wang, H., Zhang, C., Yu, W.W., Wang, X., Zhang, Y., Xiao, M., 2019. Nat. Commun. 10, 1–8.

Zhang, J., Wang, J., Cai, L., Wang, S., Wu, K., Sun, B., Zheng, W., Kershaw, S. V., Jia, G., Zhang, X., Rogach, A.L., Yang, X., 2024. Angew. Chemie - Int. Ed. 63.

Zhang, J., Zhang, T., Ma, Z., Yuan, F., Zhou, X., Wang, H., Liu, Z., Qing, J., Chen, H., Li, X., Su, S., Xie, J., Shi, Z., Hou, L., Shan, C., 2023. Adv. Mater. 35, 2209002.

Zhang, M., Bi, C., Xia, Y., Sun, X., Wang, X., Liu, A., Tian, S., Liu, X., de Leeuw, N.H., Tian, J., 2023. Angew. Chemie Int. Ed. 62.

Zhang, X., Cheng, H., Zhang, H., 2017. Recent Progress in the Preparation, Assembly, Transformation, and Applications of Layer-Structured Nanodisks beyond Graphene. Adv. Mater.

Zhang, X., Li, D., Zhang, Z., Liu, H., Wang, S., 2022. Adv. Sci. 9, 2200450.

Zhang, X., Wang, Q., Yao, Z., Deng, M., Wang, J., Qian, L., Ren, Y., Yan, Y., Xiang, C., 2023. Adv. Sci. 10, 1–7.

Zhang, Y., Siegler, T.D., Thomas, C.J., Abney, M.K., Shah, T., De Gorostiza, A., Greene,

R.M., Korgel, B.A., 2020. Chem. Mater. 32, 5410–5423.

Zhao, H., Chen, H., Bai, S., Kuang, C., Luo, X., Teng, P., Yin, C., Zeng, P., Hou, L., Yang, Y., Duan, L., Gao, F., Liu, M., 2021. ACS Energy Lett. 6, 2395–2403.

Zhao, H., Hu, Z., Wei, L., Zeng, P., Kuang, C., Liu, X., Bai, S., Gao, F., Liu, M., 2020. Small 16, 2003939.

Zhao, Y.S., Fu, H., Peng, A., Ma, Y., Xiao, D., Yao, J., 2008. Adv. Mater. 20, 2859–2876.

Zheng, X., Yuan, S., Liu, J., Yin, J., Yuan, F., Shen, W.S., Yao, K., Wei, M., Zhou, C., Song, K., Zhang, B. Bin, Lin, Y., Hedhili, M.N., Wehbe, N., Han, Y., Sun, H.T., Lu, Z.H., Anthopoulos, T.D., Mohammed, O.F., Sargent, E.H., Liao, L.S., Bakr, O.M., 2020. ACS Energy Lett. 5, 793–798.

Appendix 1.

Supplementary Information Table A1-1 State-of-the-art perovskite QLEDs performance

QDs Structure	Emission	Maximum EQE	Maximum Luminescence	Operation Lifetime	Reference
$CsPbBr_3$	505	22.00%	10000 $cd \cdot m^{-2}$	T_{50}_1200 nits 60 mins	Nat. Nanotechnol. 15, 668–674 (2020).
$CsPbBr_3$	515	19.30%	2000 $cd \cdot m^{-2}$	T_{50}_1000 nits 50s	Nat. Photonics 15, 379–385 (2021)
$CsPbBr_3$	520/18	21.63%	41900 $cd \cdot m^{-2}$	T_{50}_4000 nits 69 mins	Science Bulletin 66 (2021) 36-43
$FAGAPbBr_3$	531	23.40%	25000 $cd \cdot m^{-2}$	T_{50}_100 nits 132 mins	Nat. Photonics 15, 148–155 (2021)

$CsPbBr_3$	515	21.60%	36000 $cd \cdot m^{-2}$	T_{50}_1000 nits 25.3 mins	Nature 612, 679–684 (2022).
$CsPbBr_3$	518/16.4	17.85%	10000 $cd \cdot m^{-2}$	T_{50}_100 nits 177 mins	Journal of the American Chemical Society 2021 143 (47), 19928-19937
$FAPbBr_3$	532/21	19.20%	67115 $cd \cdot m^{-2}$	T_{50}_100 nits 20 mins	ACS Energy Lett. 2021, 6, 2395−2403
$CsPb(Br/I)_3$	653	21.30%	500 $cd \cdot m^{-2}$	T_{50}_100 nits 5 mins	Nat. Photonics 12, 681-687 (2018)
$MAPb(Br/I)_3$	620	21.30%	627 $cd \cdot m^{-2}$	T_{50}_100 nits 342 mins	Nature 591, 72-77 (2021)
$CsPbI_3$	640	23.00%	1000 $cd \cdot m^{-2}$	T_{50}_200 nits 600 mins	Angew. Chem. Int. Ed. 60, 16164-16170 (2021)
$CsPbI_3$	636	20.80%	3775 $cd \cdot m^{-2}$	T_{50}_110 nits 7.4 mins	Nano Lett. 22, 8266-8273, (2022)
$CsPbI_3$	686	25.30%	13600 $cd \cdot m^{-2}$	T_{50}_1200 nits 840 mins	ACS Nano 2023 17 (10), 9290-9301
$CsPbBr_3$	480/25	12.80%	~500 $cd \cdot m^{-2}$	T_{50}_90 nits 20 mins	Nat. Nanotechnol. 15, 668–674 (2020).
$CsPbBr_3$	480/20	17.80%	~3000 $cd \cdot m^{-2}$	T_{50}_100 nits 120 mins	Nature 612, 679–684 (2022).

Supplementary Information Table A1-2 Summary of red perovskite QLEDs performance.

Perovskite	**EL (nm)**	**Max. EQE (%)**	**L_{max} ($cd \cdot m^{-2}$)**	**T_{50} (min)**	**Reference**

$CsPb(Br/I)_3$ QDs	625	12.9	3382	-	Small 16, 2001062 (2020)
$CsPb(Br/I)_3$ QDs	645	14.1	794	180 (100 $cd \cdot m^{-2}$)	Nat. Photonics 12, 681-687 (2018)
$MAPb(Br/I)_3$ QDs	620	20.3	627	342 (100 $cd \cdot m^{-2}$)	Nature 591, 72-77 (2021)
$CsPbI_3$ QDs	636	20.8	3775	7.4 (110 $cd \cdot m^{-2}$)	Nano Lett. 22, 8266-8273, (2022)
$CsPb(Br/I)_3$ QDs	637	21.8	6491	15 (120 $cd \cdot m^{-2}$)	Adv. Funct. Mater. 2300116 (2023)
$CsPbI_3$ QDs	640	23.0	~1000	600 (200 $cd \cdot m^{-2}$)	Angew. Chem. Int. Ed. 60, 16164-16170 (2021)
$CsPbI_3$ QDs	628	26.04	4203	729 (1000 $cd \cdot m^{-2}$)	This work

Appendix 2.

Other Contributed Publications.

- M. Deng, Y. Li, X. Zhang, C. Wu, S. Ding, T. Zhang, M. Zhou, R. Li, C. Xiang, Mitigating Perovskite Light-Emitting Diode Degradation Mechanisms through Forward Electrical Pulses, ACS Photonics (2024). https://doi.org/10.1021/acsphotonics.4c00220.
- M. Deng, Y. Li, X. Zhang, C. Wu, T. Zhang, L. Qian, C. Xiang, High-Efficiency Pure Red CsPbI3 QLEDs Via Strong Electron Affinity Interface Layer Engineering, Adv. Opt. Mater. 12 (2024) 1–8. https://doi.org/10.1002/adom.202302758.
- B. Zhang, S. Ding, X. Zhang, L. Qian, C. Xiang, Enhancing the performance of Quasi-2D perovskite blue light emitting diodes via a WS2 energy matching layer, Chem.

Phys. Lett. 826 (2023) 140671. https://doi.org/10.1016/j.cplett.2023.140671.

- Z. Tang, S. Ding, X. Zhang, C. Wu, N.E. Stott, C. Xiang, L. Qian, Quantum Dots for Display Applications, in: Phosphor Handb., CRC Press, Boca Raton, 2021: pp. 191–214. https://doi.org/10.1201/9781003098676-6.
- S. Ding, W. Gu, X. Zhang, C. Xiang, L. Qian, 23.2: Invited Paper: Progresses in High-Efficiency Air-Stable Solution-processed Perovskite Light Emitting Diodes for Display, SID Symp. Dig. Tech. Pap. 52 (2021) 302–302. https://doi.org/10.1002/sdtp.15101.